MASTER'S THESIS

Earthquake detection and localisation using the NARS-Botswana data

BY

TIZIANA MICALLEF

UNDER THE SUPERVISION OF

DR. HANNEKE PAULSSEN

UTRECHT UNIVERSITY

DEPARTMENT OF EARTH SCIENCES

August 2019

Dedicated to my parents, Michael and Carmen

and my fiancé, Coen.

Abstract

Botswana forms a major gap in our understanding of southern Africa's seismicity. Most of the seismicity data of Botswana has, to date, either been poorly located or gone unreported owing to the paucity of instrumental coverage. Botswana is generally classified as having a low-to-moderate level of seismicity. Over the years, the only seismically active area was considered to be the Okavango Delta Region (ODR) in northern Botswana, leading to the speculation of an incipient continental rift that could represent the terminus of the southwestern branch of the East African Rift System (EARS). Since November 2013, the seismology group at Utrecht University deployed a temporary seismic network, namely the NARS-Botswana network, consisting of 21 seismic stations distributed throughout Botswana's diverse geological and tectonic units. On April 3rd, 2017 a moment magnitude 6.5 normal-faulting earthquake struck Moiyabana in central Botswana unexpectedly, in an area devoid from any recent tectonic activity. This earthquake questioned further our knowledge of the seismicity in Botswana. Thus, in this study, a more reliable assessment of the seismic activity in Botswana has been carried out using data recorded by the NARS-Botswana network from January 1st, 2014 to March 1st, 2018. For the detection and location of seismic events, the NARS-Botswana data is processed and analysed using the seismological software package SeisComP3. The resultant location, origin time and magnitude of each detected event in Botswana have been presented in an earthquake catalogue aiming to contribute positively towards hazard mitigation. During the studied period, a total of 376 seismic events have been detected and located in Botswana, with those above magnitude 4.0 mainly located in the ODR and in central Botswana. The April 3rd, 2017 mainshock, located near the tectonic boundary between the Kaapvaal Craton and Limpopo Belt, appears to be preceded by two low magnitude potential foreshocks. Aftershocks are clustered along a NW-SE strike, consistent with the focal mechanism of the main event and the strike of the Kaapvaal Craton's northern boundary. Within the ODR, most of the seismic events are aligned along a NNW-SSE trending seismicity zone, with the northern tip located at the suggested terminus of the southwestern branch of the EARS. From the clustering of seismic events in Botswana and adjacent countries, results suggest that the seismicity observed along the 2017 Moiyabana earthquake might be related to the seismicity in the ODR and eastern South Africa. Thus, concluding that the southwestern branch of the EARS might be extending southwards from northern to south-eastern Botswana, in a NW-SE direction.

Keywords: Botswana, seismicity, NARS-Botswana, 2017 Moiyabana earthquake, Okavango Delta Region, SeisComP3, continental rifting, East African Rift System.

Layman's Summary

Botswana is one of southern Africa's least studied seismicity areas. Although it is considered as a country with relatively low seismicity, over the years, moderate to large seismic events have been mainly observed in the Okavango Delta region (ODR), the northern part of Botswana. Unfortunately, not much is known and accurately documented about the seismic activity of a larger coverage of Botswana, mainly due to the lack of instrumental coverage throughout the country. Since November 2013, the seismology group at Utrecht University deployed a temporary seismic network, namely the NARS-Botswana network, consisting of 21 seismic stations distributed all over Botswana. Using data recorded by the NARS-Botswana seismic network from January 1st, 2014 to March 1st, 2018, a more reliable assessment of the seismic activity in Botswana has been carried out. The motivation behind this study arose from the unexpected and strong earthquake that occurred on April 3rd, 2017 in central Botswana, in an area acknowledged as tectonically stable. The four years NARS-Botswana data was investigated with a standard seismological software package which detects and locates seismic events. A total of 376 seismic events located within Botswana have been documented in an earthquake catalogue which aims to contribute positively towards hazard mitigation. Each entry in this catalogue describes a seismic event in terms of the date and time of occurrence, location, depth, magnitude and number of used stations in the location computation process. From the resultant earthquake locations, Botswana can be generally regarded as a country with low seismic activity. Moderate to strong earthquakes have been mainly located in northern and central Botswana. During the period under study, the largest event recorded in Botswana was the April 3rd, 2017 earthquake. This main event appears to be preceded by two earthquakes and followed by a sequence of about 216 earthquakes that are clustered along a northwest-southeast trending seismicity zone. In the northern part of Botswana, most of the detected seismic events are approximately aligned with the northern tip of this alignment located at the suggested southwestern extension of the East African Rift System (EARS). The EARS is one of the most active and extensive continental rift systems located in East Africa, which is gradually splitting the African continent in two. From the identified seismic events in Botswana and adjacent countries, results suggest that the seismic activity observed in central Botswana might be related to the seismicity in northern Botswana and eastern South Africa. Thus, leading to the conclusion that the southwestern branch of the EARS might be extending southwards from northern to south-eastern Botswana.

Acknowledgements

I would like to express my sincere gratitude to my supervisor Dr. Hanneke Paulssen for entrusting me with this research project, and for her continuous support and guidance. I would also like to thank Gert-Jan van den Hazel from the Royal Netherlands Meteorological Institute (KNMI) for the technical support with SeisComP3 software package. Thanks also go to the staff members in the seismology group at Utrecht University for their support and for installing the NARS-Botswana seismic network.

Special thanks to my family back home in Malta, for their support, love and continuous encouragement throughout my years of study. Finally, I would like to express my profound gratitude to my fiancé and his parents for their invaluable moral support, care, love and patience throughout this project.

Contents

List of Figures

List of Tables

1. Introduction

Botswana is a country in southern Africa characterised by low-to-moderate level of seismic activity with magnitudes mostly below 5.0 (Alabi et al., 2012). The geology of Botswana consists of Archean Cratons to the northwest and east of the country with tectonic mobile belts and sedimentary basins in between that evolved during different geological times, mostly throughout the Proterozoic phase (Begg et al., 2009). Currently, much of the bedrock geology of Botswana is still unclear mostly due to the large amounts of Kalahari sands covering the country (Simon et al., 2012).

Botswana's major seismic history has been initiated by two large earthquakes in 1952 (Simon et al., 2012), occurring in one of the world's largest inland deltas, the Okavango delta region (ODR), the north-western part of Botswana (Kinabo et al., 2007). Most of the seismic activity recorded in the interior of southern Africa is concentrated along the East African Rift System (EARS), one of the most active and extensive rift systems on the Earth's surface (Midzi et al., 2018). Previous seismicity studies of southern Africa showed that the ODR is one of the most seismically active regions in Botswana in which recorded earthquakes are associated with a set of northeasterly striking normal faults (e.g. Reeves, 1972 and Scholz et al., 1976). This led various scientists to suggest that the ODR represents a southwestern continuation of the EARS and thus, an incipient continental rift, referred to by many, as the Okavango Rift Zone (ORZ) (e.g., Kinabo et al., 2007; Leseane et al., 2015).

The motivation behind this study arose from the moment magnitude (M_w) 6.5 earthquake which struck the Moiyabana area in central Botswana unexpectedly on April 3rd, 2017. This large intraplate normal faulting earthquake ruptured a blind fault in Botswana, within the Limpopo-Shashe Mobile Belt, situated between the Kaapvaal and Zimbabwe Cratons (Bouwman, 2019). While most of the global seismicity occurs along plate boundaries, where most of the tectonic strain is released, this earthquake occurred inside the African continental plate, more than a thousand kilometres away from the nearest plate boundary (Albano et al., 2017). Although strong intraplate seismic events are very rare, the occurrence of these events indicates that the continental lithosphere is not completely stable and is associated with seismic hazards (Bouwman, 2019). As reported by Bouwman (2019), the mainshock was followed by 79 aftershocks with magnitudes between local magnitude (M_L) 2.5 and body wave magnitude (m_b) 5.0. Potential foreshocks were also investigated by Gardonio et al. (2018) using a template matching technique at teleseismic distances from the mainshock. Observations led Gardonio et al. (2018) to discover in total 14 foreshocks.

Most of the seismicity data we have before the NARS-Botswana network was installed in 2013 is based on recorded events on networks situated outside of Botswana. Therefore, some seismic events may have gone unreported while others may have been poorly located. A temporary network was installed to monitor the local seismicity in the ORZ. Thus, recorded seismicity data may be biased towards the northwestern part of Botswana (Simon et al., 2012; Pastier et al., 2017). Consequently, some seismically active areas, like the Moiyabana area, were invisible to previous studies. Due to all these factors, it was deemed necessary to carry out a more reliable assessment of the seismic activity in Botswana. Hence, the main aim of this study is to detect and reliably locate seismic events using data recorded by the NARS-Botswana seismic network. The distribution of seismic events is further investigated to understand how clusters of events might relate to the local geology, and to determine whether a seismic pattern exits within Botswana and/or in relation to adjacent countries. The origin time, location and magnitude of each detected event will be calculated automatically and documented in a reliable earthquake catalogue for Botswana. This earthquake catalogue is essential for the seismic hazard assessment and earthquake risk mitigation throughout the country.

This chapter will discuss in detail the main geological units in Botswana, the geological structure of the EARS and Botswana's currently known seismicity, along with information about the NARS-Botswana seismological network, the software used and the aim of this study.

1.1 Tectonic and geologic setting

Botswana is centrally positioned on the Precambrian shield of southern Africa (figure 1.1) (Simon et al., 2012). It consists of various tectonic features dominated by two main stable cratonic blocks, the Kalahari Craton to the east and southeast, comprising of the Kaapvaal and Zimbabwe Cratons, and the Congo Craton to the northwest (figure 1.2). Surrounding these Cratons are several younger mobile belts and sedimentary basins that formed through a succession of amalgamation and rifting processes (Key and Ayres, 2000; Begg et al., 2009; Fadel, 2018). There is still significant uncertainty as to the extent and nature of these tectonic units (Moorkamp et al., 2019; Fadel, 2018), mainly because 70% of the country is covered by the Kalahari sands (Simon et al., 2012). The understanding of southern Africa's crustal structure has been a major objective of research programmes by various institutions (Wright and Hall, 1990).

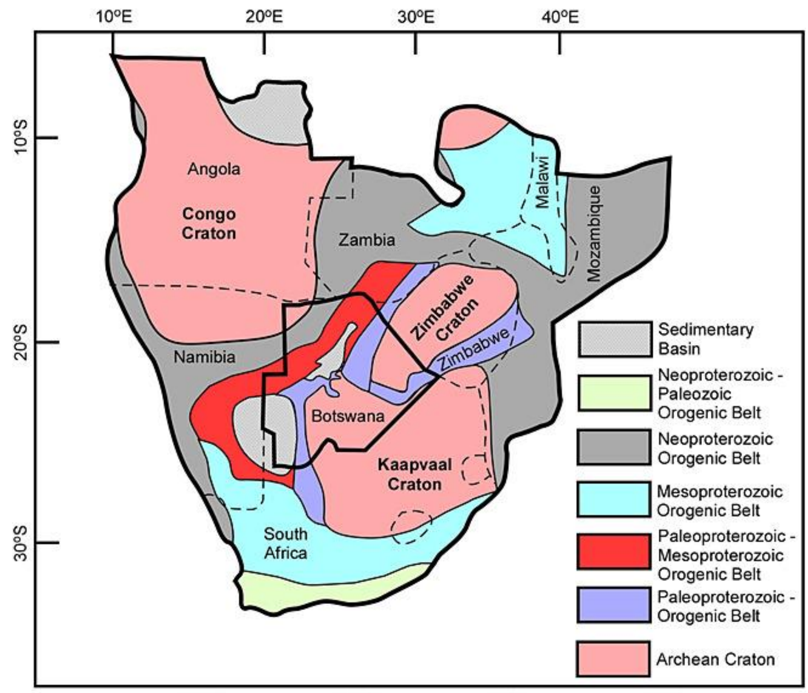

Figure 1.1. Precambrian tectonic map of southern Africa, with Botswana in the centre and its tectonic units that developed during geologic times (Leseane et al., 2015).

Botswana hosts one of the world's largest inland deltas, the Okavango Delta, located to the northwest. This delta is a result of tectonic activity associated with the rifting in the Okavango rift zone (ORZ) (Kinabo et al., 2007). The ORZ encompasses several northeast striking half-grabens (figure 1.2), considered by some to be the final extension of the southwestern branch of the East African Rift System (EARS), a major geodynamic feature which separates the African continent into two tectonic (sub)plates (e.g. Scholz et al., 1976, Modisi et al., 2000, Kinabo et al., 2008, Bufford et al., 2012). Thus, it is assumed to be an incipient rifting zone (Leseane et al., 2015). However, uncertainties remain whether this ORZ is actually part of the southwestern continuation of the EARS.

In the following subsections the general tectonic and geological units in Botswana are discussed in detail.

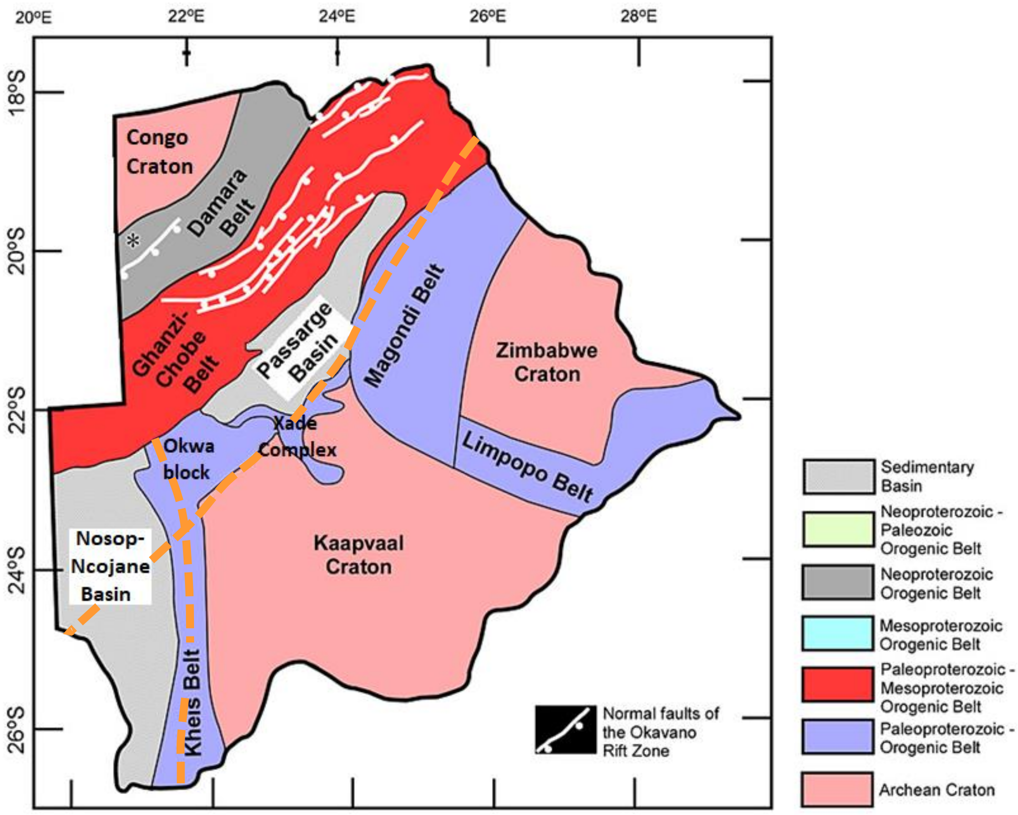

Figure 1.2. Precambrian tectonic map of Botswana showing the Archean Cratons and Proterozoic orogenic Belts adapted from Leseane et al. (2015). The white lines in the northwest of the map represent the northeasterly trending fault system of the Okavango rift zone and the two orange dashed lines, from Fadel (2018), form the Makgadikgadi and Kalahari line which together represent the Kalahari Suture Zone.

1.1.1 Cratons and Province

1.1.1.1 Kalahari Craton

A large part of Botswana is underlain by the Archean Kalahari Craton. This composite Craton comprises of the Kaapvaal and Zimbabwe Cratons (figure 1.2), two stable cratonic blocks that are separated by the Limpopo Mobile Belt (Begg et al., 2009; Midzi et al., 2018).

The Kaapvaal Craton is the oldest tectonic unit in Botswana, which formed and stabilized between 3.7 and 2.7 Ga ago (de Wit et al., 1992). Much of this craton is covered by upper Archean basins and several distinct geological terranes, with the oldest rocks located in the south-eastern part of the craton and the youngest in the western part. This craton mainly comprises of granitoids with gneisses and narrow green stone belts (Begg et al., 2009). The extensive cover of Karoo and Kalahari strata is situated north of the east-northeast trending Zoetfontein fault (fault number 2 in figure 1.3) (McCourt et al., 2004), a fault which Reeves (1978) interpreted as the northern boundary of the Kaapvaal Craton. However, Corner and Durrheim (2018) suggested that this interpretation refers more to a change in the crustal level within the Kaapvaal Craton, with a possible downthrown side to the north.

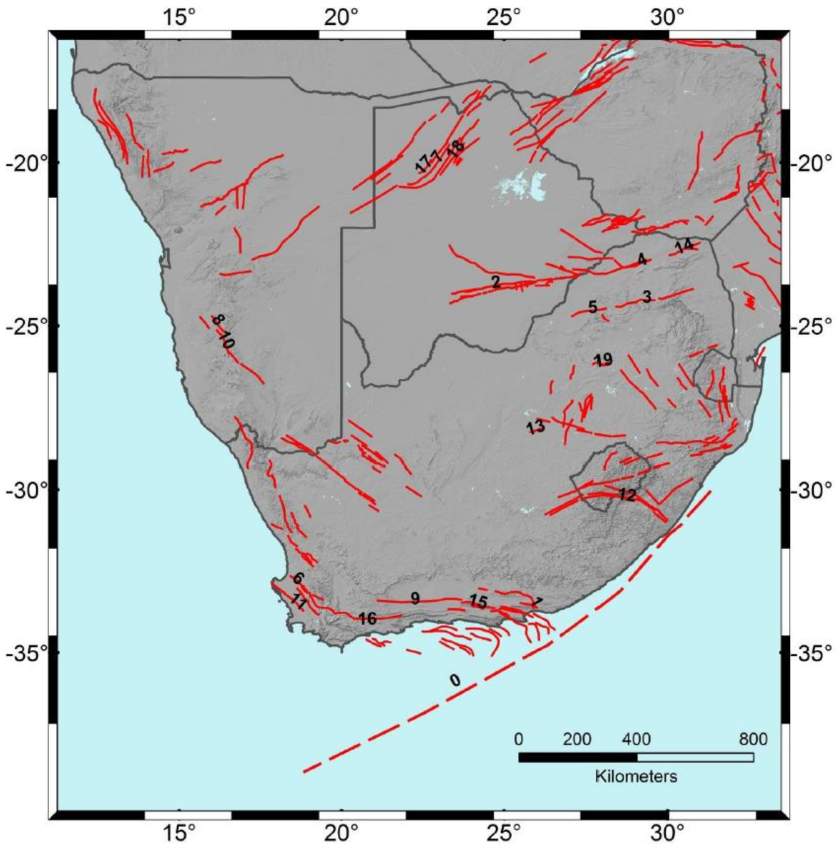

Figure 1.3. Map of Southern Africa showing the major faults in red from Mulabisana (2016). Some of these faults are labelled with black numbers and documented in Table 1.1.

The Zimbabwe Craton, on the other hand, consists of twenty-six greenstone belts which make up about 20% of the craton, while the rest of the craton consists of granite-gneiss complexes. The oldest rocks of this craton have an age of $3.57 - 3.37$ Ga (Jelsma and Dirks, 2002). The south-western part of this craton extends into eastern Botswana (figure 1.2) however, its full extent in Botswana is still unknown (McCourt et al., 2004).

Table 1.1. Fault names in Southern Africa corresponding to the numerical labelling in figure 1.3 (Mulabisana, 2016).

Fault Numbers	Fault Names
0	Agulhas
1	Zuurberg
2	Zoetfontein
3	Zebediela
4	Tshipise
5	Thabazimbi
6	Piketberg-Wellington
7	Lecha
8	Kuiseb
9	Kango
10	Hebron
11	Colenso
12	Cedarville
13	Bultfontein
14	Bosbokpoort
15	Baviaanskloof
16	Worcester
17	Tsau
18	Thamalakane
19	Rietfontein

1.1.1.2 Congo Craton

It is possible that the south-western part of the Congo Craton, described as the Angolan Shield by McCourt et al. (2013), extends into the north-western part of Botswana (figure 1.2). The exact southern boundary of this craton in Botswana, as well as in neighbouring Zambia and northern Namibia has been the subject of ample speculation (Corner and Durrheim, 2018). The Congo Craton is made up of Archean and Paleoproterozoic rocks (Fadel, 2018; Ernst et al., 2013), with the Angolan Shield being a Paleoproterozoic basement terrane mostly comprising of granitoids along with a limited amount of Neo-Archean crust (Corner and Durrheim, 2018). It is widely accepted that around 2.05 Ga, the Congo and São Francisco Cratons in South America were connected together as a single cratonic block and remained together up until the break-up of Africa and South America about 130 Ma (Ernst et al., 2013).

1.1.1.3 Rehoboth Province

Located between between the Kheis-Okwa-Magondi Belt and the Neoproterozoic Damara orogenic system is the Rehoboth Province (figure 1.2), a puzzling area (Begg et al., 2009) due to its extensive cover by Kalahari sands (van Schijndel et al., 2014). A substantial part of the Rehoboth Province was formed during the Paleoproterozoic phase around 2.2 – 1.9 Ga, however, it is still unknown when this Province was fully assembled (van Schijndel et al., 2011). Originally, it was defined as a subprovince of the Namaqua Province located in Namibia and South Africa (van Schijndel et al., 2013). Later, Tinker et al. (2004) suggested that sometime between 1.93 and 1.75 Ga this Province was accreted to the Kaapvaal Craton.

In the southwest of Botswana, part of the Rehoboth Province is covered by the Nosop-Ncojane Basin (figure 1.2) (Key & Ayres, 2000), with the Ncojane Basin located at the northernmost part and the Nosop Basin farther to the south (Hoffe, 1996). The Nosop-Ncojane Basin is a thick sedimentary basin consisting of Nama Group sediments above Ghanzi Group rocks with a total thickness of more than 10 km (Key & Ayres, 2000). Beneath the Nosop Basin, a possible ancient craton (Maltahohe) has been considered to exist (Begg et al., 2009) whereas Wright and Hall (1990) have interpreted this as a western extension of the Kaapvaal Craton.

1.1.2 Mobile Belts

1.1.2.1 Limpopo Belt

The Limpopo Belt is an east-northeast trending high-grade metamorphic terrane formed as a result of the collision between the Kaapvaal and Zimbabwe Craton (figure 1.2) during the late Archean time (Van Reenen et al., 1987; Thomas et al., 1993; James and Fouch, 2002). To the west, the belt is covered by Kalahari sands, while Proterozoic and Phanerozoic sediments cover the east of the belt. This belt has been divided into three contrasting crustal zones (figure 1.4); the northern and southern Marginal Zones, and the Central Zone. The Northern Marginal Zone (NMZ) lies mainly in Zimbabwe, while the Southern Marginal Zone (SMZ) is exposed in South Africa (Gore et al., 2009). These two marginal zones are extensively deformed and include rocks related to adjacent Cratons (Begg et al., 2009). The Central Zone (CZ) is characterised by largely epicontinental rocks (Van Reenen et al., 1987) separated from the two marginal zones by the Triangle shear zones to the north and the Palala shear zone to the south of the CZ (Gore et al., 2009).

Based on gravity data interpretation, the extent of the Limpopo Belt has been redefined by Ranganai et al. (2002) to include the Shashe Belt, located northwest of the Magogaphate shear zone (figure 1.4). The area between the Shashe shear zone and the Lechana Fault, part of the Shashe Belt, has been defined as an extensional part of the NMZ in the Limpopo Belt, with the Shashe shear zone and the Northern Limpopo thrust as the boundary which separate the Limpopo-Shashe Belt from the Zimbabwe Craton (figure 1.4). On the other hand, the area between the Dinokwe thrust and the Mahalapye shear zone bounds the extensional part of the

SMZ, with the Dinokwe thrust and the Hout River shear zone separating the Limpopo-Shashe Belt from the Kaapvaal Craton (figure 1.4). The CZ of the Shashe Belt, which corresponds with the CZ of the Limpopo Belt, is separated from the marginal zones by tectonic discontinuities (Ranganai et al., 2002).

The Limpopo Belt boundaries are clearly distinct in Zimbabwe and South Africa however, little is known of how much it extends west within Botswana. Moreover, uncertainties remain about the boundaries of the Zimbabwe Craton, Limpopo Belt and Kaapvaal Craton in Botswana (Ranganai et al., 2002).

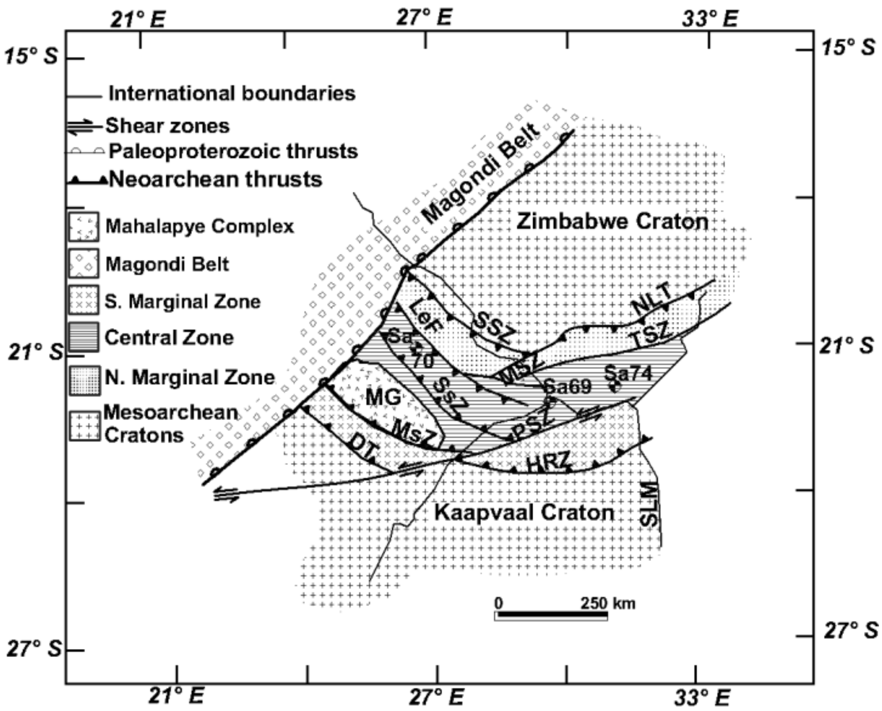

Figure 1.4 Tectonic map of the Limpopo-Shashe Belt showing the distribution of the three crustal zones in association to the Zimbabwe Craton, Kaapvaal Craton and Magondi Belt, based on surface geology and gravity data interpretation by Ranganai et al. (2002). DT = Dinokwe Thrust; HRZ = Hout River Shear Zone; LeF = Lechana Fault; MG = Mahalapye Granite; MSZ = Magogaphate Shear Zone; MsZ = Mahalapye Shear Zone; NLT = Northern Limpopo Thrust Zone; PSZ = Palala Shear Zone; SLM = Sabi-Lebombo Monocline; SSZ = Shashe Shear Zone; SsZ = Sunny Side Shear Zone; TSZ = Triangle shear zone.

1.1.2.2 Damara-Ghanzi Chobe Belt

Bounding the south-eastern margin of the Congo Craton, in the north of Botswana is the highly complex Damara Belt (figure 1.2) (Begg et al., 2009), consisting of a succession of highly metamorphosed sediments formed during the Neoproterozoic to early Paleozoic Pan-African Orogeny (Wright and Hall, 1990; Nascimento et al., 2017; Fadel, 2018). It is generally interpreted to have developed as a result of the collision between the Congo and Kalahari Cratons (550-500 Ma) (Meneghini et al., 2017).

Forming part of the southern margin of the Damara Belt, is the Ghanzi-Chobe Belt (figure 1.2) (Modie, 2000), consisting of a sequence of tightly folded, late Proterozoic metasedimentary rocks (Wright and Hall, 1990; Hoffe, 1996). Originally, the Ghanzi-Chobe Belt was formed as a rift basin in which volcano-sedimentary rocks were accumulated and developed through extensional tectonics associated with a continental collision along the Namaqua-Natal Belt. Later, during the Pan-African Damara Orogeny, the basin was exposed to post-depositional tectonic deformation that resulted in a fold and thrust belt (Modie, 2000).

In Botswana, the area between Mamuno, near the Namibia border, and Lake Ngami is referred to as the Ghanzi Ridge (Modie, 2000). To the east of the Ghanzi Ridge, between the Makgadikgadi Line and the Ghanzi-Chobe Belt, is the Passarge Basin (figure 1.2), filled with up to 15 km thick Ghanzi Group sediments (Key and Ayres, 2000; Haddon, 2005). The Passarge Basin is bordered by the Kalahari Suture Zone (KSZ) in the south (figure 1.2), a major thrust zone considered to be associated with the formation of the Kheis and Magondi Belts (Key and Ayres, 2000; Haddon, 2005; Fadel, 2018). The KSZ consists of granulite facies metamorphic rocks, however, nowadays various places are covered with thick Phanerozoic sediments from the Kalahari sands (Materna et al.,2019). The Kalahari and Makgadikgadi Lines are collectively referred to as the KSZ, with the northerly trending Kalahari Line thought to represent the western edge of the Kaapvaal Craton while the northeasterly trending Makgadikgadi Line likely to mark the northern boundary of the Kaapvaal Craton (Haddon, 2005). During the late Mesoproterozoic and Neoproterozoic times, this former thrust zone was believed to have been reactivated as a major rift fault with a northwest down throw. In fact, the presence of the two deep sedimentary basins; the Passarge and Nosop-Ncojane Basins, west of the KSZ indicate that the downthrow was very significant (Key and Ayres, 2000; Haddon, 2005).

Within the Damara-Ghanzi Chobe orogenic Belts is the Okavango Rift Zone (ORZ) (see section 1.1.3)(figure 1.2) (Leseane et al., 2015; Fadel, 2018), one of the most seismically active regions in Botswana (Midzi et al., 2018).

1.1.2.3 Kheis-Okwa-Magondi Belt

The composite Khesi-Okwa-Magondi Belt bounds the western margin of the Zimbabwe and Kaapvaal Cratons (figure 1.2) (Begg et al., 2009). The about 2 Ga old, north trending Kheis Belt runs along the western boundary of the Kaapvaal Craton in South Africa and Botswana (Schlüter, 2006; Oriolo and Becker, 2018). It is a fold-and-thrust belt comprising of low-grade metasedimentary and metavolcanic rocks (Haddon, 2005; Midzi, 2018). The boundary between the Kheis Belt and the Rehoboth Province is defined by the Kalahari Line, part of the KSZ (Oriolo and Becker, 2018).

To the northern edge of the Kheis Belt is the Okwa Inlier with a basement consisting of about 2.1 Ga metamorphic rocks, probably underlain by Archean rocks (Begg et al., 2009).The area surrounding the western part of the Zimbabwe Craton and the northwestern part of the Limpopo Belt is known as the Okwa-Magondi terrane, an enigmatic region due to unclear geological features that are covered by large amounts of Kalahari sands (Midzi, 2018). The early Proterozoic Magondi Belt, defining the western edge of the Zimbabwe Craton, is composed of a thick sequence of sediments and volcanic rocks (Begg et al., 2009). To the east, the Magondi

Belt unconformably covers rocks of the Zimbabwe Craton, whilst its western boundary is overlaid by younger sediments (Oriolo and Becker, 2018). In Botswana, the northwestern margin of the Magondi Belt is clearly distinguished by a significant geophysical feature, the Makgadikgadi Line which runs across central Botswana over a distance of about 1200 km (Key and Ayres, 2000). Crossing the Makgadikgadi Line is the Xade Complex, around 100 km long and 25 km wide, situated in central Botswana. It is entirely covered by various Kalahari sediment thicknesses and Karoo strata. Modelling and drilling information suggests that the Xade Complex is a layered basic Complex, consisting of both intrusive subvolcanic sheets and extrusive lavas (Pouliquen and Key, 2008). It has a unique Y-shape form, with its northeastern part aligned with the Makgadikgadi Line, its southern part parallel to the Kalahari Line, and the northwestern part following a trend similar to the Okwa block (Haddon, 2005).

1.1.3 The Okavango Rift Zone

Located in northwestern Botswana, the Okavango Rift Zone (ORZ) consists of several northeasterly trending faults including, the Thamalakane, Kunyere, Linyanti, Chobe, Nare, Phuti, Lecha, Tsau, Gumare and Mababe faults (figure 1.5) with the most active faults situated in the southeastern boundary (Kinabo et al., 2007; Shemang and Molwalefhe, 2011; Rankin, 2015; Pastier et al., 2017). Kinabo et al., 2007 suggest that these faults are still at an early stage of development. Together, they define a northeast-southwest zone that is about 400 km long, with the west-northwest trending dextral Sekaka Shear Zone (SSZ) and the Gumare fault in the southwest and the Linyanti and Chobe faults in the northeast. The northwest and southeast fault boundaries of the ORZ appear to be represented by the Gumare and Nare faults which define a zone of extension around 150 km wide (Kinabo et al., 2007; Rankin, 2015). Based on calculated displacements of the dykes across the faults, Kinabo et al. (2007) deduced that the Gumare, Tsau, and Lecha faults are normal faults dipping to the southeast, whereas the Kunyere, Mababe, Thamalakane, Phuti, Nare, Liyanti, and Chobe are northwest dipping normal faults.

The seismically active ORZ has been described as an incipient continental rift (Kinabo et al., 2007; Kinabo et al., 2008; Mulabisana, 2016; Shemang and Molwalefhe, 2011) and some even suggested it to be a continuation of the southernwestern branch of the East African Rift System (EARS) (e.g., Scholz et al., 1976, Modisi et al., 2000, Kinabo et al., 2008, Bufford et al., 2012; Leseane et al., 2015) (see section 1.1.4). However, these interpretations have lately been challenged by Pastier et al. (2017). The ORZ appears to be developing within a large structural depression known as the Makgadikgadi-Okavango-Zambezi (MOZ) basin, a basin consisting of alluvial fan deposits as well as deeper palaeo-lake sediments in structural depressions or subbasins (Kinabo et al., 2007; Shemang and Molwalefhe, 2011). One of the world's largest inland alluvial fans, the Okavango Delta (∼22 000 km^2) is situated within the ORZ, supporting the biggest wetland in southern Africa. The formation of this alluvial fan is believed to be related to neotectonic activity associated to the rifting in the ORZ which strongly affects the drainage and geomorphology of the MOZ basin (Kinabo et al., 2007; Shemang and Molwalefhe, 2011; Leseane et al., 2015).

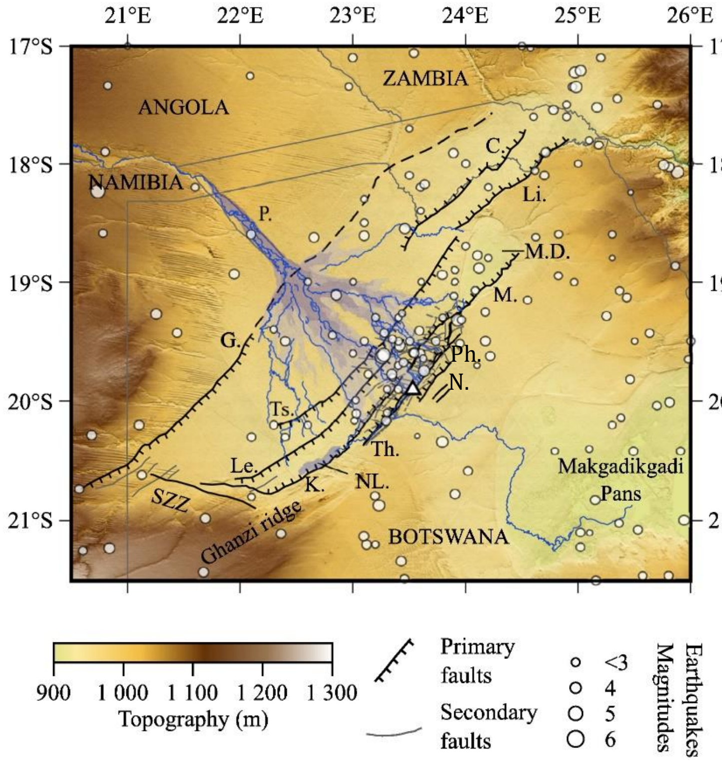

Figure 1.5. Okavango Rift Zone (ORZ) topographic map (SRTM30) demonstrating the location of the main faults and their corresponding dipping direction, the local seismicity with magnitude greater than 3 (based on unreviewed ISC data) and inundated regions from Pastier et al. (2017). C.: Chobe fault, G.: Gumare fault, K.: Kunyere fault, Le.: Lecha fault, Li: Linyanti fault, M.: Mababe fault, M.D.: Mababe Depression, N.: Nare, N.L.: Lake Ngami, P.: Panhandle, Ph.: Phuti, SSZ: Sekaka Shear Zone, Th.: Thamalakane fault, Ts.: Tsau fault.

1.1.4 East African Rift System

Splitting the African continent into two tectonic (sub)plates, called the Somali Plate and the African (Nubian) Plate is the East African Rift System (EARS) (Pastier et al., 2017). South of the main Ethiopian rift, the EARS is divided into two specific branches, known as the eastern and western branches (figure 1.6). The volcanically active eastern branch of the EARS is the oldest (>25 to < 1 Ma) of the two and extends from the Afar Depression in Ethiopia to Kenya and central Tanzania through the Kenya and Turkana rifts. On the other hand, the less evolved, younger and much less volcanic western branch (<15 Ma) extends from Lake Albert in Uganda to Lake Malawi in central Mozambique through various discontinuous rift basins (Kinabo et al., 2007; Pastier et al., 2017). The approximately 50-100 km long and 40-100 km wide individual rift basins are filled by extensive amounts of sediments consisting of fluvio-deltaic and lacustrine sediments and/or volcanics and volcanoclastics. Individual rift basins of each branch are connected together by transfer faults/accommodation zones (Kinabo et al., 2007). Some authors agree that a third branch of the EARS, known as the southwestern branch, extends southwest from Lake Tanganyika and adds the ORZ as its southern terminus (e.g. Scholz et al., 1976; Modisi et al., 2000; Kinabo et al., 2007; Leseane et al., 2015).

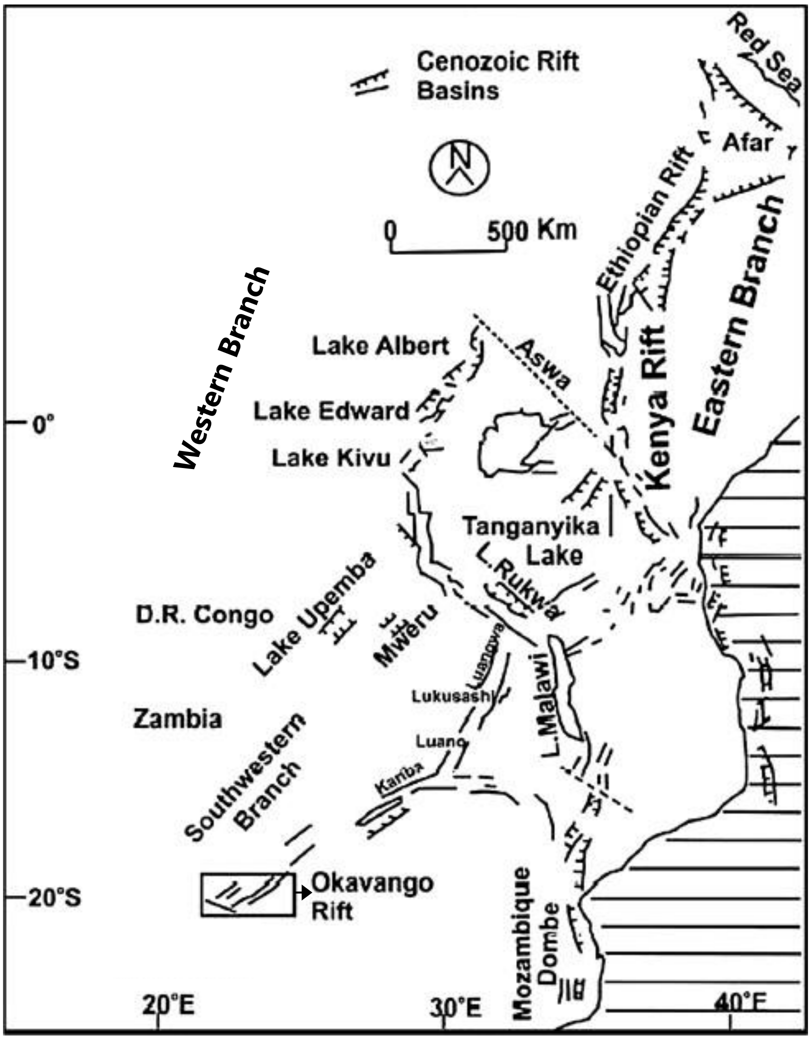

Figure 1.6. Map of the East African Rift System showing the eastern, western and southwestern branches from Kinabo et al. (2007). The black box indicates the location of the Okavango Rift Zone, in northwestern Botswana.

Initially, Du Toit (1927) suggested that there is a relationship between the EARS and the ORZ, then Fairhead and Girdler (1969) proposed that the EARS extended in Botswana in a north-south orientation. Later, an extension of the EARS along a northeast-southwest axis was postulated by Reeves (1972). However, Reeves (1972) suggested the central Kalahari, 250 km south from the ORZ, as the extensional part of the EARS. It was Scholz et al. (1976) who proposed the current assumption that the ORZ is the terminus of the southwestern extension branch of the EARS (Scholz et al., 1976; Pastier et al., 2017).

1.2 Botswana's seismicity

Seismic activity in Botswana was first recognised between 1949 and 1951, thanks to the first seismographic network installed in South Africa (Reeves, 1972; Simon et al., 2012). Between 1952 and 1953, 33 events, most of them greater than magnitude 5.0, were observed in the ORZ. It was during this period that the seismicity in Botswana was first accentuated due to the 6.1

and 6.7 Local magnitude (M_L) events, occurring in the ORZ on September 11th and October 11th 1952, respectively. During 1954 to1955, only two magnitude 5.0 events were observed in northern Botswana and in the subsequent ten years, three other minor events were located in the same region (Reeves, 1972). Between 1959 and 1965, the first seismic network in Zimbabwe was set up by the Rhodesia Meteorological Services. Initially, the network consisted of three stations, with Bulawayo station as the closest seismic station to Botswana, around 400 km away from the ORZ (Scholz et al., 1976). Later in 1968, two more stations were added and another one in 1971 (Reeves, 1972). This seismic network led to the discoveries by Reeves (1972) and Scholz et al. (1976), who both noticed high seismic activity in the ORZ and suggested a correlation between the EARS and Botswana's seismicity. However, Reeves (1972) postulated the Kalahari axis, a line 250 km south of the ORZ, as the EARS extension while Scholz et al. (1976) attributed the high seismic activity in the ORZ to the southwestern extension of the EARS (Pastier et al., 2017). From 1950 to 1991, a total of 154 earthquakes with various magnitudes were detected in Botswana (Simon et al., 2012). In 1993 the LBTB seismic station, near Lobatse in south-eastern Botswana, was deployed and operated by the U.S. Geological Survey (USGS) as part of the Global Telemetered Seismograph Network (GTSN) (U.S. Geological Survey, 2019). This was the first broadband station installed in Botswana to monitor local seismic events and underground explosions. More recently, between the period 2005 to 2007, a network of twenty to thirty permanent seismic stations was installed by the AfricaArray (AA) around eastern Africa, to monitor the EARS and seismicity in southern Africa. However, none of these stations were placed in Botswana. Later, during 2008 and 2010, the AA network was expanded to include other parts of Africa, one of these was the temporary station MAUN in northern Botswana (AfricaArray, 2010). The addition of more stations resulted in an increase of detected seismic events which are available on the International Seismological Centre (ISC) database (Pastier et al., 2017). Other temporary seismic networks were also deployed in Botswana, however, these were only used to understand Botswana's geology and not to detect earthquakes (Carlson et al., 1996; Gao et al., 2013).

Little is known and documented about the seismic activity of a larger coverage of Botswana, mainly due to the paucity of seismometers on the African continent (Pastier et al., 2017; Nthaba et al., 2018). Due to this, some earthquakes might have been recorded by only one seismic station. However, the ISC review process requires each earthquake to be detected by at least two stations in order to publish it (Pastier et al., 2017). This raises concern as some of the available ISC data for events detected in Botswana might be unreliable due to data being based on events recorded by a very few amount of stations, mostly located outside of Botswana. Additionally, local seismic stations were temporally installed to monitor seismic activity only in the ORZ (Simon et al., 2012), making any recorded data instrumentally biased to the northwestern part of Botswana. This bias might have hidden major areas of seismicity in Botswana.

Pastier et al. (2017) used the unreviewed data set from the ISC, between 2004 and 2016 to plot events with magnitude greater than 3.0 for Southern Africa (figure 1.7). To prevent any induced seismicity due to man-made activities, no events with magnitude less than 3.0 were used. From this study, some regions revealed particular seismic activity which other studies did not observe before, such as the previously assumed aseismic Ghanzi ridge and central Kalahari, south of the Ghanzi ridge. In fact, axes of earthquake clusters in a northwest-southeast orientation were identified by Pastier et al. (2017), with one of them starting from eastern Namibia, passing through central Kalahari and ending in northeastern South Africa. Seismic activity within the ORZ was concentrated along the southeastern edge of the delta, in between the NE-SW striking Tsau and Thamalakane faults. The rate of seismicity recorded between these faults may be attributed to the large quantity of water which is contained in them, as well as the continued inflow of extensive amounts of water into the delta (Nthaba et al., 2018). Significant seismic activity was also observed in the region of the Mababe Depression to the northeast of the delta, whereas Lake Ngami to the southwestern end, appeared to be relatively aseismic (Pastier et al., 2017). Seismicity appears to be very low in the central region of the delta and also along the NE-SW striking Gumare fault. However, some events were recorded on the presumed extension of the Gumare fault, northeast of the delta (see black dashed line in figures 1.5 and smaller dashed line in figure 1.7) up till the northern part of the Linyanti swamps (Pastier et al., 2017; Nthaba et al., 2018).

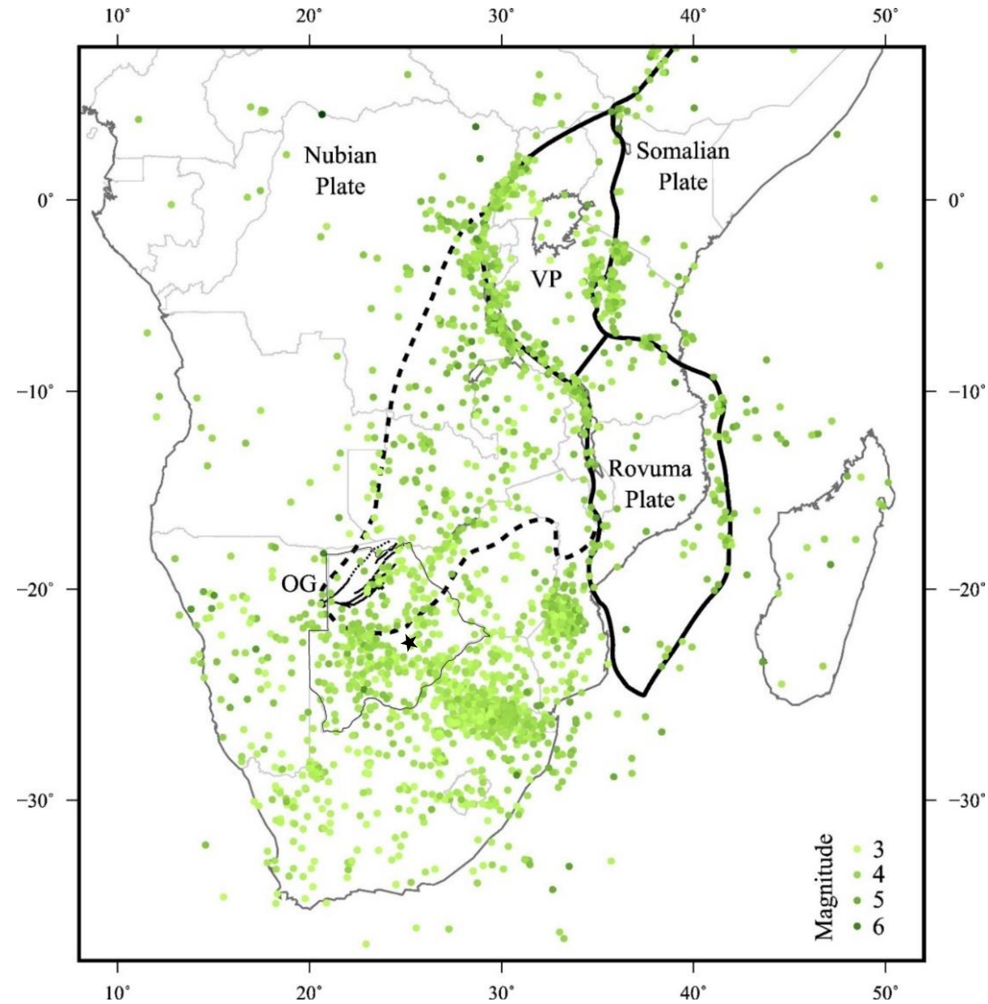

Figure 1.7. Southern Africa map showing the seismicity distribution (M ≥ 3) between 2004 and 2016 from Pastier et al. (2017). These recorded seismic events are based on unreviewed data from the ISC database. The dashed region represents the poorly defined southwestern extension branch of the EARS referred to as the South-Western Extension Area (SWEA) by Pastier et al. (2017). The black star in Botswana represents the location of the M_w 6.5 normal-faulting earthquake in 2017. OG: Okavango Graben, VP: Victoria Plate.

From August 2013 to December 2014, Pastier et al. (2017) identified from the unreviewed ISC database more than 400 events with magnitudes mostly between 3 and 5.6, in north and west Botswana (figure 1.8). During this period, only 26 events were recorded in the ORZ. In contrast, considerable seismic activity was detected in the central Kalahari, a region corresponding to a ENE striking Karoo failed rift. There was no specific earthquake concentration observed along the Zoetfontein fault (refer to figure 1.3 for fault location) (Pastier et al., 2017).

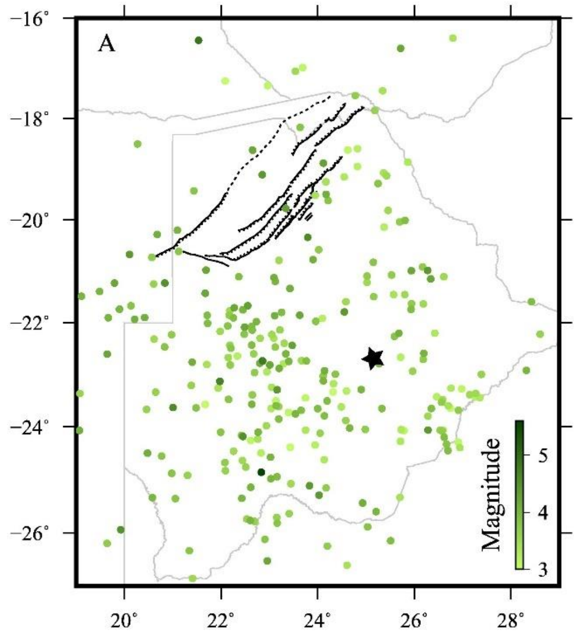

Figure 1.8. Seismicity of Botswana by Pastier et al. (2017) from August 2013 till December 2014 based on unreviewed data from the ISC. The black star represents the location of the M_w 6.5 normal-faulting earthquake in 2017.

Whilst Botswana is a country with low local level of natural seismicity, moderate to large earthquakes have been mainly associated with the ORZ (Kwadiba and Ntibinyane, 1993). However, due to the poor seismic network distribution, some seismically active regions in Botswana may well have remained invisible to a lot of previous studies. Recently, this hypothesis was supported by the M_w 6.5, normal-faulting earthquake on April 3rd, 2017, in central Botswana, near the village Moiyabana. This earthquake occurred in a region with low historical seismicity and far away from any identified active fault (Kolawole et al., 2017; Albano et al., 2017; Gardonio et al., 2018; Midzi et al., 2018; Bouwman, 2019). Due to its lower crust depth (around 25 to 30 km deep), Gardonio et al. (2018) suggested that this intraplate earthquake might have been triggered by elevated, sub-lithostatic, pore fluid pressure. Moreover, by applying a template matching approach to continuous signals recorded at teleseismic distance from the mainshock, Gardonio et al. (2018) also detected 14 foreshocks. For the same time interval in which these foreshocks were detected, the ISC online Bulletin only documented one magnitude 4.1 earthquake about 120 km away from the mainshock. On the other hand, Kolawole et al. (2017) and Bouwman (2019) proposed that this earthquake and its aftershocks occurred due to extensional reactivation of the northeast dipping Moiyabana fault. This fault forms part of an ancient zone of weakness within the Limpopo-Shashe orogenic belt that resulted from the collision of the Kaapvaal and Zimbabwe Cratons (Kolawole et al., 2017; Bouwman, 2019).

The exploitation of natural resources, such as minerals and hydrocarbons has contributed enormously to the generation of seismic events (Albano et al., 2017). Up to 40 induced seismic events, or more, have been identified per month in southern Africa (Alabi et al., 2012). Botswana is a country abundant in various natural resources, including diamond, gold, coal, copper, nickel and soda ash (known also as sodium carbonate) (figure 1.9). Since its discovery in 1967, diamond has been the most important mineral resource in the country. In fact, the richest diamond mine in the world is considered to be the Jwaneng diamond mine, located in south-central Botswana (AZoMining, 2012). Deep-level mining as is established in South Africa consists of working into the earth's crust where naturally occurring seismicity takes places. To control and not aggravate the occurrence of induced seismic events, these man-made activities are closely monitored and regulated (Alabi et al., 2012).

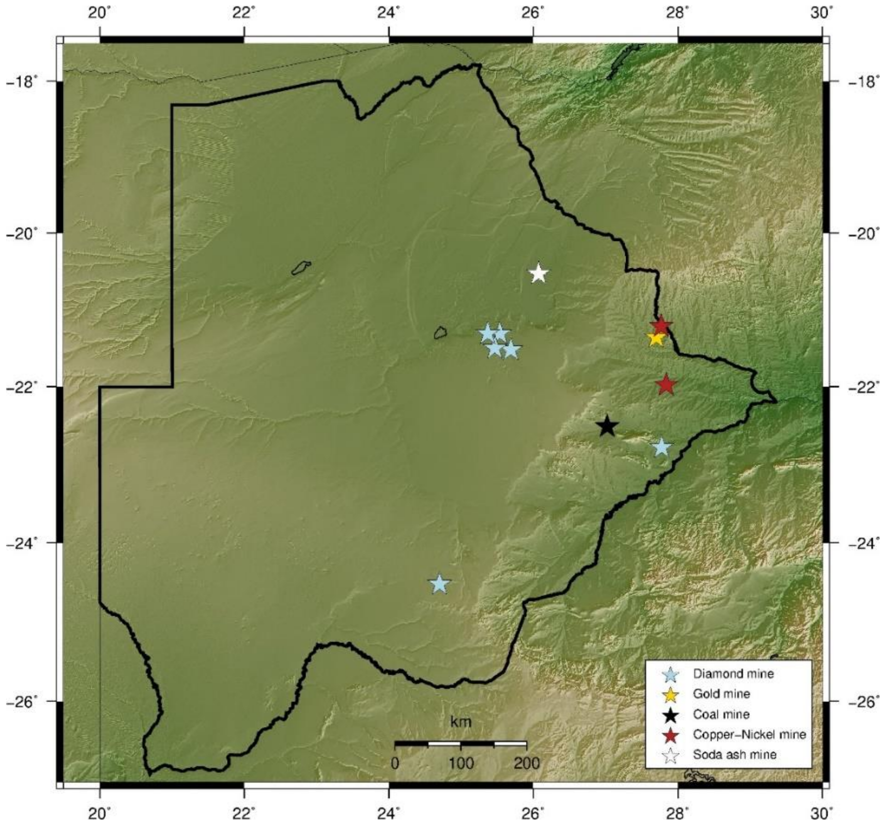

Figure 1.9. Mine locations in Botswana (KnowBotswana, 2010; Gwebu, 2013; Lucara Diamond, 2019).

The occurrence of natural seismicity in Botswana seems to be guided by multiple tectonic units (discussed in section 1.1), with events mainly located in the mobile belts. Most of the seismic activity in Botswana has been mainly associated with the ORZ (Midzi et al., 2018). However, it has now become clear from the 2017, M_w 6.5 earthquake and its aftershocks that other regions in the country, like central Botswana, are also seismically active. This raises the need for a more reliable assessment of the seismic activity throughout Botswana which is indeed the purpose of this study (as explained in section 1.5). As a result, previous unknown faults and regions of increased hazard can later be identified.

1.3 NARS-Botswana seismological network

The NARS-Botswana seismic network was installed in June 2013 and operated by the seismology group of the Faculty of Geosciences, Utrecht University until March 2018. The scientific purpose of the NARS-Botswana temporary project was to reveal the structure of the crust and upper mantle beneath Botswana in order to obtain a better understanding of its complex tectonics (Fadel, 2018). Since March 1st 2018, the Botswana Geoscience Institute (BGI) was assigned the ownership of the NARS-Botswana stations, making the stations part of the Botswana Seismological Network (BSN) (Seismology group, Utrecht University, 2015).

The network comprises a total of 21 broadband seismic stations (Table 1.2) distributed across most of the country, except for poor station coverage in the southwestern part of Botswana. Figure 1.10 shows the location of each of these stations, covering all the diverse geological and tectonic units in Botswana. For further details about the setup and equipment used in the NARS-Botswana seismic network, one can refer to the NARS-Botswana website (Seismology group, Utrecht University, 2015).

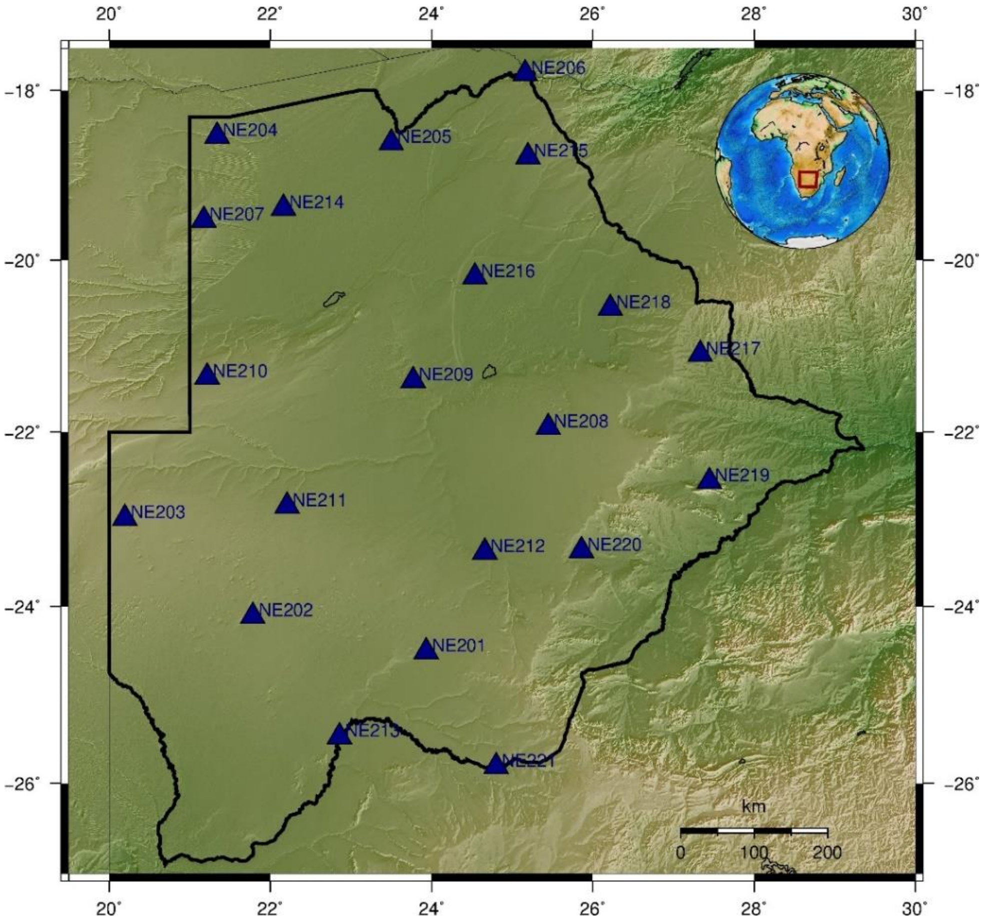

Figure 1.10. The NARS-Botswana seismological network (Seismology group, Utrecht University, 2015).

Table 1.2. Location, sensor type and installation date of the NARS-Botswana stations from the NARS-website by the Seismology group, Utrecht University (2015).

Station	Location	Sensor	Latitude (° N)	Longitude (° E)	Altitude (m)	Installation (year.day number)
NE201	Sekoma	Trillium 120p	-24.51535	23.93279	980	2013.324
NE202	Lokgwabe	Trillium 120p	-24.11352	21.78230	1153	2014.011
NE203	Kole	Trillium 120p	-22.99307	20.19555	1313	2014.015
NE204	Xaudum	STS-2	-18.53956	21.33822	1060	2015.077
NE205	Selinda	Trillium 120p	-18.62089	23.50048	961	2015.241
NE206	Kasane	Trillium 120p	-17.80017	25.16189	1006	2015.239
NE207	Qangwa	Trillium 120p	-19.52957	21.17400	1094	2015.327
NE208	Khwee	Trillium 120p	-21.94641	25.44691	1083	2014.044
NE209	CKGR	Trillium 120p	-21.40355	23.77177	1005	2015.073
NE210	Groot Laagt	STS-2	-21.36192	21.21571	1198	2015.071
NE211	Kacgae	Trillium 120p	-22.85382	22.20679	1153	2013.328
NE212	Kaudwane	Trillium 120p	-23.38039	24.66079	1038	2014.046
NE213	Phepeng	Trillium 120p	-25.47553	22.85729	1030	2013.327
NE214	Gumare	STS-2	-19.38931	22.16246	985	2015.326
NE215	Bottlepan	STS-2	-18.78417	25.19601	1035	2015.324
NE216	Phuduhudu	STS-2	-20.19568	24.53719	956	2014.040
NE217	Borolong	Trillium 120p	-21.09968	27.33424	1047	2015.236
NE218	Sowa	Trillium 120p	-20.56285	26.21785	941	2014.041
NE219	Moremi	Trillium 120p	-22.56967	27.44682	911	2015.235
NE220	Lephepe	Trillium 120p	-23.36303	25.85961	1020	2013.053
NE221	Mmakgori	Trillium 120p	-25.81185	24.80085	1158	2013.320

1.4 Software used

For the detection and location of seismic events in Botswana, the Seismological Communication Processor 3 (SeisComP3) software package has been used. SeisComp3 is one of the most broadly used software packages for seismological data acquisition, data processing and real-time data exchange. Initially, this software was developed for the GEOFON network and eventually it further extended within the MEREDIAN project coordinated by GEOFON/GFZ Potsdam and ORFEUS. Additional functions and major changes in the architecture of the software were later implemented by the GITEWS (German Indian Ocean Tsunami Early Warning System)/GEOFON development group, resulting in the upgrade of SesisComP to version 3 (Pesaresi, 2011; GFZ Potsdam, 2018). Although SeisComP3 is mostly intended to monitor real-time earthquake data through direct connection with data loggers and digitizers (Bormann et al., 2014), in this research off-line data processing and analysis was applied. This is mainly due to the fact that the NARS-Botswana data was already acquired and stored into the NARS system at Utrecht University.

SeisComP3 follows a modular approach with each module performing a discrete task. All modules are connected through a messaging system and a common database (Hanka et al., 2010; Pesaresi, 2011; GFZ Potsdam, 2018). These modules assist in rapid automatic and manual data processing and offer an interactive review of results (Weber et al., 2007).

1.5 Aim of project

The main aim of this study is to carry out a more reliable assessment of the seismicity throughout Botswana using the NARS-Botswana data from January 2014 till March 2018. Data is processed and analysed using the SeisComP3 software package, which uses automatic and manually picked P-wave arrival times to detect and locate seismic events. As a result, an earthquake catalogue spanning around four years of NARS-Botswana data is created to assist in the quest of seismic hazard and risk mitigation for Botswana.

The seismicity in Botswana is further analysed to investigate how the clustering of seismic events might relate to the local geology. To examine the variation of seismic activity in Botswana and assess the completeness of the earthquake catalogue, a magnitude-frequency relation plot is developed. From this plot the relative size distribution of events (b −value) and the rate of seismic activity in the country are estimated. Moreover, any seismic pattern within Botswana and/or in relation to adjacent countries is explored, with particular emphasis on whether a correlation exists between the ORZ and the suggested southwestern branch of the EARS (Scholz et al., 1976; Modisi et al., 2000; Kinabo et al., 2007; Leseane et al., 2015).

Since there was only one permanent seismic station operating in Botswana before the NARS-Botswana network was deployed, many seismic events have either been missed or mislocated. With this regard, seismic events detected and located in Botswana by SeisComP3 are compared with event locations listed in the ISC on-line bulletin (downloaded January 2019) for the same time interval. Considering that multiple seismicity studies for Botswana are based on the ISC unreviewed data (e.g. Pastier et al., 2017), this comparison will allow us to assess the reliability of the unreviewed ISC catalogue.

2. Methodology

Reliable automatic procedures for detecting and locating seismic events are essential in exploring, understanding and forecasting of earthquake occurrence. Determining the accurate location of any source is one of the most major tasks in seismology (Havskov et al., 2011), particularly as these hypocenters help to reveal information about the geology nearby, for example, to identify faults that ruptured in an area. Therefore, having accurate hypocenter locations will enable us to understand better the structures of the fault systems (Li, 2017).

Standard earthquake catalogues, such as the one from the ISC, typically report locations that are off by approximately 25 km in horizontal position and depth (Shearer, 2009). This is mainly due to errors contaminating the data owing to a variety of possible factors, such as inaccuracies in the stations' clocks, misidentification of the first P-wave arrival, network geometry and the quality of the seismic velocity model used (Stein and Wysession, 2003; Husen and Hardebeck, 2010; Bouwman, 2019).

In this study, an event detector is applied in SeisComP3 to all available NARS-Botswana data so that a rough estimation of the first P-wave arrival is obtained. Generally, this technique requires the data to be filtered prior to detecting changes in signal amplitude. After a seismic event has been identified, a more precise P-phase picker is implemented so that reliable P-wave arrival time measurements are obtained. Ultimately, all incoming automatic and manual P picks are used in SeisComP3 to automatically locate detected seismic events. To ensure the robustness of the automated location, a large number of automated P picks is usually required. In this chapter, the algorithms implemented in SeisComP3 for the detection and location of a seismic event are thoroughly discussed. Details about the used modules and parameter settings in SeisComP3 will be discussed in the next chapter.

2.1 *P*-phase picking

Accurate and precise picking of the first P-wave arrival is of great importance in event location and recognition. Much of our current knowledge about the seismicity and structure of the Earth is based on manual picking of onset times. However, this method has proven to be highly subjective as well as extremely time consuming, especially when it comes to large data sets (Munro, 2004). Hence, such large data sets call for an automatic event detection algorithm and phase picking.

Nowadays there are various automatic techniques available for the detection and picking of seismic events (Küperkoch et al, 2011; Trnkocsy, 2012; Vaezi and van der Baan, 2015). In this study, the Short-Term Average / Long-Term Average (STA/LTA) method is used for event detection by detecting waveform anomalies in the form of changes in amplitude. Prior to this method, the data is required to be filtered to remove unwanted noise and thus provide better data to process and analyse. After an event has been detected, the Akaike Information Criterion

(AIC) picker (Maeda, 1985) is implemented to accurately pick the P-phase arrival, needed for precise event location. To optimize the accuracy of the automated picks, each pre-calculated pick is manually reviewed and if necessary, improved. Moreover, to make sure that no seismic event was missed, events reported by the ISC were compared to those automatically detected by SeisComP3. Manual picking was also implemented in the case when an event detected by the ISC was not automatically detected with SeisComP3.

2.1.1 Event detection filters

Recorded seismic traces are highly polluted by various types of noise arising from different kinds of sources. Such unwanted noise has a serious impact on the quality of the seismic data. Hence, one main purpose of seismic data processing is to improve as much as possible the signal-to-noise ratio (SNR). To preserve the signal of interest and enhance the SNR, strategies for seismic noise attenuation are needed. In this project, unwanted noise effects from the seismic data are removed using three different filtering stages prior to the STA/LTA detector algorithm.

SeisComP3 first filters out the offset by making use of a running mean high pass (RMHP) filter of 10 seconds. Basically, the running mean, for a given timespan is computed and subtracted from the single amplitude values (GFZ Potsdam, 2018). Then in order to reduce the spectral leakage, a one-sided cosine taper (ITAPER) with a window length of 30 seconds is applied. This means that before performing a Fourier transform, the seismic data is multiplied by a tapering function. A typical taper is a function of which the amplitude smoothly decays to zero towards the window edges, aiming at diminishing the effect of the discontinuity between the beginning and ending data values. Although spectral leakage cannot be fully suppressed, it can be significantly minimized by altering the shape of the taper function in a way to reduce strong discontinuities towards the window edges. Numerous tapering functions have been proposed (Piersol, 2006), in this case the one-sided cosine taper i.e. the default tapering function in SeisComP3 was implemented.

The cosine taper window $c(t)$ is given by (Pilz and Parolai, 2012):

$$c(t) = \begin{cases} \frac{1}{2}\left(1 - \cos\frac{\pi}{a}t\right) & for\ 0 \leq t \leq a \\ 1 & for\ a \leq t \leq 1 \end{cases} \tag{2.1}$$

with time t and taper ratio a. Such tapering reduces the spectral power leakage from a spectral peak to frequencies far away. Moreover, it coarsens the spectral resolution by a factor of $\frac{1}{(1-a)}$ (Pilz and Parolai, 2012).

In the last filtering stage, a Butterworth Infinite Impulse Response (IIR) bandpass filter is implemented to eliminate both high and low unwanted frequencies from the seismic data and emphasize only those of interest. In order to use a bandpass filter, the frequency range of the data must be specified such that unwanted low frequency noise (lower than f_L), containing microseismic noise, and high frequency noise (higher than f_H) generated for instance by anthropogenic activities, can be removed from the data leaving the wanted frequency interval to be processed. This is illustrated in figure 2.1.

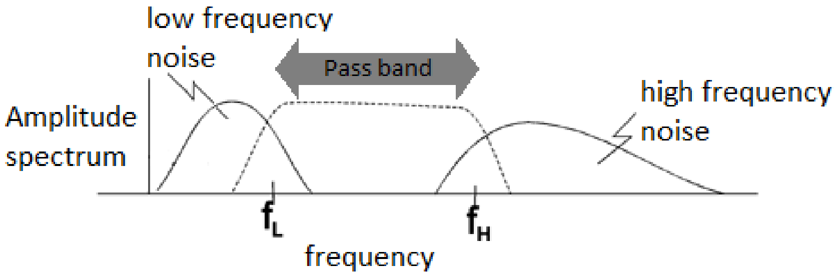

Figure 2.1. A bandpass filter with low corner frequency (f_L) and high corner frequency (f_H) shown in relation to the pass band (GeoSci Developers, 2017).

Generally, the pass band should allow frequencies associated with the maximum energy of expected seismic events. Nonetheless, it should also have a band pass that does not coincide with dominant frequency components of typical seismic noise at the site. Otherwise, the detection filter becomes inefficient (Trnkocsy, 2012).

The amplitude spectrum of the bandpass Butterworth filter is defined by

$$|G(f)|^2 = \frac{1}{1 + \left[\frac{|f| - f_b}{f_c}\right]^{2n}} \tag{2.2}$$

where f_b is the centre of the pass band, f_c is the pass band half width and the steepness of the filter is defined by the order n of the filter (University of Washington School of Oceanography, 2014).

2.1.2 STA/LTA detector algorithm

The STA/LTA is one of the most widely used detection algorithms. It works by processing seismic signals in which the average values of the absolute amplitude is continuously calculated in two consecutive moving time windows, i.e., the short-time average window (STA) and the long-time average window (LTA) (Trnkocsy, 2012).

The STA/LTA ratio is a measure similar to the signal-to-noise ratio (SNR) since the STA calculates the 'instant' amplitude of the seismic signal, while the LTA measures the average seismic noise amplitude (Trnkocsy, 2012). The average of the absolute amplitudes of a seismic trace $w(t)$ within both the STA and LTA windows is calculated by (Agius, 2007; Schweitzer et al, 2012)

$$STA(t) = \frac{1}{S} \cdot \sum_{j=0}^{S-1} |w(t-j)| \tag{2.3}$$

$$LTA(t) = \frac{1}{L} \cdot \sum_{j=0}^{L-1} |w(t-j)| \tag{2.4}$$

where $S = sampling\ rate \times STA\ length\ in\ seconds$

$L = sampling\ rate \times LTA\ length\ in\ seconds$

To detect the presence of P-phase arrivals and provide a rough estimation of the P-onset time, the STA/LTA detector algorithm in SeisComP3 requires four input parameters. These include the STA and LTA window length, a trigger threshold value and a detrigger threshold value which are further discussed in the following subsections. The explanation provided for these parameters is based on the information provided by Trnkocsy (2012).

2.1.2.1 STA and LTA window length

Window length plays an important role in the performance of the STA/LTA algorithm. The choice of the STA and LTA window lengths depends on the frequency content of the seismic waveform. Usually, the choice of the STA duration should be longer than a few periods of a typically expected seismic signal while the optimum LTA window should be longer than a few periods of the typically irregular seismic noise variations.

By adjusting the STA duration one can relatively prioritize to capture either distant or local events. The reason for this is that the shorter the STA duration is, the higher the detector sensitivity is to short period local events, but less the sensitivity is to long lasting and lower frequency distant earthquakes, and vice versa. It is also important to keep in mind that the smaller the STA window is, the more sensitive the detector is to spike-type man-made seismic noise, and vice versa (figure 2.2). This implies that the STA duration is also of great importance with regards to false detections. Thus, if false events are detected frequently at highly polluted spike-type noise sites, the STA duration must be changed so that it is much longer than these spikes. Unfortunately, this will also reduce the detector sensitivity to local short lasting events (Trnkocsy, 2012).

A longer LTA window is required to detect events with weak P-waves compared to S-waves. Longer LTA window duration also makes the STA/LTA detector more sensitive to detect P waves and increases the detector sensitivity to regional events in the 'P_n' wave, varying from about 200 to 1500 km epicentral distance. In contrast, as shown in figure 2.3, a short LTA can prevent false detections owing to regular changes of continuous man-made seismic noise. Such changes of man-made seismic noise are usually associated with night-to-day transition of human activity in urban areas (Earle and Shearer, 1994; Trnkocsy, 2012; Akram and Eaton, 2016).

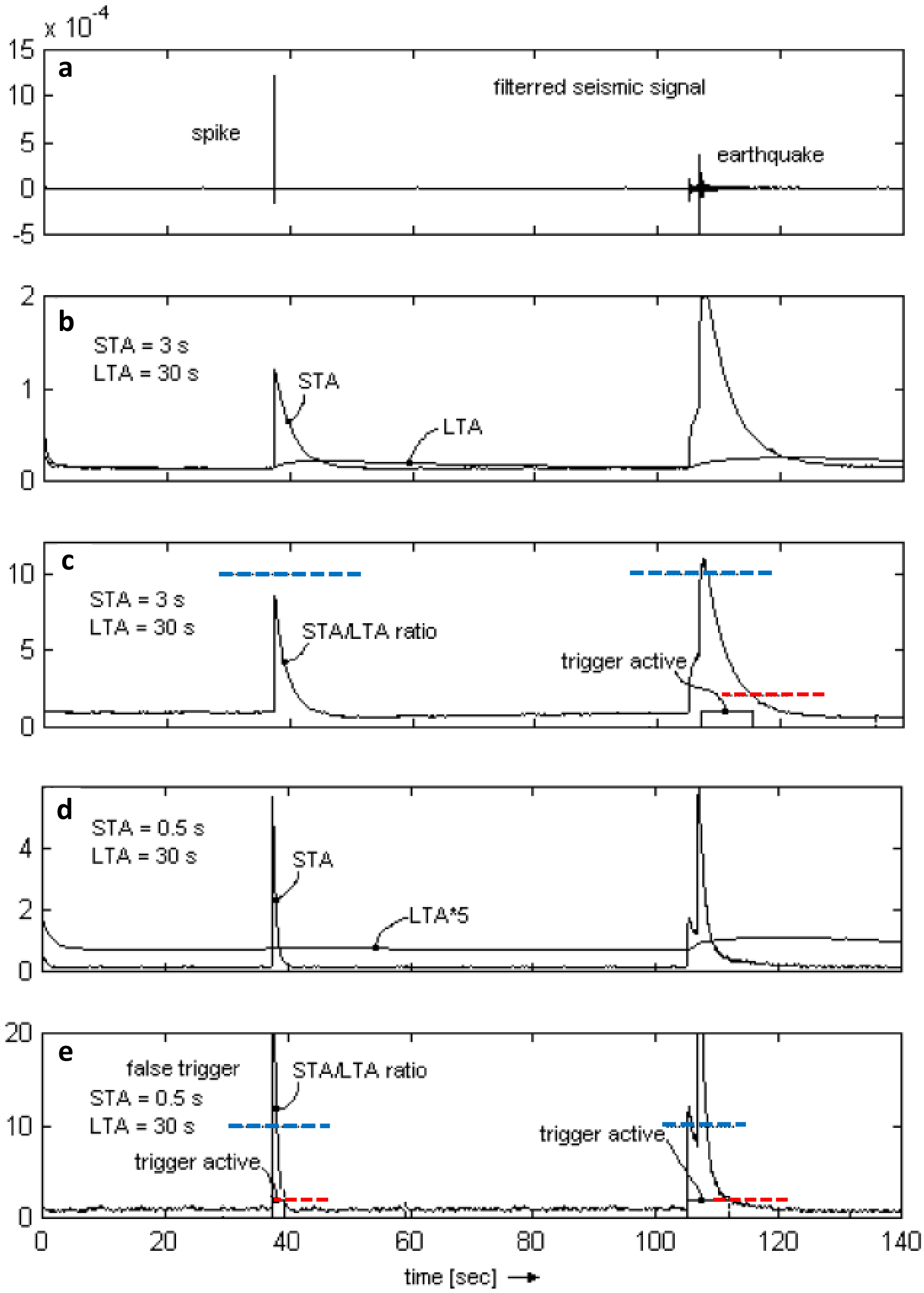

Figure 2.2. The effect of STA window duration on the detector sensitivity to short lasting local events and spike-type noise by Trnkocsy (2012). Graph (a) illustrates a filtered seismic signal with an instrumental spike on the left and a weak local earthquake on the right side of the plot. Graphs (b) and (c) demonstrate the STA, LTA and STA/LTA ratio, respectively, with a long STA window of 3 seconds. The STA/LTA trigger threshold is indicated by a blue dashed horizontal line and the detrigger threshold is indicated by a red dashed horizontal line in the STA/LTA plots. In this case, the large amplitude but short lasting spike did not trigger the system and hence, no false event was detected while the weak earthquake was hardly detected. Graphs (d) and (e) represent the same situation but with a shorter STA window of 0.5 seconds. The STA/LTA ratio for both the spike and earthquake exceeded the trigger threshold however, a false detection was generated due to the spike.

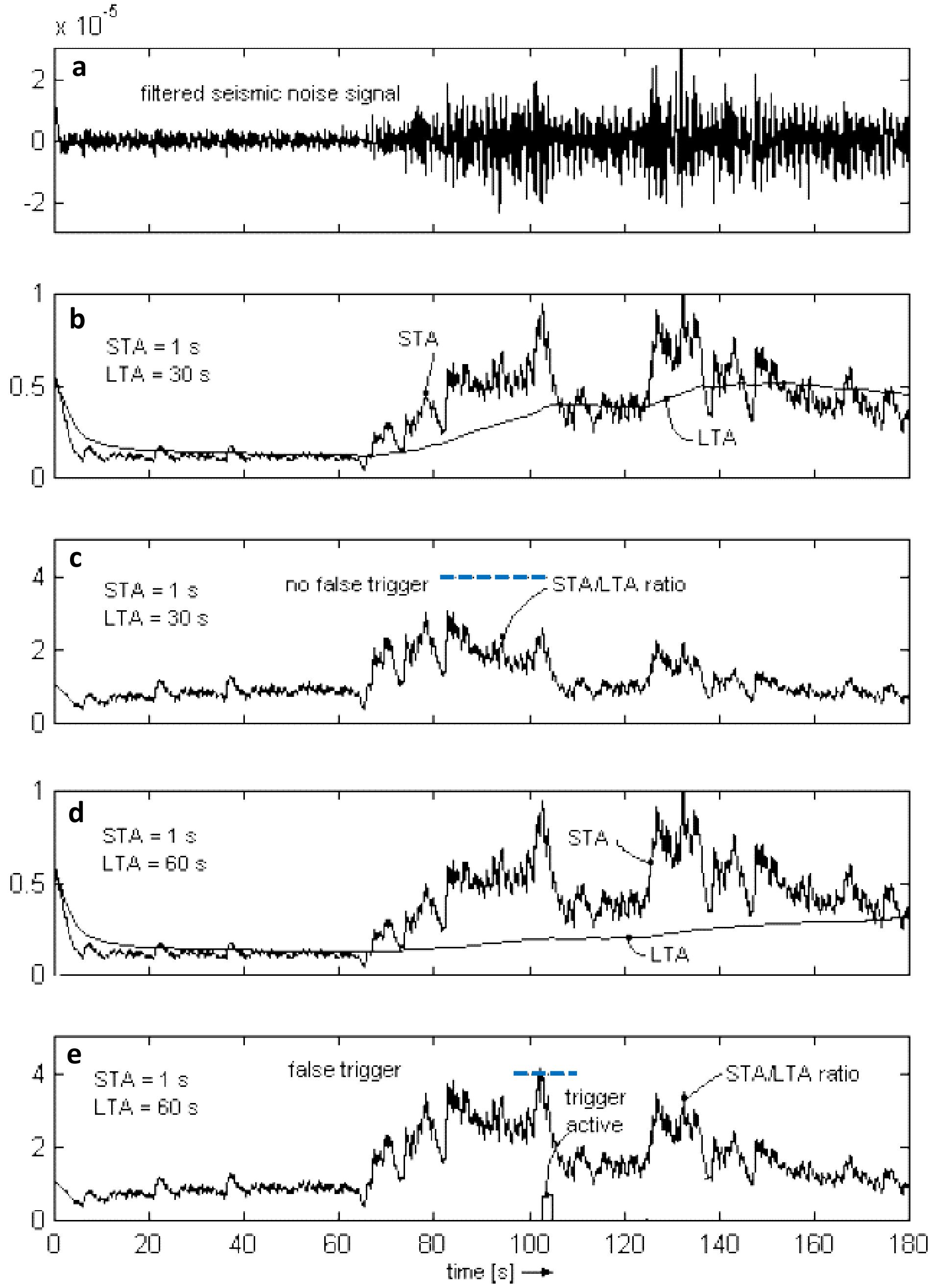

Figure 2.3. LTA window length response on false event detections from Trnkocsy (2012). Graph (a) shows a filtered seismic noise signal with an increase in seismic noise gradually occurring in the middle of the record. Graph (b) shows that with a short LTA window of 30 seconds, the LTA value is aware of the increased noise amplitude and thus, no false event is detected. This is shown in graph (c) where the STA/LTA ratio does not reach the STA/LTA trigger threshold (represented by the blue dashed horizontal line). Graphs (d) and (e) show the same situation but with a longer LTA of 60 seconds. The LTA value, in this case, changes gradually, resulting in a higher STA/LTA ratio as noise increases. Hence, generating a false event detection.

2.1.2.2 Triggering

Whenever a seismic signal is processed, the absolute amplitude of each data sample is calculated and used to evaluate the average of absolute amplitudes in both the STA and LTA windows. The ratio of both windows is then calculated and continuously compared to the selected STA/LTA trigger threshold value. When the ratio exceeds this pre-set threshold, an event is detected. Figure 2.4 shows an example of the detector variables during the STA/LTA algorithm.

The STA/LTA trigger threshold level basically controls which events will be detected and which will not. If a high value is set, less earthquakes will be detected, however, less false event detections will result. On the other hand, if a low STA/LTA trigger threshold is used, the higher the seismic station's sensitivity will be and the more events will be detected, although this may also lead to more frequent false detections. The ideal STA/LTA trigger threshold value is based on the seismic noise conditions in the area and on one's tolerance to false event detections. The setting of the optimum trigger threshold level is not only influenced by the amplitude but also by the type of seismic noise. Seismic noise with less irregular fluctuations enables a lower STA/LTA trigger threshold value while entirely irregular behaviour of seismic noise requires higher values (Trnkocsy, 2012).

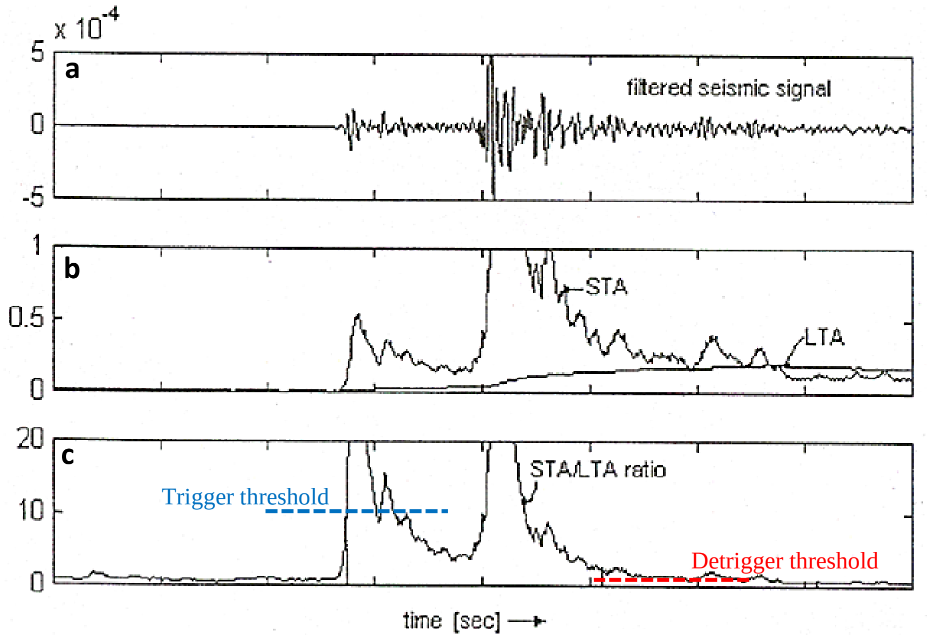

Figure 2.4. A typical local event with STA/LTA detector variables. Graph (a) shows an incoming continuous filtered seismic signal. Graph (b) shows an averaged absolute signal of the STA and LTA windows, respectively, as they move in time towards the right. Graph (c) shows the STA/LTA ratio with trigger threshold value set to 10 and detrigger threshold value set to 1 (Trnkocsy, 2012).

2.1.2.3 Detriggering

As the seismic signal gradually decays, the STA/LTA detector deactivates. This occurs when the current STA/LTA ratio falls to the value of the selected STA/LTA detrigger threshold level. As shown in figure 2.4, this detrigger threshold value should be lower (or rarely equal) than the STA/LTA trigger threshold value.

A low detrigger value is required to encompass as much of the coda waves as possible. However, a very low value may not allow the STA/LTA ratio to fall below the detrigger threshold value and thus, might miss to detect subsequent events. Moreover, a higher detrigger value should be set if one is not interested in the coda waves. Generally, the noisier the seismic site is, the higher the detrigger threshold value must be set. On the other hand, for seismically quiet areas, a typical initial value of the STA/LTA detrigger threshold level must be either set to 2 or 3.

2.1.3 AIC picker

Accurate detection and picking of the first P-wave arrival is crucial for hypocenter determination, event identification and source mechanism analysis. Traditionally, this work is done by an analyst who analyses the seismograms and picks out important phase arrivals. However, this task can take a lot of time, especially for large volumes of digital data (Zhang et al., 2003). Hence, nowadays it is extremely beneficial to use an automatic phase picker which automatically picks the onset times of seismic waves.

Much effort has been dedicated to design algorithms that automatically and precisely pick P-phase arrival times. Some of the proposed and widely used P-picking algorithms include; the Allen (1978) picker, in which the trace amplitude and the time derivative of the trace are used to generate a characteristic function (CF) that is compared to some threshold value, the Baer and Kradolfer (1987) (BK) picker which uses an envelope function (slightly modified from the Allen picker) and a dynamic threshold value, and higher order statistics in which statistical properties in a sliding window are calculated to generate a CF which is used to estimate the arrival times (e.g., Küperkoch et al., 2010). In addition to these time and frequency domain techniques, model oriented algorithms, like the one used in this study, based on the Akaike Information Criterion (AIC) became also quite common (Küperkoch et al., 2011). This criterion, which compares the quality of a set of statistical models and aims to select the best model, is given by (Akaike, 1971):

$$AIC = -2(maximum \log likelihood) + 2(number\ of\ parameters) \tag{2.5}$$

where the number of parameters is defined by the model order (Küperkoch et al., 2011). Initially, this function (equation (2.5)) was developed to determine the order of an autoregressive (AR) process, with the first term indicating the badness of the model fit and the second term the unreliability (Akaike, 1974). In seismic data, this criterion is used to distinguish the point of two adjacent time series with distinct underlying statistics (St-Onge, 2011).

Two robust AIC based approaches, referred to as AIC pickers, have been proposed for determining the P-onset time of a seismic signal (Zhang et al., 2003; St-Onge, 2011). One uses an AR process of a fixed order (Sleeman and van Eck, 1999) while the other computes the AIC function directly from a seismic waveform, without using an AR process (Maeda, 1985). Since the characteristics of a seismogram, such as the variance and the spectrum suddenly change with the occurrence of a seismic event (figure 2.5), this AIC picker assumes that the intervals before and after the first P -wave arrival time, are two different stationary time series (Küperkoch et al., 2011). In these AIC based approaches, the AIC function is computed for each sample of a shortened time series and the onset point, is determined by the global minimum AIC value (Ahmed et al., 2007).

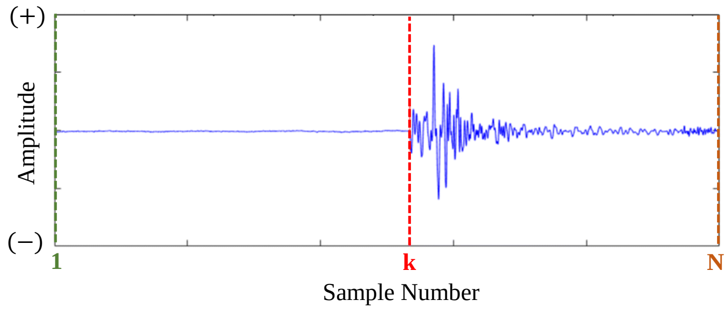

Figure 2.5. An example of a seismic trace indicating the separation point k of two statistically different parts i.e., the pre-onset segment from sample 1 till k and the post-onset segment from sample $k+1$ till N (St-Onge, 2011).

The portion before phase arrival, consisting of seismic noise and the portion afterward, consisting of the seismic signal (figure 2.5), are two segments with different statistical properties. At first, a small k sample value is multiplied by the log of the variance of the seismic data from samples 1 to k. The variance measures how far a set of data is spread out, defined as (Kurz et al., 2005):

$$var = \frac{1}{n-1}\sum_{i=1}^{n}(x(i)-\bar{x})^2 \qquad (2.6)$$

where n denotes the sample size,

$x(i)$ is sample i of the time series x and

$\bar{x}$ is the mean of the whole time series x.

Hence, the variance of a low amplitude seismic data gives a small value since the data points are located close to each other. This variance will get even smaller as k increases. However, at the P-wave onset, the samples from $k+1$ till N will have a larger variance than before. Thus, the AIC value will start to increase, indicating a global minimum at the P-wave onset. As a result, the AIC array plot will have a slanted v-shape form, as shown in figure 2.6(a) (St-Onge, 2011).

In this study, the AIC picker applied is that which is directly calculated from the seismic data, as proposed by Maeda (1985). In fact, when a seismic event is detected by exceeding the STA/LTA trigger threshold, a smaller time window containing the P-onset is cut out for more precise picking by this AIC picker. In this case, for the curtate time series x of length N samples, the AIC function at sample k is defined by

$$AIC(k) = k \cdot \log\{var(x[1,k])\} + (N-k-1) \cdot \log\{var(x[k+1,N])\} \tag{2.7}$$

where k ranges through all samples of x,
$var(x[1,k])$ is the variance of the time series $x(1), x(2), \ldots, x(k)$ and
$var(x[k+1,N])$ is the variance of the time series $x(k+1), x(k+2), \ldots, x(N)$.

The implemented AIC picker in SeisComP3 uses equation (2.7) to calculate the AIC array values, as shown in figure 2.6 (lower traces). It compares these values to search for a global minimum which determines the optimal separation point of the two adjacent time series. This point is interpreted as the P-wave onset (Zhang et al., 2003).

In order for the AIC picker to pick the P-wave arrival correctly, the selection of a proper time window that includes only the seismogram segment of interest is important. As shown in figure 2.6(a), when the P-wave arrival is clearly visible in the seismogram, the AIC values would indicate a very clear global minimum. Hence, the AIC picker is likely to be very accurate. If the seismogram has a relatively low SNR (figure 2.6(b)), there might be multiple local minima in the AIC values function however, the P-wave arrival is still distinguished by the global minimum. When more seismic noise than signal is present in the seismogram (figure 2.6(c)), indicating a very low SNR seismic signal, the global minimum is not clearly evident and thus, the AIC picker may provide large errors. Moreover, if several seismic phases are available in a time window (figure 2.6(d)), the AIC picker will indicate its global minimum at the strongest phase which may not represent the first P-wave arrival. On the contrary, the AIC picker will almost always indicate a global minimum in a time window irrespective to whether a true phase arrival is present or not (figure 2.6(e)). Thus, it is due to these reasons that we need to select a suitable time window that will enable the AIC picker to function properly (Zhang et al., 2003; Ahmed et al., 2007).

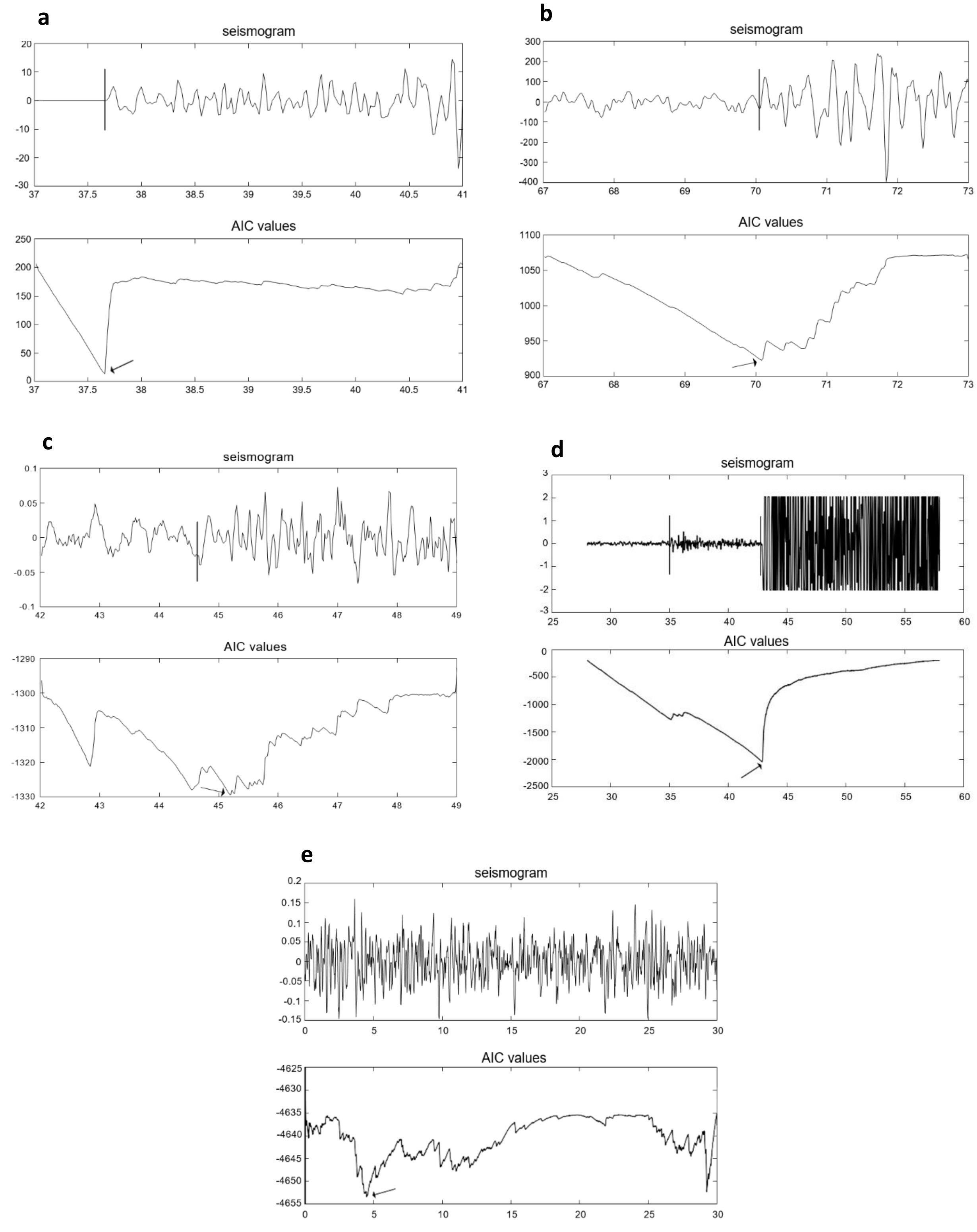

Figure 2.6. Seismograms (upper traces) and their corresponding AIC values (lower traces) by Zhang et al. (2003) showing (a) a very distinct P-wave onset, (b) a rather clear P-wave arrival with relatively lower SNR, (c) a very low SNR seismogram, (d) multiple phases available in a time window and (e) seismic noise data in which the AIC global minimum does not represent any phase arrival. The black vertical lines in seismograms (a) till (d) indicate the P-wave arrival and the arrows represented in each AIC array plot indicate the global minimum.

2.1.4 Manual P −phase picking

Despite significant advancement in automated P-onset detection and determination, picking results are still inferior to those attained manually. Thus, a proper combination of automatic and manual data processing should be ensured to produce high quality P-phase picks (Bormann et al., 2014).

Manual review of all automatically detected events by SeisComP3 is accessible through an interactive GUI (Graphical User Interface), where a number of tools are available to revise and modify, if necessary, the accuracy of the automated first P-wave onset. This is done by analysing filtered seismic signals only in the vertical component since the arrival of a P-wave is observed more clearly in this component. By zooming in a portion of the time series containing the P-onset, automatic P picks are carefully analysed and if not accurate, manual re-picking is implemented by marking the P-onset at the point where anomalies in the form of changes in amplitude are first observed. P-wave arrival times detected automatically and/or manually for a particular event are then further investigated by reviewing their trend in a travel time against distance plot (referred to as well as a travel time curve). The resulting P-wave arrival times should smoothly increase with distance. Hence, a similar trend to the P-wave curve in figure 2.7 should be attained. Any outliers in this plot are analysed again and removed if there is no clear P-onset.

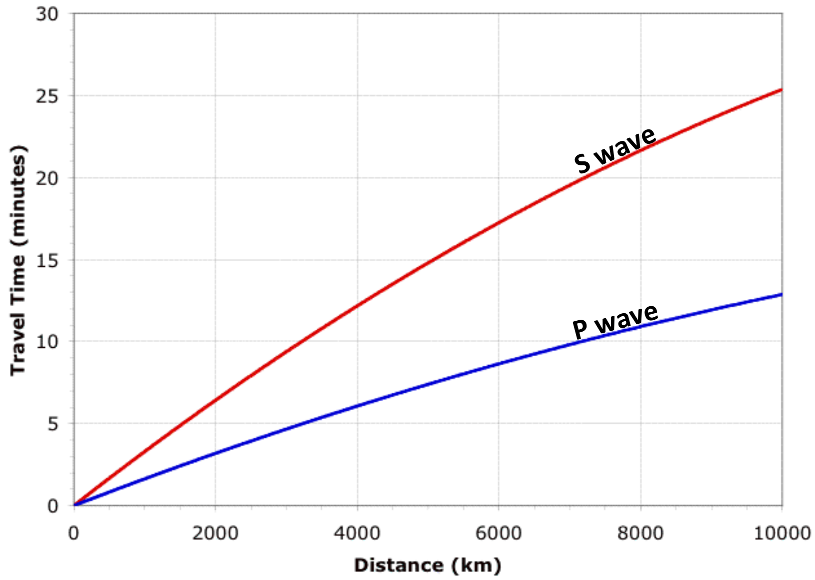

Figure 2.7. An example of a travel time curve showing the expected first P- and S-waves arrival times at a range of distances from the epicentre of a seismic event (Columbia University, 2017).

In the absence of an automatic detected event, manual analysis is implement in SeisComP3 by creating a preliminary origin. In this case, seismic signals recorded by multiple stations are examined to identify any missed seismic event. If the P-onset is clear, manual P-phase picking is applied. To ensure that no seismic event was missed, it was made sure that all automatically detected events by SeisComP3 were compared to the unreviewed events published on the ISC On-line Bulletin (2016). Any events that were detected by the ISC but not with SeisComP3 were used as input data for the preliminary origins that are manually analysed.

2.2 Event location

Once the first P-wave arrivals are picked, the next step is to identify combinations of picks that correspond to a common seismic event and determine the location of that seismic event. This is done by first considering the classic inverse problem discussed below, based on Shearer (2009) earthquake location explanation.

An earthquake is defined by its origin time (T) i.e., the initiation time of the earthquake rupture and the position (x, y, z), known as the hypocenter. The point (x, y) directly above the hypocenter, on the Earth's surface, is defined as the epicenter. In location methods, earthquakes are generally treated as point sources with the hypocenter considered as the starting point of the rupture process, usually specified in longitude (x), latitude (y), and depth below the surface (z). Since the P-wave propagation velocity is larger than the rupture velocity, the hypocenter can be resolved from the first arrival times, irrespective of the size and duration of the event.

Consider n seismic stations at locations (x_i, y_i, z_i) which detect an event at arrival times t_i^{obs} $(i = 1,2, \dots, n)$. The hypocenter location and origin time describe four unknown earthquake parameters, defined by the model vector,

$$\boldsymbol{m} = (m_1, m_2, m_3, m_4) = (x, y, z, T) \tag{2.8}$$

If we now assume some velocity model, then for every estimated $\boldsymbol{m}$ the predicted arrival time at each station can be calculated

$$\boldsymbol{t^{pred}} = \boldsymbol{F}(\boldsymbol{m}) \tag{2.9}$$

In equation (2.9) $\boldsymbol{F}$ is a function of both the velocity model considered and the individual station locations, particularly it is a non-linear function of the model parameters (except for the origin time T). Note that this is a forward problem that gives the predicted arrival time at a station from $\boldsymbol{m}$. Since we have n observations, there will be n arrival time equations in equation (2.9). Hence, the system of equations is overdetermined as there are usually many more equations than unknowns (i.e., $n > 4$).

The inverse problem we are trying to solve is that, given the observed arrival times, we wish to determine the $\boldsymbol{m}$ that, in a certain sense, gives the smallest arrival time residual at each station. The residual r_i at the i^{th} station is defined as the difference between the observed and predicted travel times which is the same as the difference between the observed and predicted arrival times:

$$r_i = t_i^{obs} - t_i^{pred} \tag{2.10}$$

$$= t_i^{obs} - F_i(\boldsymbol{m}) \tag{2.11}$$

To find the optimal $\boldsymbol{m}$, a grid search approach in combination with an iterative least-squares inversion algorithm is applied to identify the best fitting event location and origin time. In the following sub-sections, the grid search approach and the iterative least-squares inversion algorithm will be further discussed, along with event location error assessment.

2.2.1 Grid Search

By using a grid consisting of a set of discrete points that sample the region of interest adequately, a grid search over all possible locations and origin times is performed. Each of the grid points, in this approach is considered as a theoretical hypocenter for all incoming P picks (GFZ Potsdam, 2018).

For each seismic event, the observed (or measured) arrival times t_i^{obs} are compared to those predicted arrival times t_i^{pred} at each grid point. Ultimately, the optimal estimate for $\boldsymbol{m}$ would then be indicated by the grid point with the best agreement between these two arrival times. This implies that some measure of 'best agreement' is required, especially when several P-wave arrival times are observed. A frequent used approach is to seek for a $\boldsymbol{m}$ with least squares (known also as the L2 norm) that minimizes the sum of the squared residuals ϵ observed at n seismic stations (Shearer, 2009):

$$\epsilon = \sum_{i=1}^{n} \left[t_i^{obs} - t_i^{pred}\ \right]^2 \tag{2.12}$$

The RMS (root mean square) residual, defined as $\sqrt{\epsilon/n}$, is usually used as a guide to location accuracy. If the residuals are similar in value, the RMS residual provides an estimated average residual. It should be noted that the RMS residual provides only an indication of the fit of the data (Havskov et al., 2011). Furthermore, the variance of the data, in other words, the average squared residual ϵ/n , describes the spread in the residuals. In statistics, the variance is formally defined as ϵ/n_{df}, where n_{df} is the number of degrees of freedom i.e., the difference between the number of observations n and the number of free parameters in the fit (in our case, $n_{df} = n - 4$ since $\boldsymbol{m}$ consists of 4 parameters). Typically, n is greater than the number of fitting parameters, and therefore n and n_{df} are considered roughly to be equal. Additionally, this implies that residual RMS^2 is roughly equal to the variance (Shearer, 2009).

The least squares approach is the most frequently used measure of misfit due to the simple forms of equations attained in the minimization problems. It will work properly if the misfit between t^{obs} and t^{pre} is generated by uncorrelated, random Gaussian noise. However, this is often not the case as the errors are non-Gaussian. As a result, the least squares approach will be more sensitive to the outliers i.e., individual large residuals of the data. For instance, a residual of 3 will contribute 9 times more to the misfit ϵ, than a residual of 1. An alternative strategy that can partially solve this problem is to use the sum of the absolute residuals

$$\epsilon = \sum_{i=1}^{n} \left|t_i^{obs} - t_i^{pred}\right| \tag{2.13}$$

This measure of misfit, known as the L1 norm, is much more robust to outliers than the L2 norm.

Once a measure of misfit has been defined (e.g., the RMS residual) and computed for each grid point, the optimal $\boldsymbol{m}$ is identified by the point with the smallest misfit (Shearer, 2009; Havskov et al., 2011). Note that a grid search for the origin time is not required. In fact, the best fitting origin time at each grid point can be attained by simply calculating the median of the residuals, in the case of the L1 norm or the average of the residuals, in the case of the L2 norm (Shearer 1997; Richards-Dinger and Shearer, 2000).

Ideally, the optimal $\boldsymbol{m}$ for well-behaved data is clearly identified by the point with the smallest misfit however, in reality, the arrival times are contaminated with errors. As a result, there might be multiple grid points, even far away from each other, with similar misfit (Havskov et al., 2011). Hence, the iterative least-squares inversion algorithm is eventually implemented to test the location found by the grid search and examine if the set of picks indeed form a consistent hypocenter.

2.2.2 Iterative least-squares inversion algorithm

The following explanation of the iterative least-squares location algorithm is based on the text by Stein and Wysession (2003) and Shearer (2009). The algorithm starts off by considering a trial model $\boldsymbol{m}_0$, which is an estimated guess which we hope is close to the best location. In our case, the solutions determined from the grid search approach will represent this trial model. The new location $\boldsymbol{m}$ located a small distance away from $\boldsymbol{m}_0$ is given by

$$\boldsymbol{m} = \boldsymbol{m}_0 + \Delta\boldsymbol{m} \tag{2.14}$$

where $\Delta\boldsymbol{m}$ is considered to indicate small perturbations to the target solution $\boldsymbol{m}$.

In order to linearize the problem (equation (2.11)), the predicted times at $\boldsymbol{m}$ are approximated by using the first term (the linear term) in the Taylor series expansion:

$$t_i^{pred}(\boldsymbol{m}) = t_i^{pred}(\boldsymbol{m}_0) + \frac{\partial t_i^{pred}}{\partial x}\Delta x + \frac{\partial t_i^{pred}}{\partial y}\Delta y + \frac{\partial t_i^{pred}}{\partial z}\Delta z + \Delta T$$

$$= t_i^{pred}(\boldsymbol{m}_0) + \frac{\partial t_i^{pred}}{\partial m_j}\Delta m_j \tag{2.15}$$

The index j in equation (2.15) ranges from 1 to 4 and corresponds to the earthquake parameters defined in equation (2.8).

Hence, the residuals at the new location $\boldsymbol{m}$ can now be written as

$$r_i(\boldsymbol{m}) = t_i^{obs} - t_i^{pred}(\boldsymbol{m})$$

$$= t_i^{obs} - t_i^{pred}(\boldsymbol{m}_0) + \frac{\partial t_i^{pred}}{\partial m_j}\Delta m_j$$

$$= r_i(\boldsymbol{m}_0) + \frac{\partial t_i^{pred}}{\partial m_j}\Delta m_j \tag{2.16}$$

To minimize these residuals in such a way that the predicted data are closer to those observed, we seek to find $\Delta\boldsymbol{m}$ such that

$$r_i(\boldsymbol{m}_0) = \frac{\partial t_i^{pred}}{\partial m_j} \Delta m_j \tag{2.17}$$

In vector-matrix form this can be written as

$$\boldsymbol{r}(\boldsymbol{m}_0) = \boldsymbol{G}\,\Delta\boldsymbol{m} \tag{2.18}$$

where $\boldsymbol{r}$ is the residual vector computed from a trial model $\boldsymbol{m}_0$ and $\boldsymbol{G}$ is an $n \times 4$ matrix of partial derivatives i.e.,

$$G_{ij} = \frac{\partial t_i^{pred}}{\partial m_j} \tag{2.19}$$

with $i = 1,2, \dots, n$ and $j = 1, \dots, 4$.

Equation (2.18) represents a system of linear equations with 4 unknowns (corrections to the hypocenter and origin time). Nonetheless, there are $\boldsymbol{n}$ equations of this type corresponding to each observed arrival time. Therefore, since the minimum number of automatically detected *P* picks needed to declare an event in SeisComP3 is 6 (GFZ Potsdam, 2018), equation (2.18) will consists of more equations than unknowns. In order to solve such overdetermined problem, one solution for the perturbation vector $\Delta\boldsymbol{m}$ is acquired by using the standard least squares minimization technique (Shearer, 2009). To do this, we regard the elements of $\boldsymbol{r}$ and $\boldsymbol{G}$ as having errors described by their standard deviations σ_i. Thus, the least squares solution is given by the model that minimizes the misfit,

$$\chi^2 = \sum_{i=1}^{n} \frac{1}{{\sigma_i}^2} \left[r_i(\boldsymbol{m}_0) - \sum_{j=1}^{4} G_{ij}\,\Delta m_j \right]^2 \tag{2.20}$$

referred to as the prediction error. For the misfit to be small as possible, the partial derivative of χ^2 with respect to the change in the model parameters Δm_k must equal to zero.

$$\therefore \qquad \frac{\partial \chi^2}{\partial \Delta m_k} = 0 = 2 \sum_{i=1}^{n} \frac{1}{{\sigma_i}^2} \left[r_i(\boldsymbol{m}_0) - \sum_{j=1}^{4} G_{ij}\,\Delta m_j \right] G_{ik} \tag{2.21}$$

Rearranging, equation (2.21) yields

$$\sum_{i=1}^{n} \frac{1}{{\sigma_i}^2}\, r_i(\boldsymbol{m}_0)\, G_{ik} = \sum_{i=1}^{n} \frac{1}{{\sigma_i}^2} \left[\sum_{j=1}^{4} G_{ij}\,\Delta m_j \right] G_{ik} \tag{2.22}$$

If the variance of the data are equivalent ($\sigma_i{}^2 = \sigma^2$), then the variance term in equation (2.22) can cancel out, and

$$\sum_{i=1}^{n} r_i(\boldsymbol{m}_0)\, G_{ik} = \sum_{i=1}^{n} \left[\sum_{j=1}^{4} G_{ij}\, \Delta m_j \right] G_{ik} \tag{2.23}$$

In matrix notation this can be written as

$$\boldsymbol{G}^T \boldsymbol{r}(\boldsymbol{m}_0) = \boldsymbol{G}^T \boldsymbol{G}\, \Delta\boldsymbol{m} \tag{2.24}$$

$\boldsymbol{G}^T \boldsymbol{G}$ is a square matrix and thus, its inverse exists. Hence, a solution for the perturbation vector $\Delta\boldsymbol{m}$ is obtained by taking the inverse of $\boldsymbol{G}^T \boldsymbol{G}$ on both sides of equation (2.24)

$$(\boldsymbol{G}^T \boldsymbol{G})^{-1} \boldsymbol{G}^T \boldsymbol{r}(\boldsymbol{m}_0) = (\boldsymbol{G}^T \boldsymbol{G})^{-1} \boldsymbol{G}^T \boldsymbol{G}\, \Delta\boldsymbol{m}$$

$$(\boldsymbol{G}^T \boldsymbol{G})^{-1} \boldsymbol{G}^T \boldsymbol{r}(\boldsymbol{m}_0) = \boldsymbol{I}\, \Delta\boldsymbol{m} \qquad \text{where } \boldsymbol{I} = \text{Identity matrix}$$

$$\therefore \qquad \Delta\boldsymbol{m} = (\boldsymbol{G}^T \boldsymbol{G})^{-1} \boldsymbol{G}^T \boldsymbol{r}(\boldsymbol{m}_0) \tag{2.25}$$

Next, we replace $\boldsymbol{m}_0$ by the new trial model $\boldsymbol{m}_0 + \Delta\boldsymbol{m}$ and repeat the process until the misfit is sufficiently small. Generally, this iterative process converges quite rapidly as long as the initial hypocentral guess is not far away from the actual solution (Stein and Wysession, 2003).

2.2.3 Location errors

Since seismic events are located using arrival times possibly contaminated with measurement errors and travel times that are calculated on the basis of the wrong assumption that the true velocity model is used, the hypocentral solutions will have errors (Havskov et al., 2011). These errors result in a relative location scatter around the actual location of the earthquake (Husen and Hardebeck, 2010). To get an indication of the probable uncertainties in our solution, the behaviour of the misfit function in the area close to the smallest misfit can be determined. In a two-dimensional case, this can be done for example, by contouring the RMS residual (i.e., the misfit) as a function of x and y in the vicinity of its minimum. If the RMS grows quickly when moving away from the minimum, it is made clear that a better solution has been attained than when the RMS grows very slowly away from its minimum (Shearer, 2009). Similarly, it would also be possible to create three-dimensional contours in order to get an indication of the 3D uncertainty (Havskov et al., 2011). However, this approach provides only a qualitative assessment of the uncertainties in our model parameters, it does not quantify this measure. In the seismic event location problem these uncertainties can be evaluated from a statistical point of view in order to determine the error ellipse, i.e., the way in which hypocenter errors are usually represented (Husen and Hardebeck, 2010). One can refer to the method described by Bratt and Bache (1988) for a detailed statistical understanding of how the error ellipse is computed.

In error analysis, the crucial variable is the variance σ^2 of the arrival times (Havskov et al., 2011). Depending on whether this data variance is known or not, two types of statistics, used to calculate the size of the confidence region, exist (Husen and Hardebeck, 2010). These include:

- F statistics used when the variance is unknown (e.g., Flinn, 1965; Jordan and Sverdrup, 1981)
- χ^2 statistic used when the variance is known (e.g., Evernden, 1969)

Basically, these error ellipse procedures use the arrival time variance to determine the corresponding misfit value. In the case where the data variance is unknown, an estimate s^2, derived from the residuals of the best fitting hypocenter $r_i(\boldsymbol{m}_{best})$ and the number of degrees of freedom $n_{df} = n - M$, is used (Shearer, 2009; Havskov et al.,2011):

$$s^2 = \frac{1}{n_{df}} \sum_{i=1}^{n} \left[t_i^{obs} - t_i^{pred}(\boldsymbol{m}_{best}) \right]^2 \tag{2.26}$$

Based on the work of Flinn (1965), the joint confidence region for the solution $\boldsymbol{m}_{best}$ is bounded by the p percent confidence ellipsoid, determined from

$$(\boldsymbol{m} - \boldsymbol{m}_{best})^T\, \boldsymbol{S}^{-1} (\boldsymbol{m} - \boldsymbol{m}_{best}) = {\kappa_p}^2 \tag{2.27}$$

where the parameter covariance matrix $\boldsymbol{S}$ is defined by

$$\boldsymbol{S} = s^2(\boldsymbol{G}^{\boldsymbol{T}}\boldsymbol{G})^{-1} \tag{2.28}$$

The confidence coefficient ${\kappa_p}^2$ is given by

$${\kappa_p}^2 = Ms^2F_p(M, n - M) \tag{2.29}$$

where $F_p(M, n - M)$ represents the F statistics at the p percent confidence level with M and $n - M$ degrees of freedom (Bratt and Bache, 1988).

Seismic events detected from outside a seismic network tend to have considerably large location uncertainties. This is mainly due to a poor station distribution. Moreover, since these events are recorded from only one side of the network, large tradeoffs exist between the location in the direction towards or away from the network and the origin time (Husen and Hardebeck, 2010). In our case, this should not be much of a problem as we seek to detect events in Botswana by using a good station coverage within most of the country. However, events recorded out to greater distances are likely to show higher location uncertainties.

Another issue in the event location problem is the well-known tradeoff between origin time and event depth. This usually results when there is a large distance between the stations location and the event recorded (figure 2.8). Consequently, changes in event depth may be offset by a shift in the event origin time (Shearer, 2009).

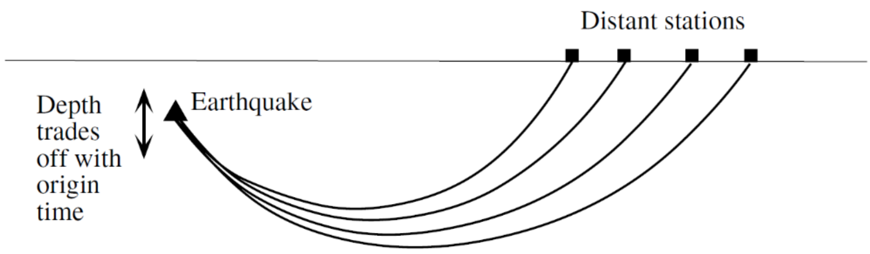

Figure 2.8. Tradeoff between event depth and origin time due to event recorded by only distant stations (Shearer, 2009).

3. Data Processing

Once the NARS-Botswana data was accumulated from the 21 broadband seismic stations in Botswana and stored into the system, it was possible to process and analyse it for the occurrence of possible seismic events between January 2014 and March 2018. To detect seismic events and determine their hypocentre location, the software package SeisComP3 (SC3) (version 2017.334) was used.

Before the processing of data, station metadata, including station and instrument response information, obtained from dataless SEED files were configured in SC3 station bindings (note that a binding in SC3 maintains the configuration of how a station is utilized in a module (GFZ Potsdam, 2018)). On the other hand, the NARS-Botswana data, containing only waveform data, were in MiniSEED files. However, since these MiniSEED files are not organised as separate files per day, per station component, it was necessary to use the 'dataselect' programme (https://github.com/iris-edu/dataselect) to sort the NARS-Botswana data in SeisComP Data Structure (SDS). In order to create and extract multiplexed sorted MiniSEED files from SDS archives, one has to run the archive tool, *scart*, available as one of the utilities in SC3. The following is an example used in Linux command line:

```
seiscomp exec scart -dsvE -t '<start-time>~<end-time>' <path to SDS archive> > dayfile.mseed
```

This command merges MiniSEED day files from each and every station, located in a local SDS archive into one MiniSEED volume per day, called *dayfile.mseed*. Thus, it organises the data to be finally used for processing by SC3.

SC3 has a modular design approach in which every module is in charge of a discrete task. Table 3.1 shows the modules used in this study with a description of their corresponding task. These modules communicate with each other through a Transmission Control Protocol/Internet Protocol (TCP/IP) messaging system based on the open source toolkit *Spread* (http://www.spread.org/). The main component of the messaging system, referred to as the mediator, is called *scmaster*. This is the only module in SC3 providing writing access to the database by making sure that all the information communicated between modules is written in its database (Hanka et al., 2010). By default, SC3 uses the MySQL database, in which its database schema is based on QuakeML (an XML-based data exchange standard for the representation of seismological parameters) (Schorlemmer et al., 2011).

For waveform data access, SC3 utilizes both the *seedlink* and *arclink* protocols. *Seedlink* is used for (real-time) data acquisition and serves also as a client-server software. *Arclink*, on the other hand, complements *SeedLink* by supplying a larger store of data. The *arclink* protocol provides access to archived waveform data via the module *slarchive* in MiniSEED format (Hanka et al., 2010). An automated switching between the *seedlink* and *arclink* protocols in SC3 is used when processing data in offline mode (Olivieri and Clinton, 2012).

SC3 is a software package designed for fast interactive analysis (Hanka et al., 2010). Apart from automatic earthquake detection and localisation, SC3 provides magnitude and amplitude estimations, and offers the possibility for manual picking to optimize results of pre-calculated picks and to assist in creating new origins for any undetected events. Figure 3.1 shows a flowchart of the main steps carried out within the processing of the NARS-Botswana data.

Table 3.1. List of SC3 modules used in this study for the detection and localisation of an event from Weber et al. (2017).

	Module Name	Task Description
Acquisition	*seedlink*	(Real-time) data acquisition and distribution
	arclink	Retrieval of archived waveform data and distribution
	slarchive	Data archiving in SDS
Processing	*scmaster*	TCP/IP messaging server
	scautopick	Automatic *P* detector/picker
	scautoloc	Automatic locator
	scamp	Amplitude calculation
	scmag	Magnitude calculation
	scevent	Event associator
Analysis	*scolv*	Origin Locator View: Full manual event revision and data analysis

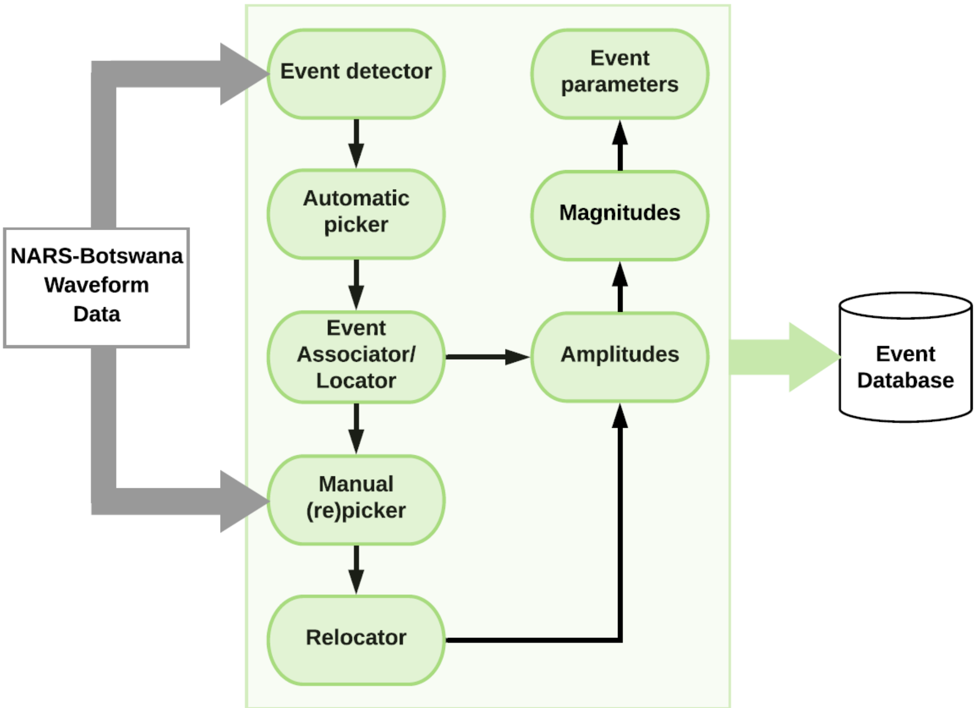

Figure 3.1. SC3 data processing flowchart.

This chapter will discuss the multiple stages executed with SC3 for the detection and location of seismic events in Botswana, along with some tested examples used to establish the optimum parameters configuration. Some of the text in the following sections, discussing the modules in SC3, is based on the current SeisComP3 documentation (GFZ Potsdam, 2018).

3.1 Automatic event detection

The *scautopick* module is used to detect automatically the arrival of P-waves by searching for waveform anomalies in the form of changes in amplitude. It starts by first reading all the parameters set in the configured bindings of each station. Later, each incoming record is filtered by applying a running mean high pass (RMHP) filter of 10 seconds, a one-sided cosine taper (ITAPER) of 30 seconds and a fourth order Butterworth bandpass filter with corner frequencies specified in section 3.1.1. After filtering the data, a two-step procedure is applied to automatically pick the P-phase arrival time. First a rough estimation of the P-onset time is obtained through the short- and long- term average (STA/LTA) ratio detector. This detector computes the STA/LTA ratio in each trace and checks if this ratio exceeds the trigger threshold value set. Once this threshold is reached, an event is identified and the AIC picker is launched on an interval of the filtered data, relative to the initial detection made by the STA/LTA detector. This picker seeks to provide accurate P-onset time estimations which are eventually required for a precise event location.

As describing by Shearer (2009) P-waves are mostly visible on the vertical component of a seismogram, while little P energy is recorded on the horizontal components. Thus, the NARS-Botswana data were processed using the BHZ (broadband, high gain, vertical component) channel.

In this study, *scautopick* is run in offline mode on the vertical component of the multiplexed sorted MiniSEED volume data that were created per day, by the archive tool, *scart*. For example, the following call:

```
seiscomp exec scautopick --playback -I dayfile.mseed
```

will process all the data in *dayfile.mseed* for which bindings exits and send the output to the messaging system. Eventually, when all of the data records are fully processed *scautopick* will automatically stop running.

The following sub-sections present some examples that illustrate how the optimum parameters were obtained for:

- the corner frequencies of the fourth order Butterworth bandpass filter,
- the STA/LTA detector and
- the AIC picker

which are required by the module *scautopick* for the automatic detection of P-wave arrival times.

3.1.1 Butterworth bandpass filtering

To select the appropriate frequency range for Butterworth bandpass filtering, one has to first pay particular attention to the Nyquist frequency, which is half the sampling frequency of a discrete signal. The Nyquist frequency is the maximum frequency beyond which aliasing will occur. Since the data used in this study is sampled at a sampling frequency of 20 Hz, this results in a Nyquist frequency of 10 Hz. Moreover, low frequency noise, comprising of microseismic noise, and high frequency noise generated mainly by wind and cultural noise, had to be filtered out. According to Cessaro (1994), microseismic noise is identified by long period waves with dominant periods ranging from 2 to 40 seconds. By analysing some of the NARS-Botswana data, it was observed that the dominant frequency was typically 5 seconds. Hence, only frequencies greater than 0.2 Hz were considered.

To determine the optimal filter parameters (corner frequencies) of a fourth order Butterworth bandpass filter, the seismic events recorded on February 23rd, 2016 and April 27th, 2015 by stations NE219 and NE221, respectively, were tested and studied (figures 3.2 and 3.3). Different corner frequencies were applied to observe how they affected the quality of the signal. Eventually, the optimal filter was identified when the filtered signal provided a clear P-phase arrival with the least unwanted noise. In each case, shown in both examples represented in figures 3.2 and 3.3, the high corner frequency (f_H) was kept fixed whereas the low corner frequency (f_L) was changed to 0.3 Hz, 0.5 Hz and 0.7 Hz.

From the filtered time signals shown in figure 3.2, with particular reference to cases 3 and 4, it can be observed that in each of these cases the higher the f_L is, the clearer is the P-phase arrival time. The 0.7 – 2.0 Hz bandpass filter was observed to be the optimum filter from all due to the clear P-phase arrival and the removal of unwanted noise from the signal. Similar results can be observed in figure 3.3, where the 0.7 – 2.0 Hz bandpass filter also is the optimal filter. Consequently, a fourth order Butterworth bandpass filter with corner frequencies of 0.7 and 2.0 Hz was applied on the vertical component of the NARS-Botswana data, prior to the STA/LTA detector data processing.

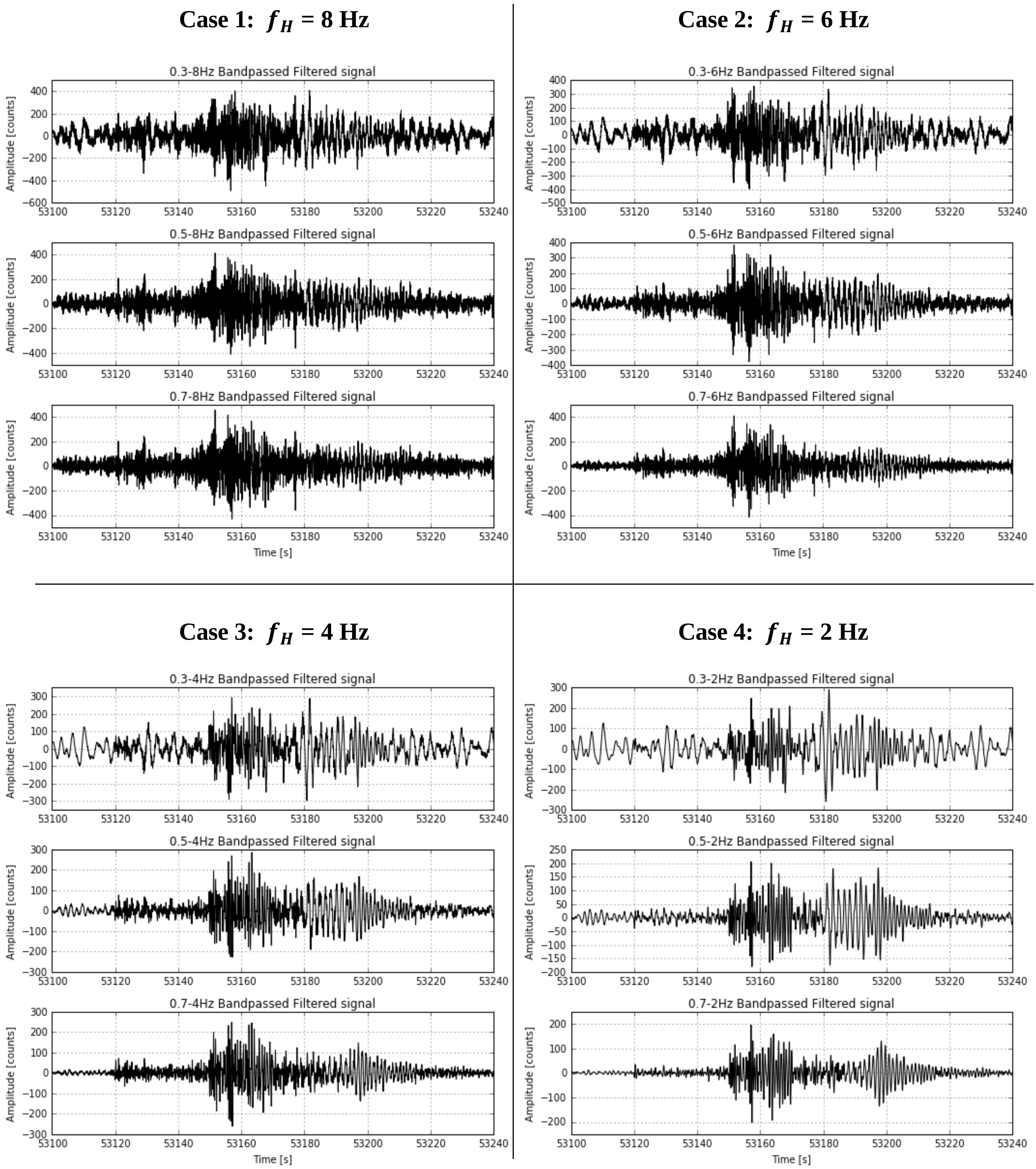

Figure 3.2. Filtered time signals with different bandpass ranges for a local event in Botswana on February 23rd, 2016 recorded by station NE219.

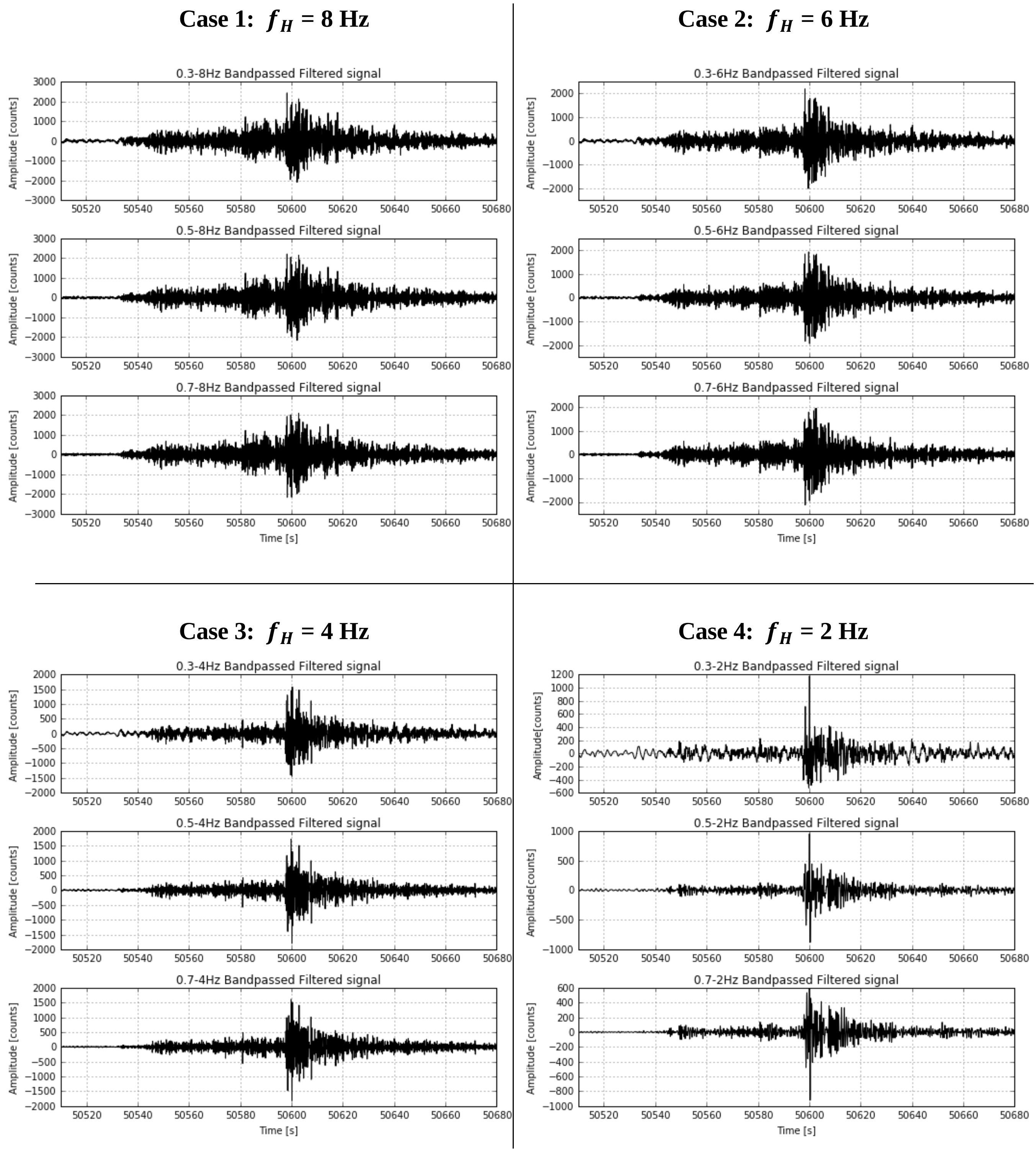

Figure 3.3. Filtered time signals at different bandpass ranges for an event in Botswana on April 27th, 2015 recorded by station NE221 at a distance of about 448 km.

3.1.2 STA/LTA parameters

STA/LTA parameters were extensively tested by trial and error to analyse how they influenced the STA/LTA detector mechanism. The following are a few examples that demonstrate how different parameters affect the STA/LTA ratio plots. In these examples, the February 23rd, 2016 event was taken under consideration.

Example 1: Implemented STA/LTA parameters

STA (s)	LTA (s)	Trigger Threshold	Detrigger Threshold
0.5	30	3	2

As shown in figure 3.5, the STA/LTA ratios of the February 23rd, 2016 Botswana event, recorded by four NARS-stations, are sensitive to the first *P*-wave arrival in each signal shown in figure 3.4. With the implemented STA/LTA parameters shown above, a correct pick detection is made around the *P*-onset time of the event. This can be observed by the reliable *P* picks made (short vertical green lines) in the filtered seismic signals for each of the corresponding station (figure 3.4).

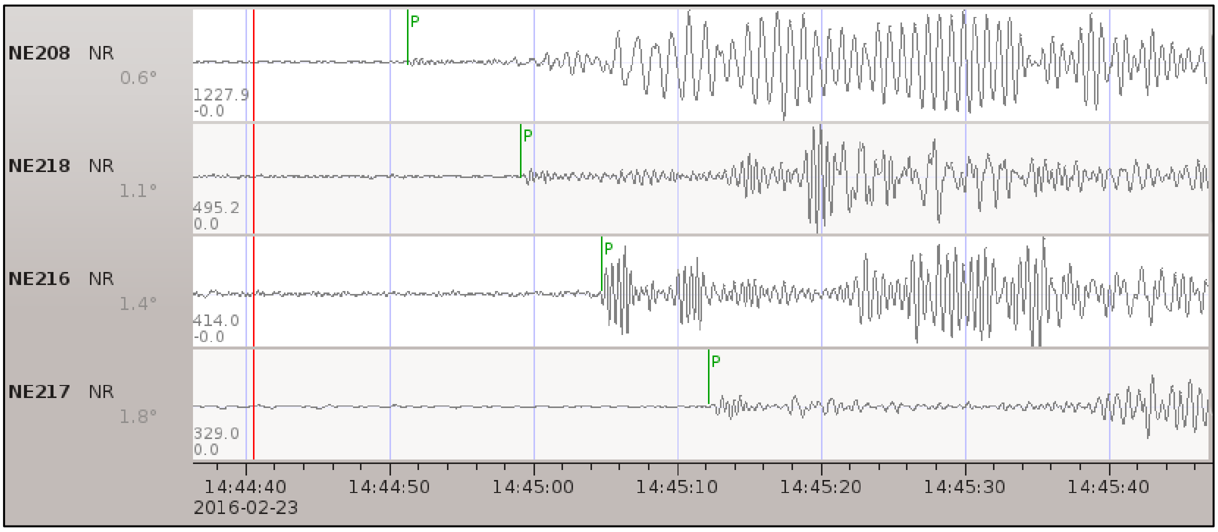

Figure 3.4. Filtered seismic signals generated by SC3 showing the first *P*-wave arrival (small green vertical lines) of the February 23rd, 2016 Botswana event recorded by four NARS-Botswana stations. To the left of each signal, the distance between the station and the seismic event is shown in degrees. The long red vertical line passing through all the filtered signals, represents the origin time of the event. Amplitude values representing the maximum and mean values of each signal are presented before the red line.

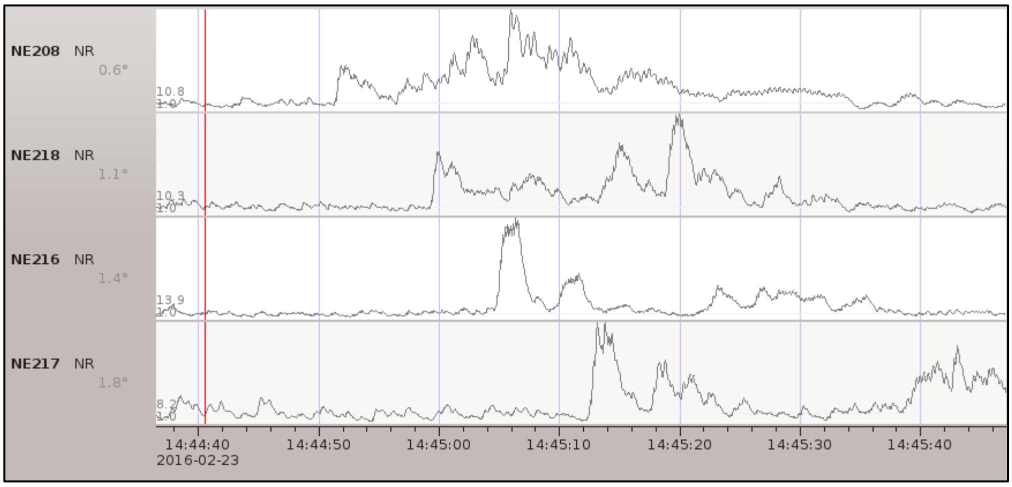

Figure 3.5. STA/LTA plots corresponding to the parameters implemented in example 1. The maximum and minimum STA/LTA ratio values of each signal are illustrated on the bottom left of each STA/LTA plot (before the red vertical line indicating the origin time). In the grey area, to the left, the distance between each station and seismic event is given in degrees.

Example 2: Shorter STA time window

STA (s)	LTA (s)	Trigger Threshold	Detrigger Threshold
0.3	30	3	2

A short STA window duration provides higher sensitivity to short lasting local seismic events. In fact, as shown in figure 3.6, the STA/LTA plots for the February 23rd, 2016 Botswana event have more peaks than the STA/LTA plots in figure 3.5. By decreasing the STA window, more picks are often produced around the estimated onset time. Due to the many picks produced by a single station, the locator module might consider them as possible glitches and thus, does not declare an event. As a result, SC3 did not detect the February 23rd, 2016 Botswana event for this configuration.

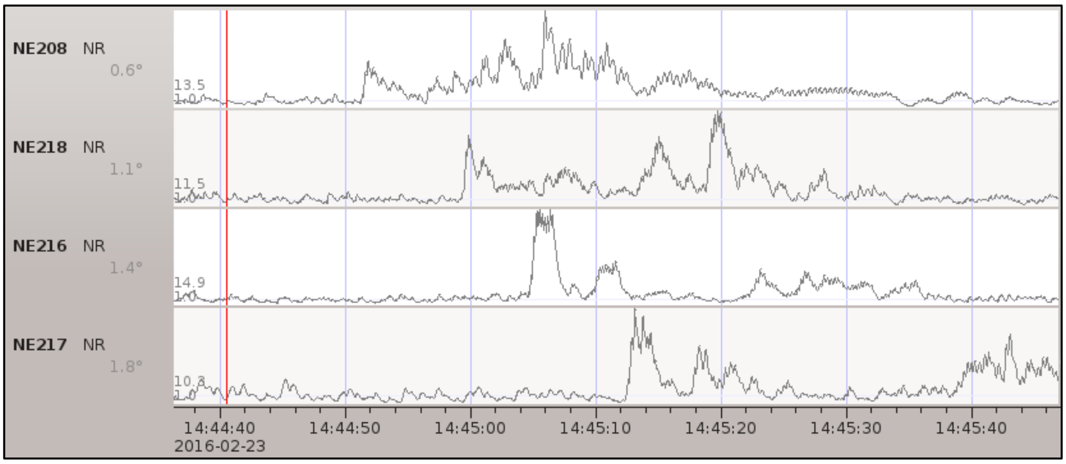

Figure 3.6. STA/LTA plots similar to figure 3.5, but for the parameters applied in example 2.

Example 3: Longer STA time window

STA (s)	LTA (s)	Trigger Threshold	Detrigger Threshold
1	30	3	2

By increasing the duration of the STA window, the STA/LTA detector became less sensitive to local events but more sensitive to distant ones. In fact, with this configuration, the event that occurred in Botswana on the 23rd February 2016 was not detected. However, a distant seismic event located to the South of Australia was detected later, the same day. If we look at the STA/LTA plots for the February 23rd, 2016 Botswana event, shown in figure 3.7, one can observe that the maximum and minimum STA/LTA values (at the bottom left of each plot) are much lower than the ones in the previous examples. In this case, the STA/LTA ratio might have not exceeded the trigger threshold set and thus, did not detect the seismic event in Botswana.

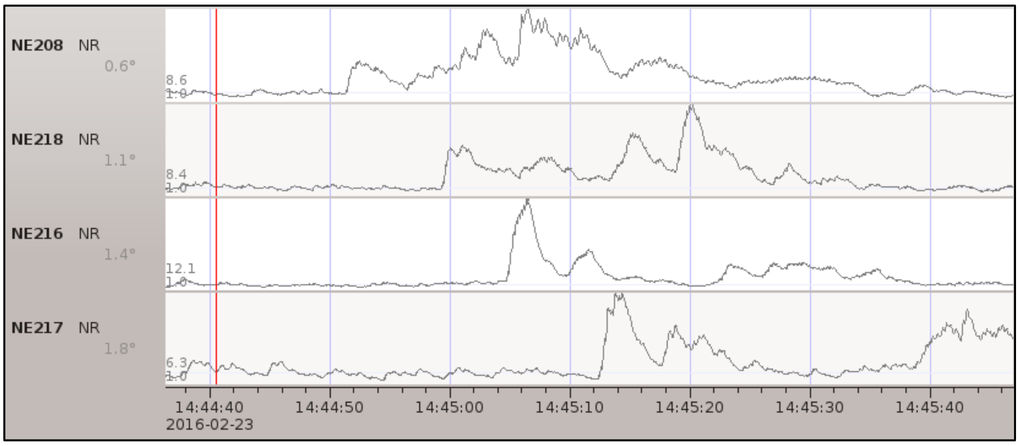

Figure 3.7. STA/LTA plots similar to figure 3.5, but for the parameters applied in example 3.

Example 4: Shorter LTA time window

STA (s)	LTA (s)	Trigger Threshold	Detrigger Threshold
0.5	10	3	2

When a shorter LTA parameter was used, lower STA/LTA ratio values were attained (figure 3.8). This configuration basically diminishes the detector's sensitivity to seismic events. Consequently, no event was detected on February 23rd, 2016.

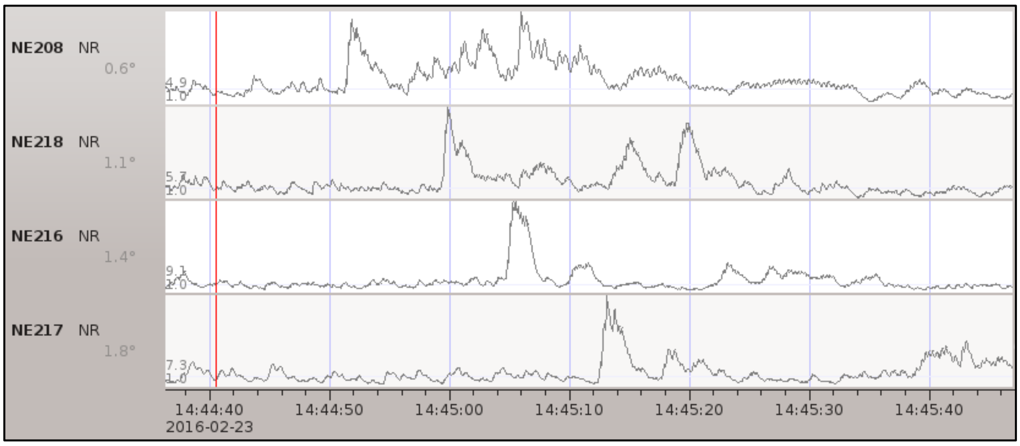

Figure 3.8. STA/LTA plots similar to figure 3.5, but for the parameters implemented in example 4.

Example 5: Longer LTA time window

STA (s)	LTA (s)	Trigger Threshold	Detrigger Threshold
0.5	60	3	2

A long LTA window duration, increases the sensitivity of the detector to distant events. In fact, when these parameters were implemented in SC3, only a distant event (same as example 3) was detected. When using such a long LTA window, the LTA value does not change very rapidly with the occurrence of a seismic event. Hence, higher STA/LTA values are obtained (see maximum and minimum STA/LTA values in figure 3.9).

One must be cautious here for events which have considerably larger amplitude surface waves compared to *P* waves, such as the top two signals in figure 3.4 recorded on 23rd February, 2016 for stations NE208 and NE218. In this case, as illustrated in the top two STA/LTA plots in figure 3.9, *P* waves might barely get detected but the bigger later phase waves, with larger STA/LTA values, might easily exceed the trigger threshold. As a result, the *P*-phase picker, which is implemented around the results obtained by the STA/LTA detector, might not pick the correct *P*-wave onset time.

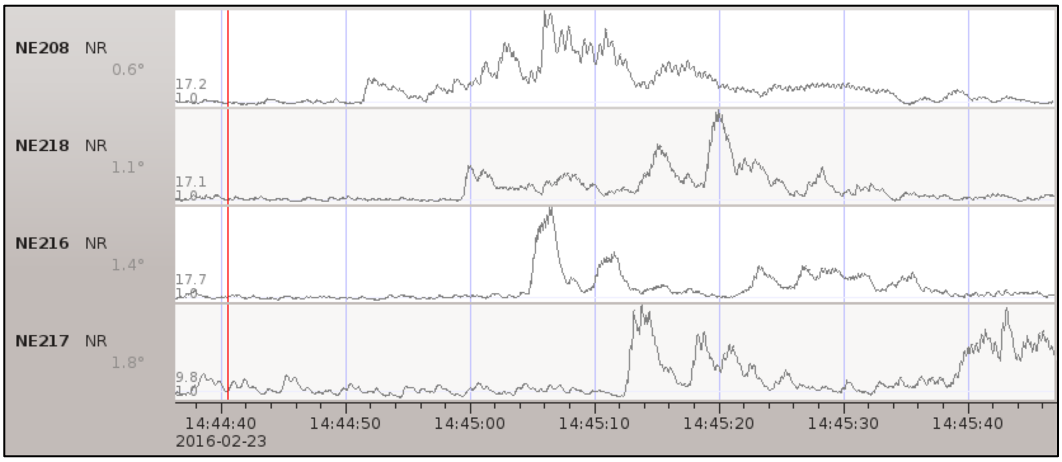

Figure 3.9. STA/LTA plots similar to figure 3.5, but for the parameters implemented in example 5.

Example 6: Lower threshold levels

STA (s)	LTA (s)	Trigger Threshold	Detrigger Threshold
0.5	30	2	1

The lower the STA/LTA trigger threshold level is, the more sensitive the detector will be to identify seismic events. However, with such low trigger threshold, more frequent false event detections might be made. In this case, the picker will produce more frequent picks which the locator module in SC3 might view as possible glitches and thus, set to ignore. This might have been the reason why the STA/LTA detector corresponding to these parameters failed to detect any event on February 23rd, 2016. Furthermore, when a low detrigger threshold level is set, the STA/LTA ratio value might not be allowed to fall below this set value. Thus, the STA/LTA detector might have not terminated its process.

Example 7: Higher threshold levels

STA (s)	LTA (s)	Trigger Threshold	Detrigger Threshold
0.5	30	4	3

By setting a high trigger threshold level one is restricting the STA/LTA detector to detect only strong seismic events. Thus, the magnitude (M) 3.1 event located in Botswana on February 23rd, 2016, in this case, was not detected.

3.1.3 AIC picker parameters

After an event has been detected, the AIC picker is implemented to the vertical component of the filtered data, around the initial onset detected through the STA/LTA detection process. In order for the picker to automatically pick the P-wave onset, three parameters had to be specified in SC3. These include;

- the filter that is used for signal enhancement prior to applying the AIC picker,
- the time window which specifies when the picker should start and end searching for the global minimum AIC value and
- the minimum signal-to-noise ratio (SNR) allowed.

The optimal parameters were chosen via a trial and error process. As shown in figure 3.10, accurate P-onset picks were obtained by applying the AIC picker on Butterworth fourth order bandpass filtered (0.5 – 5.0 Hz) traces, within a time window of length 5 s, starting 3 s before the initial STA/LTA detection and 2 s after. A smaller time window can very often lead to multiple fake picks. On the other hand, a larger time window may include multiple seismic phases. In the latter case, the AIC picker will pick the strongest phase that might not indicate the first P-wave arrival. Furthermore, to reduce the risk of identifying fake picks, only traces with SNR greater than 3 were used. This means that traces with SNR below this configured minimum value were removed from further processing.

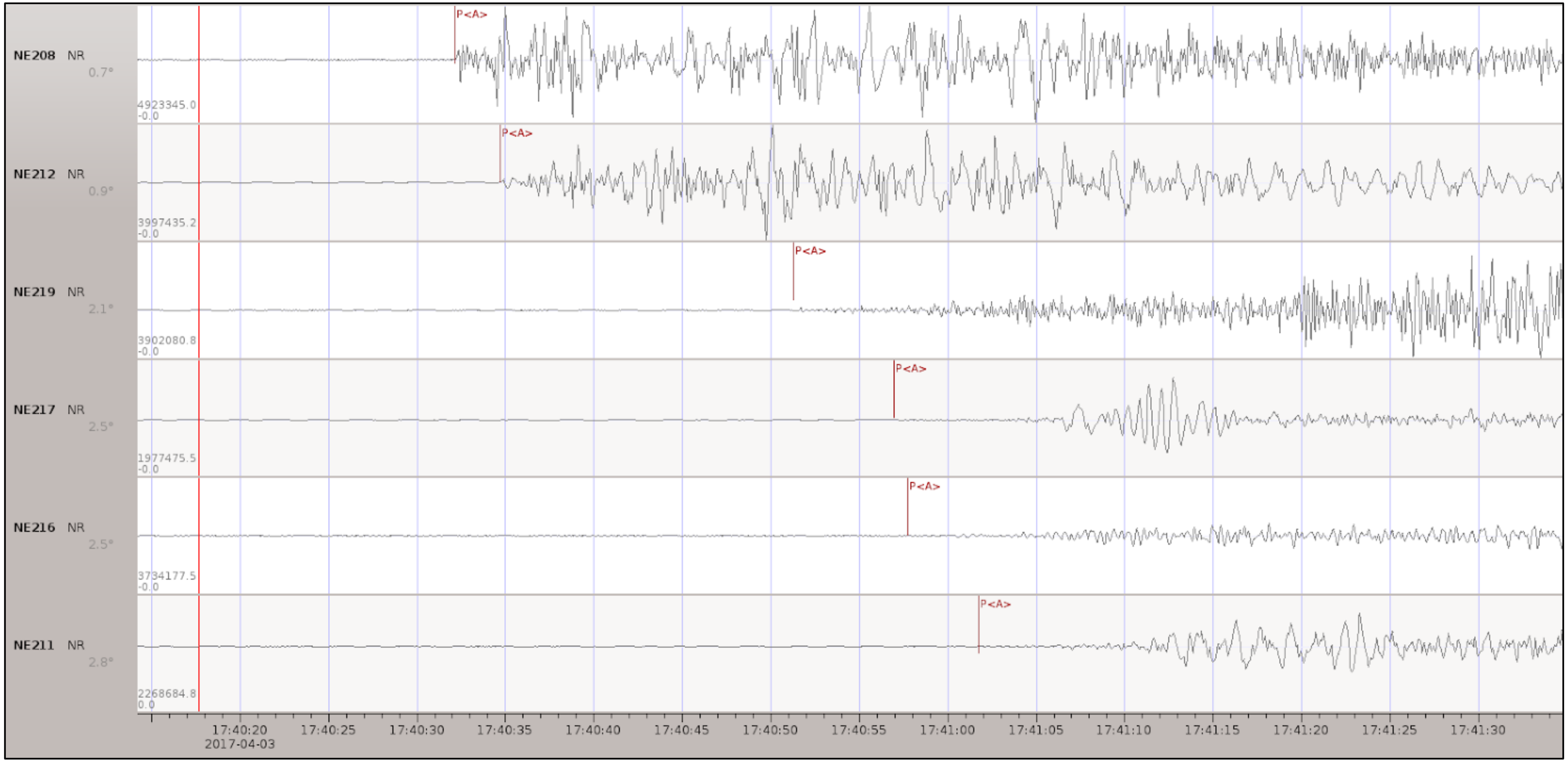

Figure 3.10. Automatic AIC picker performance on six vertical component data of the recorded April 3rd, 2017, strong Botswana event. The long red vertical line passing through all the filtered signals, on the left, represents the origin time of the event. The short vertical lines indicating the first *P*-wave arrival for each signal, represent the automatic picks performed by the AIC picker.

3.2 Automatic event location

The module *scautoloc* in SC3 is responsible for locating seismic events automatically. It is a program that runs as a background process, continuously reading incoming picks determined by the AIC picker. Each pick produced is accompanied by two types of amplitudes, namely SNR and m_b amplitudes. Table 3.2. lists some of the most important input parameters that need to be set in the *scautoloc* module.

Before calculating the hypocenter of a seismic event, *scautoloc* tries to filter out picks that are most likely incorrect. In particular, it checks whether too many frequent picks are generated by a station. In this case, these picks are considered to be probably wrong and must therefore be filtered out. Besides pick filtering, *scautoloc* attempts to associate an incoming pick with a previously calculated origin (note that an origin in SC3 refers to a calculated hypocenter and origin time), in particular those picks related to a strong event which *scautoloc* has already localised. If several picks fail to be associated to an already determined origin, then *scautoloc* uses these picks to compute a new event location. In this process, a grid search in combination with the LocSAT location program (Bratt and Nagy, 1991) is performed. Within the grid search approach, possible event locations are determined. A default grid file, consisting of evenly spaced discrete points at the surface and depth points limited to areas of known deep seismicity, is used by SeisComP3 (GFZ Potsdam, 2018). Potential locations are identified by comparing the observed arrival times of P phases with those predicted by a reference velocity model, defined by *autoloc.locator.profile*. The grid points with the smallest misfit are then considered as possible event locations. The LocSAT location program is then launched to check these potential locations obtained by the grid search. This program determines the best fitting location by using an iterative least squares inversion technique until the RMS residual is sufficiently minimized (Bratt and Bache, 1988). If the RMS residual acquired by LocSAT is too large, associated picks with large residuals are removed and an improved location is tested to check if a reduction in the RMS residual can be achieved. Moreover, location uncertainties are also computed by the LocSAT program.

Finally the estimated hypocenter location is refined by checking the corresponding amplitudes provided with each pick. These amplitudes provide essential information needed in order to compare origin qualities. For instance, a pick with high SNR and m_b amplitudes is likely to correspond to a real seismic onset and thus will provide a better estimated location.

Table 3.2. A description of a few important input parameters specified in the *scautoloc* module, along with the implemented configurations (GFZ Potsdam, 2018).

Parameter	Description	Configuration
locator.defaultDepth	Default depth used as a fixed depth if the same location quality (e.g. pick RMS) for the estimated depth can be attained. This is mostly the fixed depth for shallow events.	10 km
locator.minimumDepth	Minimum depth allowed for a location to be reported	1 km
autoloc.maxRMS	Maximum RMS allowed for a location to be reported	3.5 s
autoloc.maxResidual	Maximum individual pick residual	7.0 s
autoloc.minPhaseCount	Minimum number of automatically detected P-phases needed to report an event location	6
autoloc.locator.profile	Locator profile used	iasp91 (Kennett and Engdahl, 1991)

3.3 Amplitude and magnitude calculations

A small set of amplitudes for magnitude types M_{Lv}, m_b, m_B and $M_w(m_b)$ (see table 3.3 for descriptions) are computed by two particular modules in SC3, namely, *scautopick* and *scamp*. Apart from automatic picking, *scautopick* measures the SNR and the amplitudes used in M_{Lv}, m_b and m_B magnitude calculations. These amplitudes are computed for each automatic pick within a fixed time window, starting at the P-wave pick time. The module *samp*, on the other hand, measures amplitudes which *scautopick* did not calculate. In our case, it measures the amplitude used to estimate $M_w(m_B)$ which is the moment magnitude M_w based on m_B magnitudes. In addition, *scamp* also calculates amplitudes for manual picks.

Usually, all amplitudes are calculated once and reported to the database immediately. However, if the location of an event changes significantly, for instance due to enhanced manual picks, amplitudes need to be recomputed. These amplitudes are reused by the magnitude computation module, *scmag*, which effectively updates the corresponding magnitudes for that particular event.

Table 3.3. Magnitude types calculated in SC3 and their corresponding description (GFZ Potsdam, 2018).

Magnitude Type	**Description**
M_{Lv}	Local magnitude (Richter, 1935) calculated on the vertical component
m_b	Narrow band body wave magnitude (0.7 - 2 Hz) (e.g., Veith and Clawson, 1972)
m_B	Broad band body wave magnitude (1 – 3 Hz) (Bormann and Saul, 2008)
$M_w(m_B)$	Moment magnitude derived from m_B magnitudes (Bormann and Saul, 2008)
M_{wp}	Broadband moment magnitude based on the first P-wave arrival (Tsuboi et al., 1995)
$M_w(M_{wp})$	Moment magnitude derived from M_{wp} magnitudes (Whitmore et al., 2002)

Scmag is a module which operates in conjunction with *scamp*. Its task is to calculate the magnitudes indicated in table 3.3 using the magnitude scales defined in the glossary section of the SC3 documentation (GFZ Potsdam, 2018).

Among all the available magnitude calculations, the preferred event magnitude in SC3 is the composite magnitude M. This is obtained from a weighted average of the individual well-determined magnitudes. In SC3, it is referred to as the summary magnitude M and is calculated as follows (Hanka et al., 2010; GFZ Potsdam, 2018):

$$M = \frac{\sum w_i M_i}{\sum w_i} \qquad \text{with } w_i = a_i n_i + b_i \quad (3.1)$$

where i is the magnitude type index,

w_i is the weighting factor of a magnitude type i,

m_i is the network magnitude of type i and

n_i is the number of station magnitudes of type i.

Since the only two types of magnitudes used to compute M, in our case, are M_{Lv} and m_b, the configured values for the coefficients a_i and b_i in equation (3.1) are:

- $a_i = 0$ for both magnitudes types M_{Lv} and m_b
- $b_i = 1$ for magnitude type m_b while $b_i = 2$ for magnitude type M_{Lv}.

The summary magnitude M in SC3 is considered to be a best possible compromise among all magnitudes (GFZ Potsdam, 2018). In this regard, it was decided to publish only automatic magnitude solutions related to the summary magnitude M in the final Botswana earthquake catalogue. However, it is very important to keep in mind that large uncertainties often exist in individual magnitude types, especially when these are calculated automatically. Thus, large discrepancies might also exist in the estimated summary magnitude M.

3.4 Automatic event association

During the localization process, SC3 creates several origins (hypocenters with their corresponding origin time) for one seismic event (see upper list in figure 3.11). These origins are based on the available amount of P-wave picks at a specific time. In fact, as time goes by during the processing of the data, more automatic picks are available and therefore, more reliable origins will be reported. The module *scevent* receives different origins and tries to associate them to one event. This association is based on comparisons between epicentre location variations, origin time differences and similarities in the P-wave picks. The origin with the most amount of automatically detected P-wave picks, along with the smallest RMS residual is then selected by SC3 as the best estimated location and origin time for that particular event. On the other hand, if an incoming origin does not match to any identified event, *scevent* will form a new event comprising of this new origin.

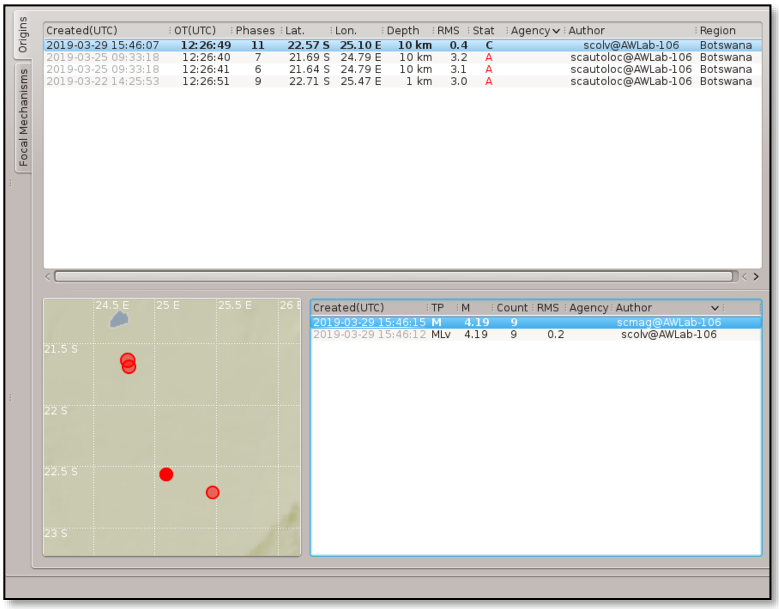

Figure 3.11. Associated origins to the April 5th, 2017 event. The upper list illustrates information about each origin while the lower list displays the computed magnitudes. The preferred origin and magnitude are highlighted in blue in both lists. The map, located in the lower left part, shows the locations of the associated origins with the filled circle representing the preferred origin.

3.5 Event analysis and manual picking

Automatic event solutions such as picks, hypocenter location, origin time and magnitudes are reviewed and revised through the interactive tool *scolv* (SC3 Origin Locator View). *Scolv* is a GUI that allows interaction with and management of the event catalogue, access to all origins associated with each event, manual picking of data, relocation of events and magnitude review.

Figure 3.12. illustrates the event location tab in *scolv* for the event recorded on October 11th, 2016. A detailed list of all the detected *P*-phase arrivals recorded by the NARS-Botswana network is provided (lower part), along with arrival residual plots, travel time and move-out curves (upper right part).

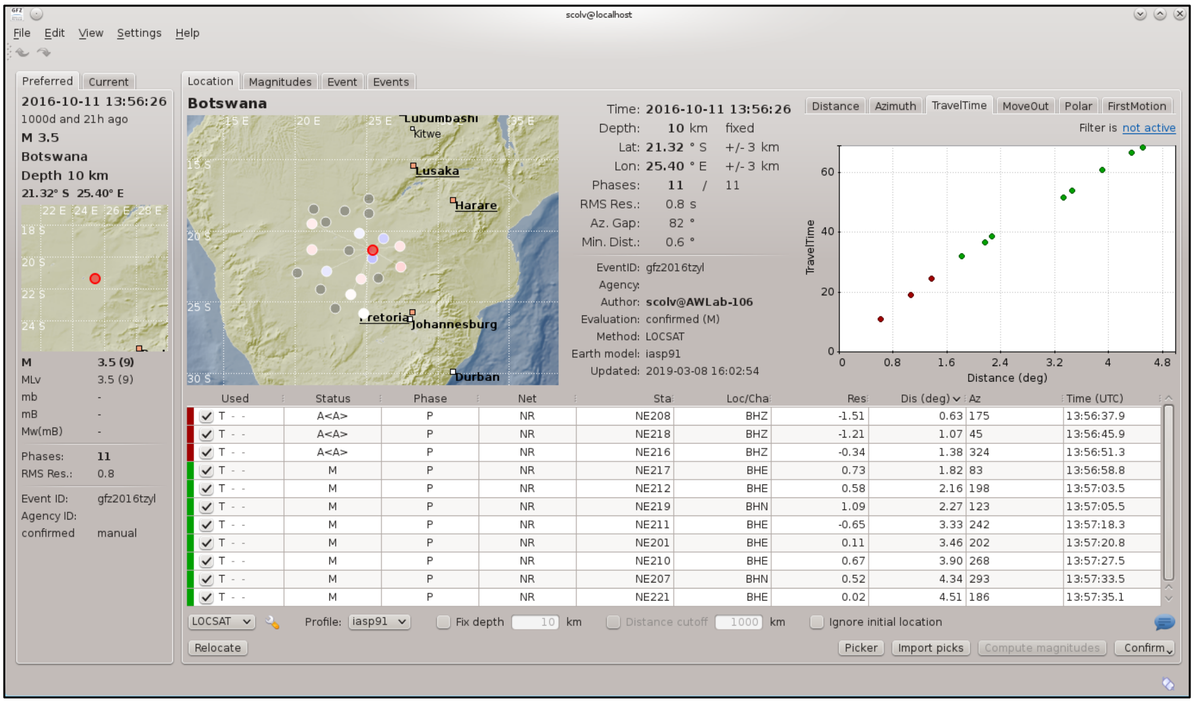

Figure 3.12. *Scolv* location window showing the solution for the October 11th, 2016 event.

By accessing the waveform picker window, shown in figure 3.13, automatic picks (shown by short vertical red lines) are analysed separately. Among many features, this window enables one to zoom in traces, add unpicked stations and perform manual picking on the vertical component of each trace. Figure 3.14 demonstrates an example of a clear *P*-phase onset, however, the automatic AIC picker (red line) did not pick this onset accurately. In such cases, the *P*-phase onset was picked manually. This was performed by first selecting one of the available bandpass filters in *scolv* that gave the clearest onset. By zooming in the trace it was then possible to mark this onset point accurately (green line).

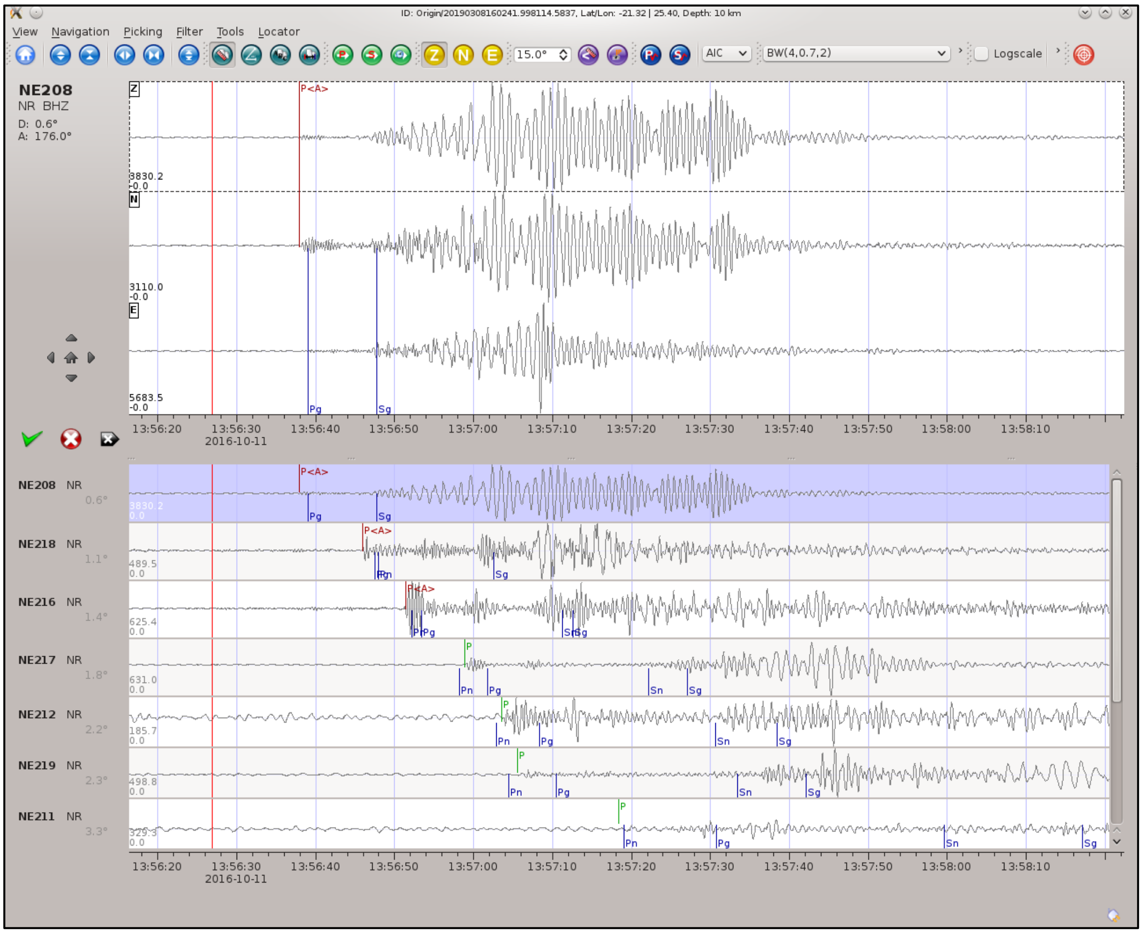

Figure 3.13. Waveform picker window for the strong event recorded on October 11th, 2016. This window is divided into two parts; the zoom trace in the upper part and the trace list in the lower part. In the trace list only the vertical component is shown. Each of these traces is aligned by the origin time (long vertical red line, on the left) and marked by either a darker red short line to indicate automatic picking or a green short line to indicate manual picking. Additional *P* and *S* phases, calculated automatically using the iasp91 velocity model (Kennett and Engdahl, 1991), are also displayed in this window.

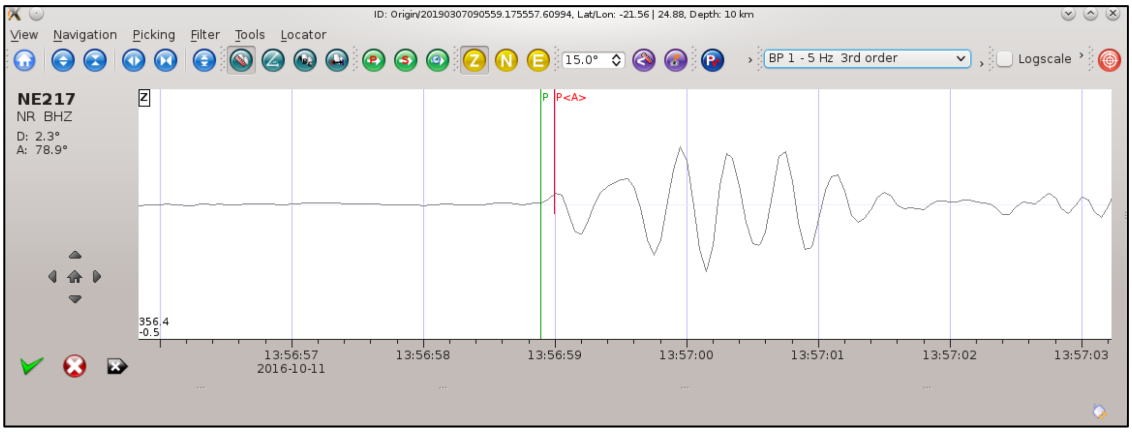

Figure 3.14. An example of a zoomed trace showing the performance of the automatic AIC picker (red) as compared to the manual pick (green) for the October 11th, 2016 event recorded by station NE217.

Events reported by the ISC but not detected with SC3 were also analysed in *scolv*. This was achieved by creating preliminary seismic events in *scolv* with the event solutions provided by the ISC as the input parameters. Consequently, manual analyses and picking of each available trace was performed in the corresponding waveform picker window.

All detected events in a defined time span are illustrated in the events tab of *scolv*. As shown in figure 3.15, this window provides information about the origin time (OT), magnitude solution for the selected type of magnitude (TP), amount of detected *P*-phase arrivals, epicentre and depth, region and the corresponding event ID.

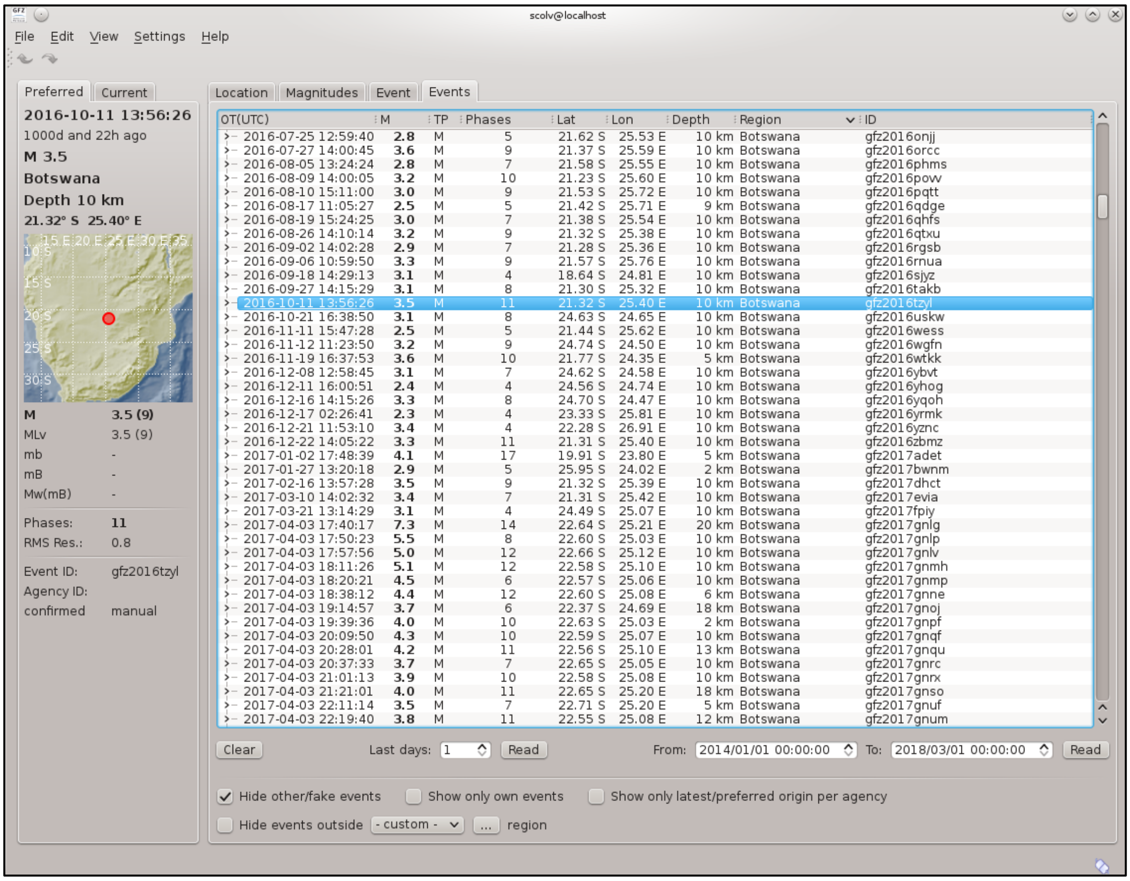

Figure 3.15. Botswana event list window in *scolv*.

4. Results and Discussion

4.1 Detected and located seismic events in Botswana

Botswana forms a major gap in our understanding of southern Africa's seismic activity. By processing the NARS-Botswana data from January 1st, 2014 to March 1st, 2018, an earthquake catalogue for Botswana has been created in order to provide a reliable assessment of the seismicity in Botswana and contribute positively towards hazard mitigation. The complete Botswana earthquake catalogue is included in Appendix A. It contains the computed locations and magnitudes of 376 detected events in Botswana.

The distribution of seismic events according to magnitude values in the Botswana earthquake catalogue is shown in figure 4.1. There are a total of 62 events with summary magnitude (M) greater than 4.0, one of which has a 7.3 magnitude, representing the strongest earthquake recorded in Botswana since 1952. The incompleteness of this catalogue is indicated by the small number of seismic events with magnitude (M) less than 3.0. This is mainly due to the large distances between seismic stations and the location of small events, making it difficult for SC3 and other seismological agencies to detect and locate these small events accurately. Moreover, small events might have been recorded by only a few NARS-Botswana seismic stations. However, in order to report an event location, the location module *scautoloc* in SC3 requires each seismic event that is automatically detected to be recorded by at least six stations, whereas those seismic events detected manually, by using the ISC event solutions as input parameters, require each event to be recorded by a minimum of four stations. Otherwise, events are ignored by the automatic location process within SC3.

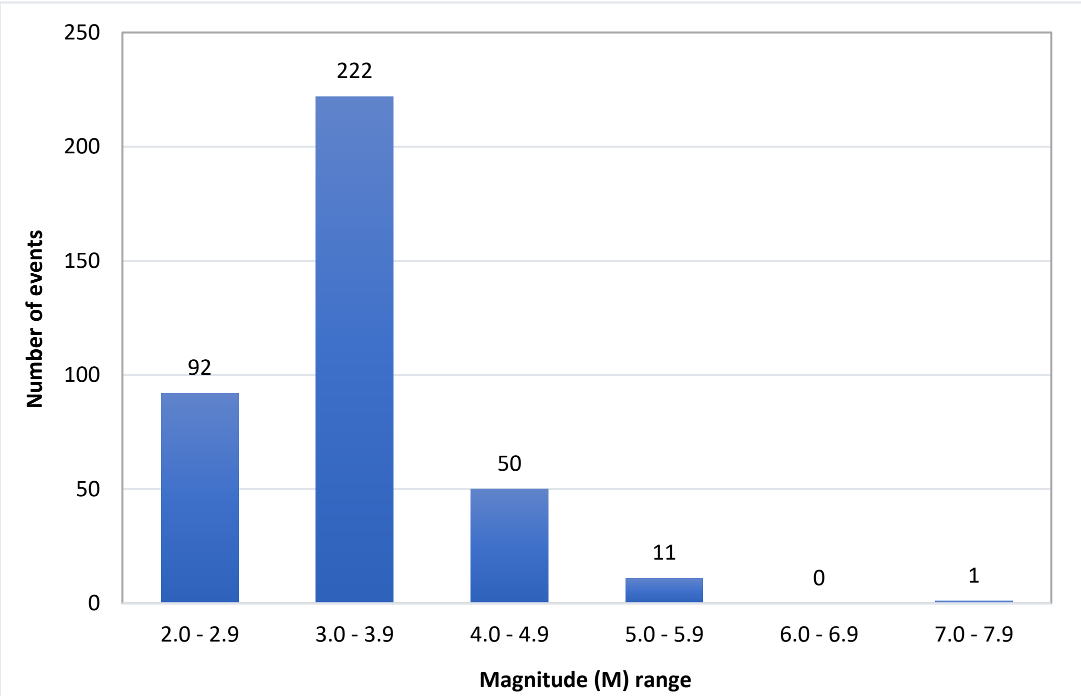

Figure 4.1. Botswana event catalogue magnitude (M) distribution.

Figure 4.2 shows the annual distribution of detected events for the years 2014 until 2017. A considerable increase in seismic activity can be observed from 2016. This is attributed to the fact that during 2014 and 2015 some NARS-Botswana seismic stations were still being installed. In fact, only by 2016 all the 21 stations were operational. However, due to battery failure, certain seismic stations did not always record data during the studied years.

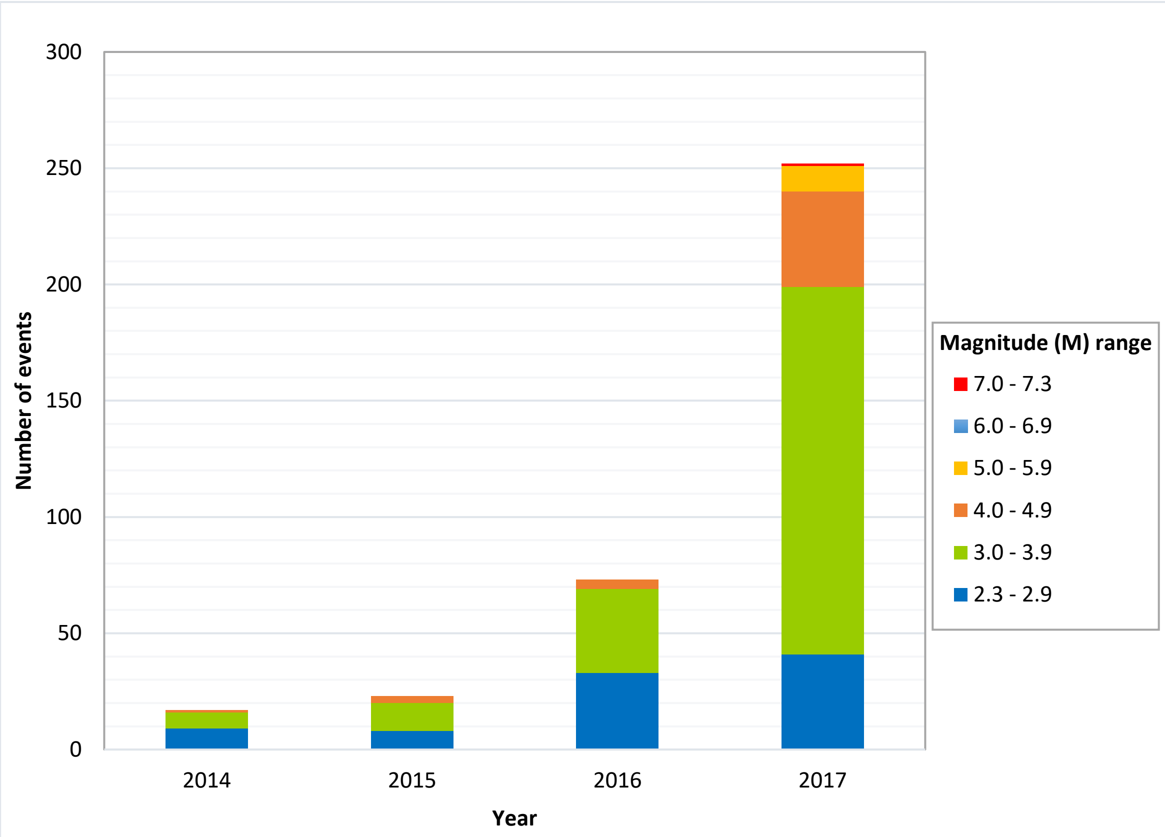

Figure 4.2. The annual number of detected events in Botswana for the years 2014 till 2017.

A map of all the events documented in the Botswana earthquake catalogue, with summary magnitude (M) ranging in between 2.3 and 7.3, is shown in figure 4.3. This seismicity map shows that most of the seismic events that occurred in the Okavango Rift Zone (ORZ) were of low-to-moderate magnitudes ranging from 3.0 to 4.9, while those above 4.9 appearing mainly in central Botswana where the April 3rd, 2017 strong earthquake occurred.

Within the ORZ (northern part of Botswana), seismic activity was highest along the south-eastern edge of the delta where a clear cluster of events can be observed between the NE-SW striking Thamalakane and Tsau faults (refer to figure 1.5 for fault names). A few other events located along the western part of the Chobe fault and below the Nare fault might also form part of this cluster of events which is trending in a NNW-SSE direction, for a length of about 184 km. This clustering of events in the ORZ suggests the development of an active rift which might correspond to the southwestern continuation of the EARS (Scholz et al., 1976; Modisi et al., 2000; Kinabo et al., 2007; Leseane et al., 2015). Among the three depocenters outlined by Kinabo et al. (2007), only the Mababe Depression and the Chobe regions show seismic activity. However, Lake Ngami, the third depocenter (located at the southern part of the Kunyere fault), shows no seismic activity. It is further to the north of the Kunyere fault (i.e. the southern edge of the delta) that some earthquake activity is observed. No seismic events were detected in the western part and in the central part of the delta.

Shemang and Molwalefhe (2011) suggest that the lack of large magnitude earthquakes within the ORZ may be associated with the inflow of large amounts of fluids into the Okavango Delta region. They proposed that the relationship between seismicity and fluid flow in the ORZ is similar to the San Andreas Fault (SAF) (e.g. Unsworth et al., 1999 and Unsworth and Bedrosian, 2004). These studies related to the SAF suggest that the seismic behaviour within fault zones might be controlled by a network of connected fluid-filled cracks. With this regard, Shemang and Molwalefhe (2011) concluded that fluid migration, in particularly along the northern segments of the Kunyere and Thamalakane faults, may cause an increase in pore pressure within rocks, reducing the frictional stress during an earthquake.

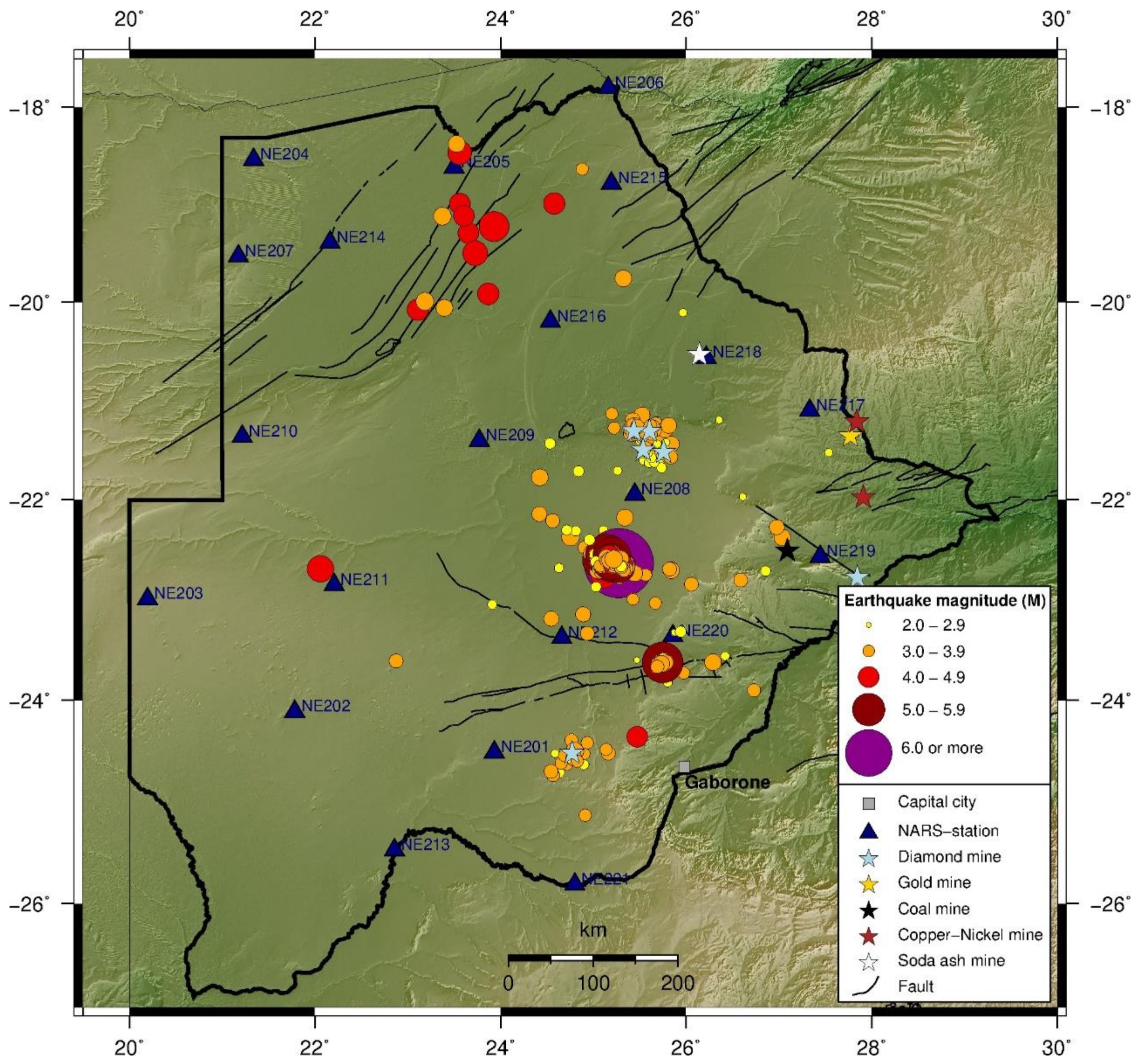

Figure 4.3. Locations of seismic events (coloured circles) of the Botswana earthquake catalogue (Appendix A). Locations of major faults are from Mulabisana (2016) and Midzi et al. (2018).

The only event detected in western Botswana is the April 27th, 2015 seismic event at $(-22.693°, 21.989°)$ with summary magnitude (M) 4.5 (figure 4.3). According to the tectonic map of Fadel (2018), this event is located in the Okwa block (figure 4.4). This event has a depth of 1.756 ± 5.325 km, indicating its occurrence in the uppermost layer of the crust. It is possible that this event represents a boundary between different tectonic units, however, more seismicity is needed to be detected to verify this.

Another earthquake with M 5.6 occurred on August 12th, 2017 at $(-23.626°, 25.678°)$ inside the Kaapvaal Craton (figure 4.4) to the southeast of Botswana. As shown in figure 4.3, this event appears to be mapped along the Zoetfontein fault (refer to figure 1.3 for the location of the Zoetfontein fault). However, the focal mechanism for this event (Bouwman, 2019) indicates a normal fault with either a southwest or northeast dipping fault. By taking a closer look at figure 4.3, it can be observed that this event is located very close to the junction of three major faults. Due to the focal mechanism of this event, it is more likely that this event corresponds to the mapped fault north of the Zoetfontein fault.

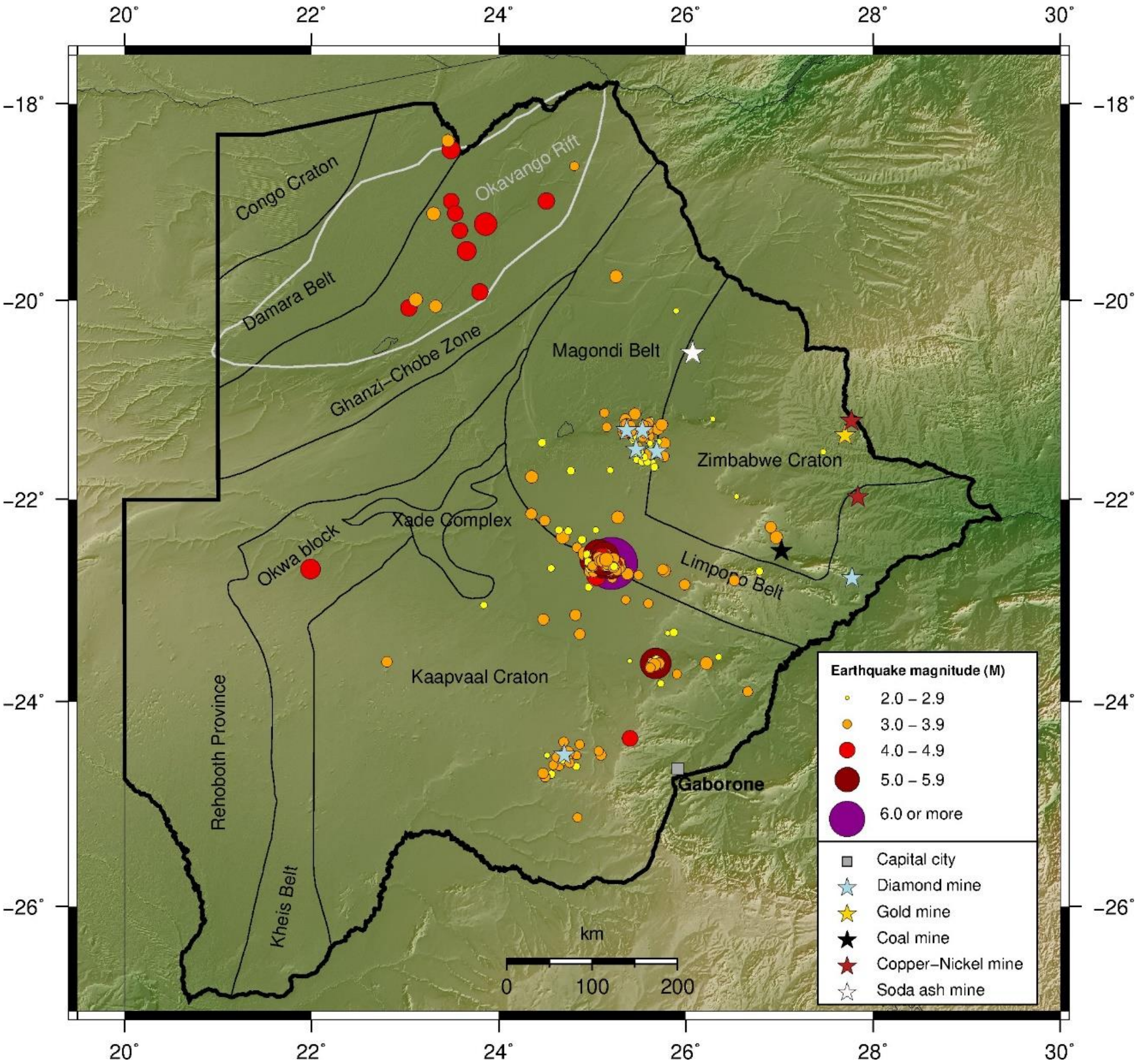

Figure 4.4. Map of Botswana showing the main tectonic units from Fadel (2018) together with the locations of the seismic events detected in this study.

The magnitude (M) 7.3 earthquake in central Botswana, near Moiyabana is the largest event recorded in Botswana by the NARS-Botswana network (hereafter referred to as the Moiyabana earthquake). This earthquake occurred on April 3rd, 2017 at 17:40:17 UTC, close to the junction between the Kaapvaal Craton and the Limpopo Belt (figure 4.4). According to Bouwman (2019) this event occurred along a normal fault that dips towards the northeast and has a NW-SE strike. This is quite consistent with the strike of the Kaapvaal Craton's northern boundary. By using the double difference technique to relocate the mainshock and several aftershocks of the 2017 Moiyabana earthquake Bouwman (2019) deduced that these earthquakes might have reactivated an existing thrust fault, named the Moiyabana Fault, in the Limpopo Belt. It is further interpreted that this fault is related to the deformation associated with the collision of the Kaapvaal and Zimbabwe Cratons. Similar conclusions have also been made by Kolawole et al. (2017) using aeromagnetic data and Moorkamp et al. (2019) using magnetotelluric data.

With a hypocenter at a depth of 20.4 $\pm$ 9.6 km, the Moiyabana earthquake is surprisingly deep for a rifting event. Materna et al. (2019) identified this event in the lower crust. Previous events in southern Africa have also been identified in the lower crust and upper mantle (Yang and Chen, 2010), indicating that despite high temperatures these areas can withstand high differential stresses. Moreover, the large depth of the 2017 Moiyabana earthquake may be associated with its location along the Kaapvaal Craton's northern boundary. Mooney et al. (2012) in fact showed that intraplate earthquakes often concentrate along the edges of cratons. In addition, Craig et al. (2011) showed that southern Africa's deepest rifting events are likely to occur along the boundaries of ancient cratons (Materna et al., 2019).

The 2017 Moiyabana earthquake occurred in a remote area with no historic or previous evidence of similar magnitude events, and very little topographic relief (Materna et al., 2019). Between January 1st, 2014 and April 2nd, 2017, the mainshock is observed to be preceded by two potential foreshocks in the epicentral area of the mainshock (Table 4.1) at distances less than 42km away from the mainshock. None of these detected foreshocks match the foreshocks detected by Gardonio et al. (2018) using a template matching technique. This template matching technique used data from five stations at distances from 1200 to 2000 km from the mainshock for the period between November 2016 and April 2017. According to Gardonio et al. (2018) two foreshock swarm-like sequences, consisting of a total of fourteen events, were observed prior to the mainshock. By utilizing the NARS-Botswana data (i.e. near-field strong motion data), it was possible to verify that none of the fourteen events corresponded to a detected event in this (or the ISC) catalogue. It is suspected that these false results are due to data that is recorded at teleseismic distances from the mainshock.

Table 4.1. Detected (fore)shocks in the epicentral area of the 2017 Moiyabana earthquake.

EventID	Date	Origin time (UTC)	Latitude (°) ± error	Longitude (°) ± error	Depth (km) ± error	Summary Magnitude (M)	No. of stations
gfz2014vbum	2014-10-27	19:43:41	-22.401 ± 16.186	24.890 ± 8.311	10.0*	2.9	4
gfz2015evme	2015-03-10	16:09:01	-22.305 ± 15.789	25.038 ± 8.813	10.0*	2.6	4

* Depth fixed

In this study, a sequence of about 216 aftershocks followed the 2017 Moiyabana earthquake, with summary magnitude (M) between 2.5 and 5.7. These aftershocks appear to be clustered along a northwest-southeast trending seismicity zone (figure 4.3). This is consistent with the focal mechanisms of the main event and multiple aftershocks (Bouwman, 2019). Furthermore, these aftershocks show that the Moiyabana Fault might be connected to other distinct faults in the south-eastern part of Botswana. Such faults might be related to the continuation of the mapped faults in figure 4.3. Hence, with reliable seismic events locations it is now possible to locate new, extended or reactivated faults in Botswana, identifying regions of increased hazard.

Most of the detected aftershocks are located at a shallower depth than the main event. Indeed, this observation supports the notion that the rupture along the Moiyabana Fault has an up-dip propagation (Materna et al., 2019; Bouwman, 2019). On the other hand, only four aftershocks were located at a deeper depth than the Moiyabana earthquake. However, these events have a large uncertainty depth error which limits the hypocenter depth accuracy. As discussed in section 2.2.3, this might be due to the large distance between the seismic stations and the location of the event.

The sources of stress that drive intraplate earthquakes can be challenging to identify (Materna et al., 2019). Although the Moiyabana earthquake and its aftershocks occurred in a region that is about 300 km south of the ORZ, Materna et al. (2019) suggested that stress conditions in central Botswana might be related to the EARS. By observing the seismicity pattern in figure 4.4, it is possible that the northwest-southeast trending seismicity zone along the Moiyabana earthquake is related to the rifting in the ORZ, thus suggesting a possible southward propagation of the EARS (Bird et al., 2006; Materna et al., 2019). Similarly, Fadel (2018) suggested that the extension of the EARS towards central Botswana might explain the occurrence of the 2017 Moiyabana earthquake. This interpretation is based on low shear-wave velocities observations below the main event that seem to be directly connected to the low velocity zone in the mantle below the ORZ. This low velocity zone could indicate mantle upwelling which might explain the extensional mechanism and low crustal depth of the main event. Furthermore, the mantle low velocity anomaly observed beneath the ORZ might indicate the continuation of the EARS due to its location at the extended southwestern branch of the EARS (Fadel, 2018). In the upper mantle, Moorkamp et al. (2019) also observed a low surface velocity structure, trending NW-SE at a depth of 75 km in the vicinity of the Moiyabana earthquake suggesting that a region with a weak upper mantle exists between two strong ancient cratons. However, due to the lack of a significant thermal anomaly in the deep lithosphere below the Moiyabana earthquake, Moorkamp et al. (2019) suggested that instead of thermal weakening from the mantle, the main event was triggered from the top by interaction of the ambient stress field with surrounding ancient structures. It is difficult to clearly identify what triggered the 2017 Moiyabana earthquake. More insight into the resolution of the velocity models by Fadel (2018) and Moorkamp et al. (2019) is needed to provide a more detailed view of what might be happening in the crust and mantle beneath Botswana.

Considerable seismic activity with low magnitudes ranging from 2.3 to 3.9 is also observed at $(-21.308°, 25.536°)$, $(-24.523°, 24.702°)$ and $(-22.512°, 27.022°)$, indicating areas where anthropogenic activities take place (figures 4.3 and 4.4). Most of these detected events are concentrated near diamond mining areas, in the south and eastern part of Botswana. Anthropogenic activities such as deep underground mining cause changes in the stresses within the earth's crust and reduce the faults' strength (Gibson and Sandiford, 2013). These activities induce seismicity, that is recorded along with tectonic events. In order to distinguish whether a seismic event is an explosion or an induced earthquake along a fault, can be determined from the radiation pattern.

4.2 Frequency-Magnitude relation

Several catalogue-based approaches are available for assessing the completeness of the catalogue (Mulabisana, 2016). One of the most traditional approaches uses the event frequency-magnitude relation developed by Gutenberg and Richter (1944) in the form:

$$\log_{10} N = a - bM \tag{4.1}$$

where N is the cumulative number of events above a certain magnitude M. The parameter a describes the rate of seismic activity in a given area, obtained from the intercept of the graph $\log N$ against M, while b, referred to as the b-value, is a parameter that characterises the slope of the frequency-magnitude distribution and defines the relative size distribution of events (Nthaba, 2018). Generally, the b-value is roughly equivalent to 1. If b is large (i.e. greater than 1), the studied area is characterised with relatively more small earthquakes, whereas a small b-value (i.e. smaller than 1) would indicate that large earthquakes occur more frequently. Determining an accurate and reliable b-value is important in studies related to seismotectonics, seismic risk analysis, prediction, and hazard (Alabi et al, 2012).

The frequency-magnitude distribution of 117 seismic events located in Botswana is shown in figure 4.5. Events that occurred after April 3rd, 2017 were excluded in order to avoid bias due to the strong earthquake and its subsequent aftershocks. This frequency-magnitude relationship depends on the magnitude of completeness (M_C) for which all seismic events above this particular magnitude are considered to be represented in the event catalogue. In this case, the M_C is considered to be 3.1 since the frequency-magnitude distribution decreases (roughly) linearly above this threshold magnitude.

The Gutenberg-Richter relation, shown in figure 4.5, gives a low a value of 5.21 ± 0.15, suggesting that seismic activity in Botswana is relatively low. In addition, the b-value of 1.10 ± 0.04 indicates that Botswana is a country with mostly small to moderate seismic events. However, one must keep in mind that a longer observational and studied period is needed for a meaningful analysis of the seismic activity in an area. Nthaba et al. (2018), uses the ISC data from 1966 to 2012 to determine the Gutenberg-Richter relation for seismic events in Botswana. However, their resulting a and b values are slightly bigger than the ones found in this study using the NARS-Botswana data.

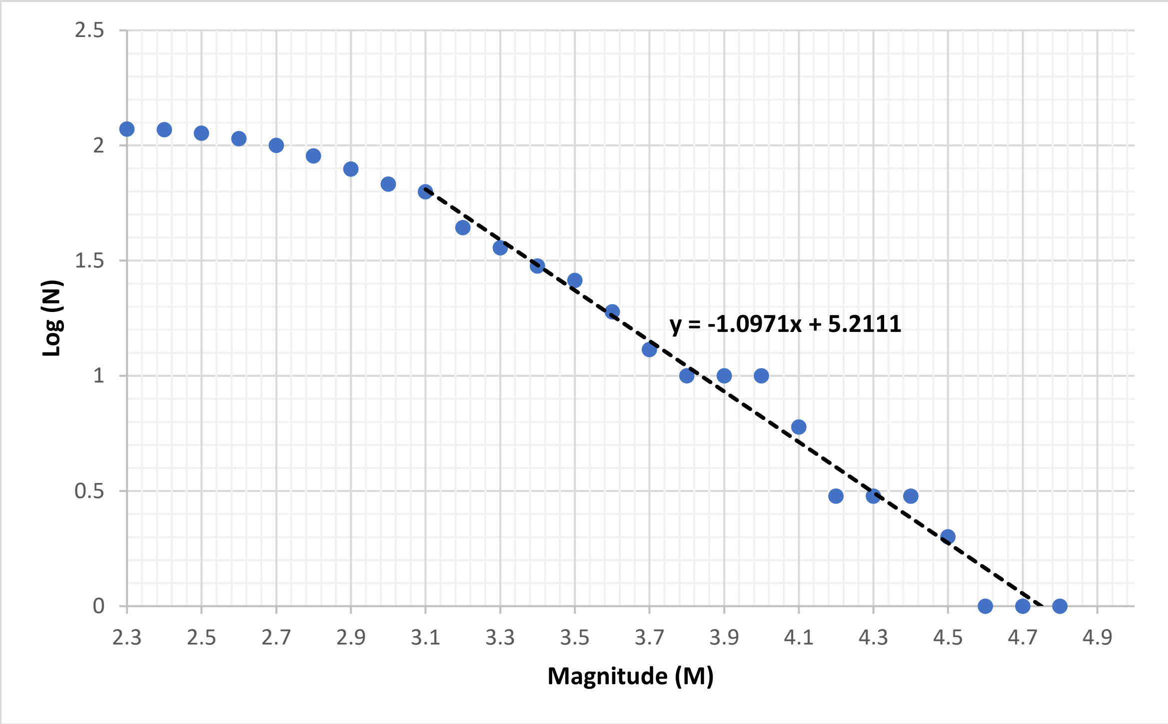

Figure 4.5. The Gutenberg-Richter relationship for the January 1st, 2014 till April 2nd, 2017 Botswana events, along with the line of best fit indicating the magnitude of completeness. Note that the magnitude used is the summary magnitude (M) determined by SC3.

4.3 Computed event locations versus locations reported by the ISC

The event locations were compared with the event locations listed in the ISC on-line bulletin between January 1st, 2014 and March 1st, 2018. Figure 4.6 shows the unreviewed locations reported by the ISC (yellow circles) and the SC3 calculated locations (red and blue circles) in map view. This map shows that the ISC locations are more dispersed than the ones calculated in this study. Moreover, 30 new events (blue circles) which are not reported in the ISC event catalogue, were detected automatically by SC3.

In the southwestern part of Botswana, the ISC located more events than was actually found in this study. By zooming in this region (figure 4.7), matching ISC and SC3-computed event locations were identified based on the time of origin. From figure 4.7, large event location discrepancies can be observed. It is important to point out that the ISC data is based on data contributed by individual seismological agencies from all over the world. For Botswana, most of the ISC data is provided by the Goetz Observatory in Zimbabwe, the Council for Geoscience in South Africa and the East African Network (EAF) which comprises of stations located in Ethiopia, Kenya, Malawi, Uganda, Zambia and Zimbabwe (ISC On-line Bulletin, 2016). Only one station located near Lobatse in south-eastern Botswana is used to record data that is utilized by the ISC. This suggests that the data provided by seismological agencies can generally be unreliable due to the large distances from the source at which these recorded data are obtained. Furthermore, most of the solutions provided are based on a limited number of recordings.

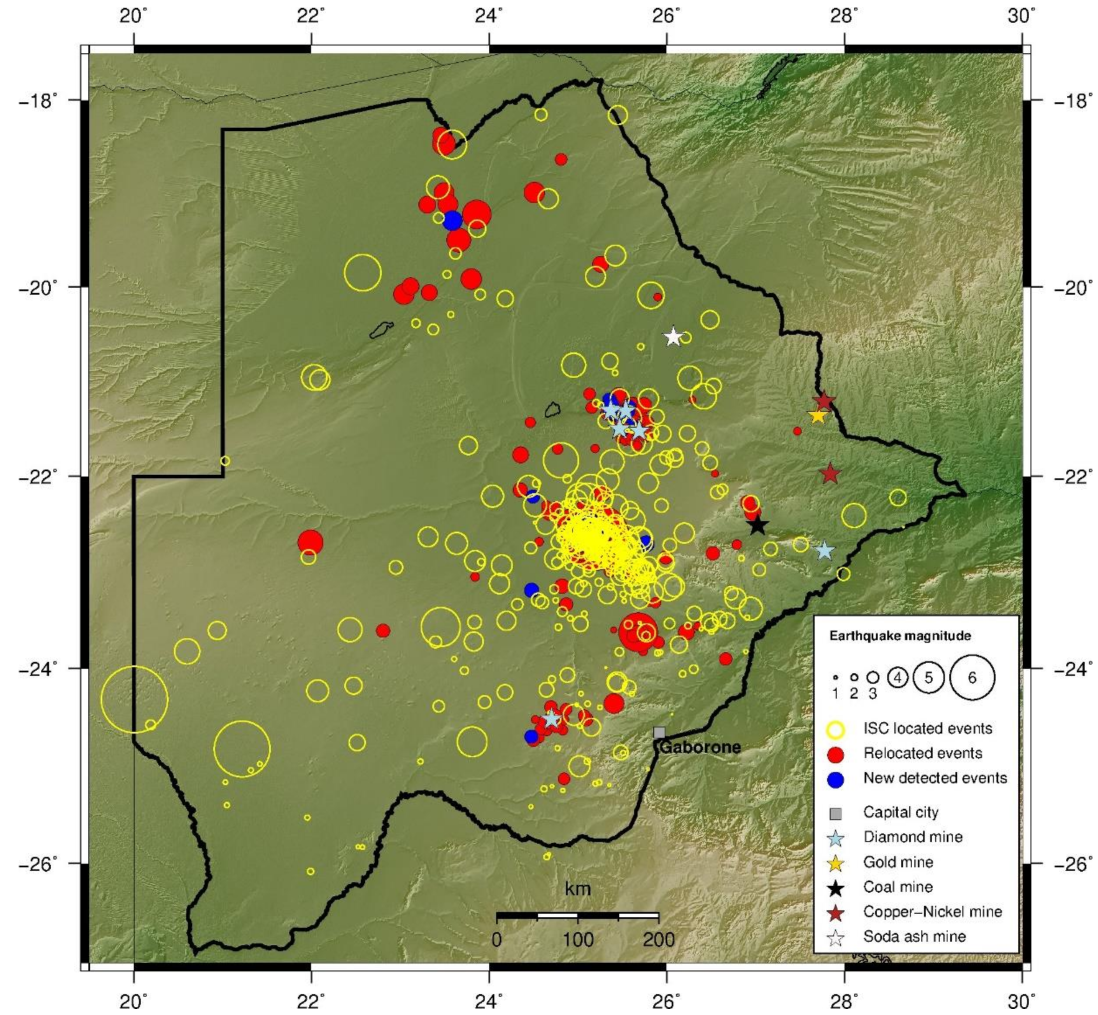

Figure 4.6. Computed epicentre locations using the NARS-Botswana data (red and blue filled circles) in comparison to the unreviewed locations provided by the ISC (yellow unfilled circles). The red circles represent events that are also documented in the ISC catalogue while the blue circles are newly detected events which the ISC did not publish. The circles' size indicates the magnitude of the events.

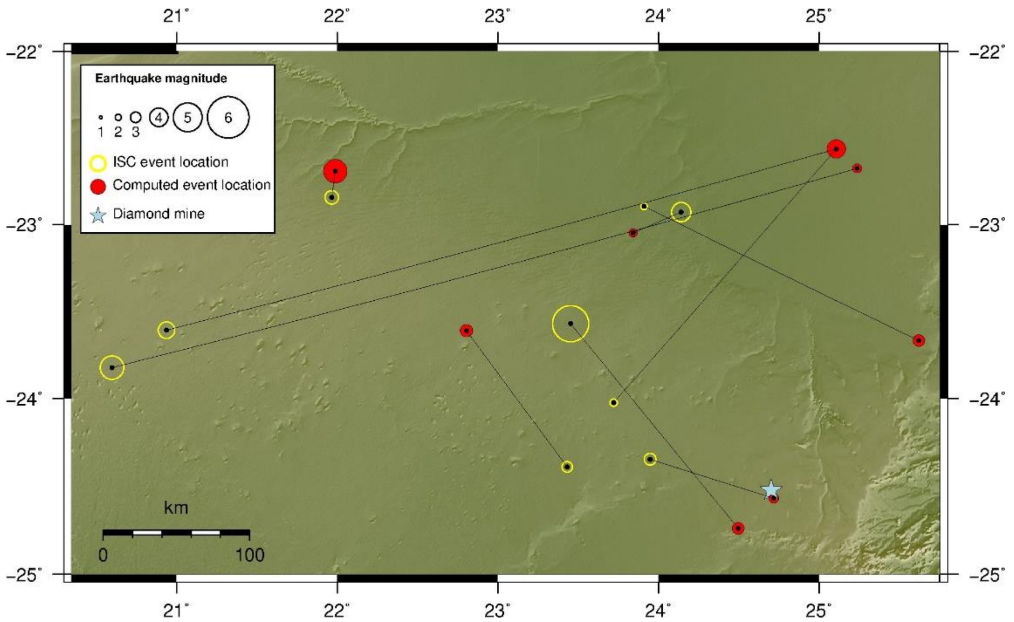

Figure 4.7. Zoomed map of the southwestern region of Botswana showing some of the ISC epicentre locations (yellow unfilled circles) connected with their SC3-computed epicentre relocations (red filled circles).

From figure 4.8, it is clear that most of the ISC unreviewed event locations for Botswana are unreliable. Besides event locations inaccuracies, 83 ISC event locations (including also duplicated events provided by different seismological agencies) were not detected when tested with SC3 using the NARS-Botswana data. Moreover, 20 ISC events were located outside of Botswana.

Unfortunately, several researchers, such as Pastier et al. (2017) and Nthaba et al. (2018), rely on the unreviewed ISC data to study the seismic activity in an area. Consequently, such studies may result in inaccurate or even false findings.

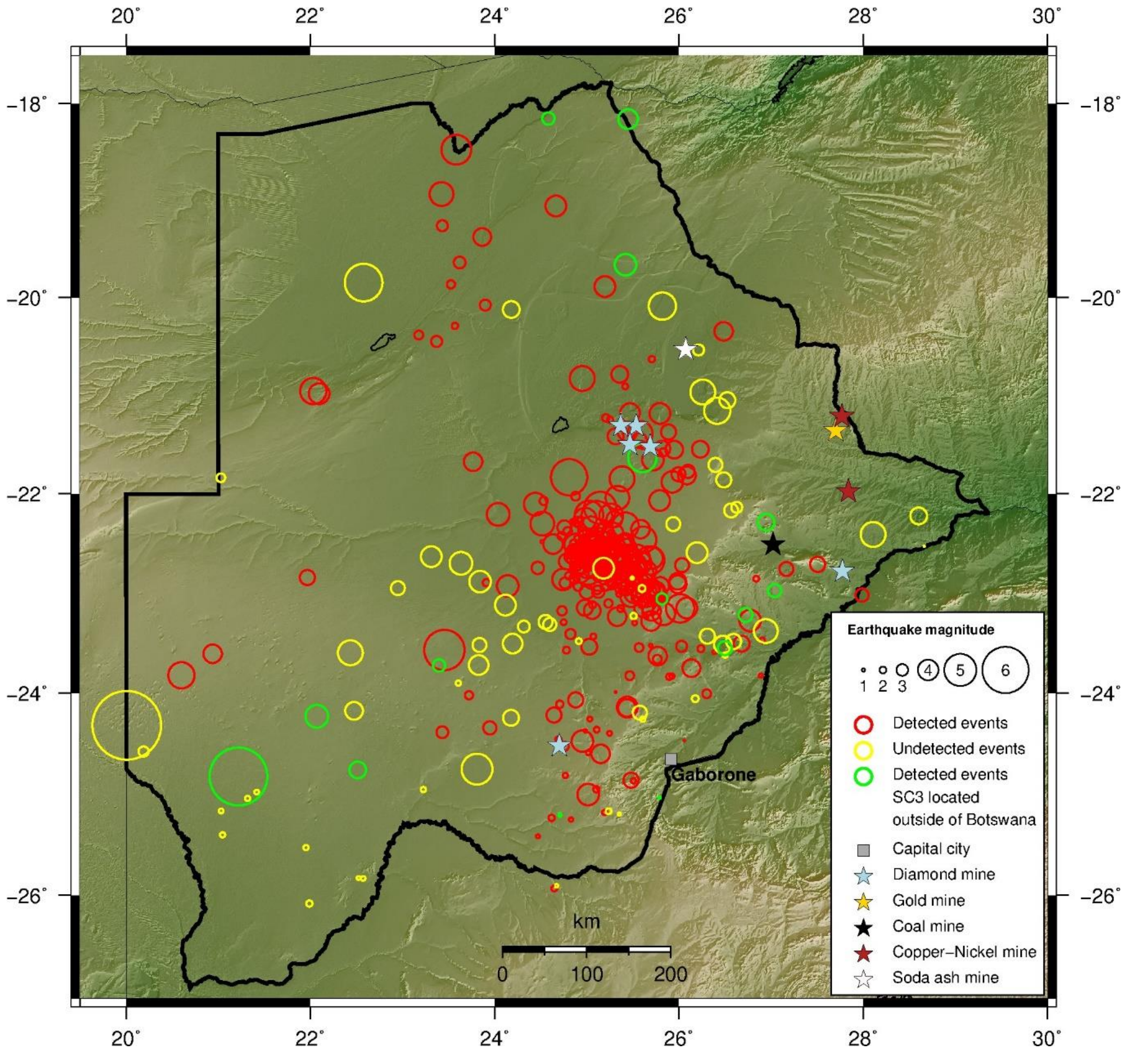

Figure 4.8. ISC event locations for the period between January 2014 and March 2018. The red circles represent the ISC events which have also been detected in this study, but have been located differently. The yellow circles indicate ISC events that have either unclear *P*-wave arrivals or no indication of an event when tested with SC3 using the NARS-Botswana data. The green circles, on the other hand, indicate those ISC events which have been reported to occur in Botswana, however, using the NARS-Botswana data these events are relocated outside of Botswana.

4.4 Botswana's seismicity in relation to the seismicity in neighbouring countries

Seismicity outside of Botswana has also been recorded by the NARS-Botswana network. During the period under study, a total of 819 seismic events have been detected and located with SC3 in and outside of Botswana (note that a less comprehensive manual event analysis was applied to seismic events detected outside of Botswana). The location and magnitude results for all detected events outside of Botswana are presented in the earthquake catalogue shown in Appendix B. Figure 4.9 shows the seismicity map of all the detected events with summary magnitude (M) ranging from 2.3 to 7.7. It can be observed that most of the events detected outside of Botswana comprise of large magnitude events which are mainly located in Botswana's neighbouring countries and along plate boundaries. The location error for events located outside the NARS-Botswana network increases notably (Appendix B). This is mainly due to the network geometry covering only the Botswana area.

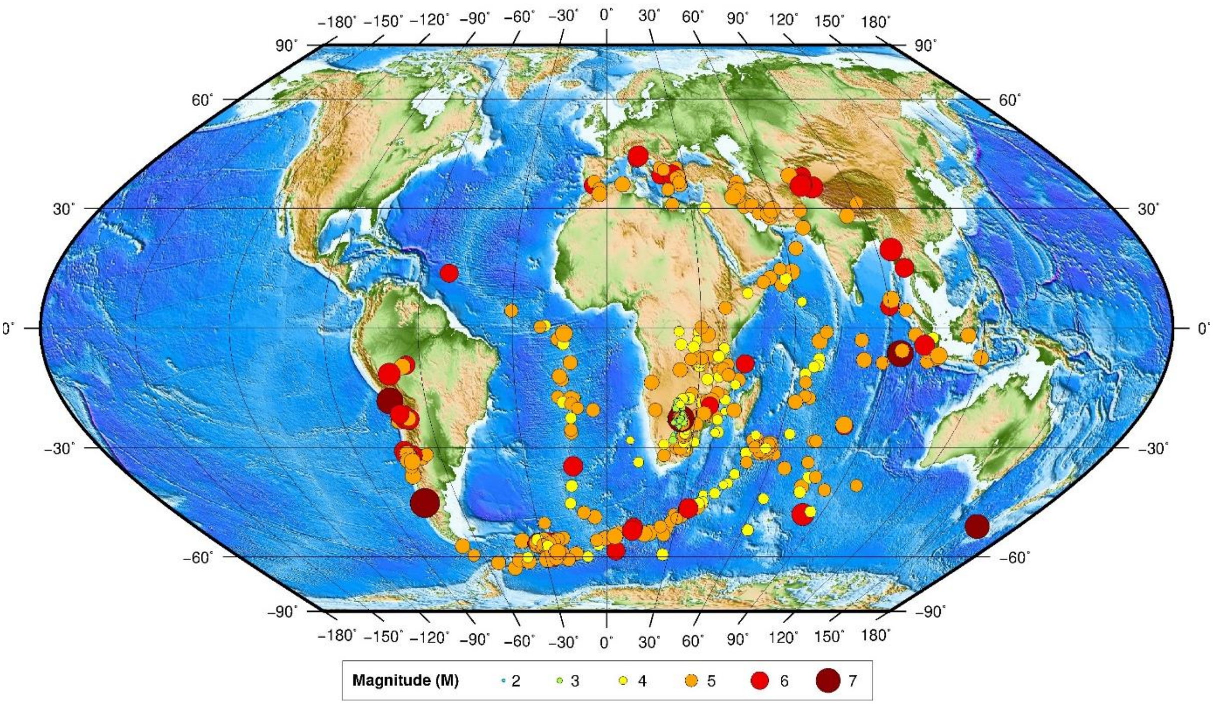

Figure 4.9. Locations of seismic events (coloured circles) that make up the global earthquake catalogue.

Figure 4.10 shows the same seismicity map as in figure 4.9 with particular focus on the southern part of Africa. From figure 4.10, it can be observed that the seismicity in South Africa and along the extension of the southwestern branch of the EARS, filled a previous unknown seismicity gap in Botswana. Thus, we suggest that the southwestern branch of the EARS is extending from the ORZ through central and south-eastern Botswana to eastern South Africa, in a NW-SE direction. This interpretation corresponds well with the suggestion made by Bird et al. (2006), Materna et al. (2019) and Fadel (2018) that central Botswana might indicate the continuing southward propagation of the EARS.

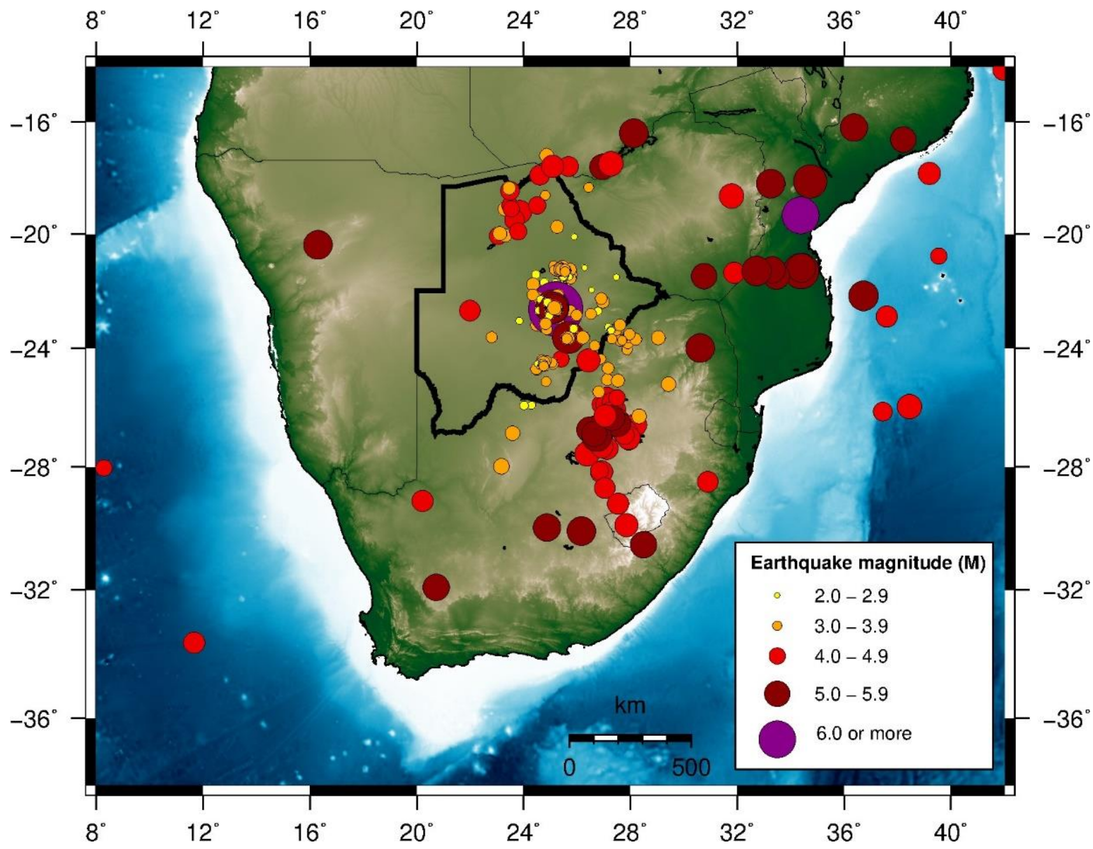

Figure 4.10. Map of southern Africa showing the locations of the detected seismic events in Botswana and neighbouring countries.

The World Stress Map 2008 (Heidbach et al., 2010) illustrates three over-coring measurements from mines in Botswana, two of which are located in the central and southern part of Botswana. These two measurements show that their maximum horizontal stresses are well aligned with the stress field needed to trigger the 2017 Moiyabana earthquake. Furthermore, another over-coring measurement in the World Stress Map 2008 (Heidbach et al., 2010), located at the border between south-eastern Botswana and northern South Africa is also consistent with the maximum horizontal stress orientations of the two over-coring measurements in Botswana. This is in agreement with the possible NW-SE trending seismicity zone observed through Botswana and the eastern part of South Africa (figure 4.10). Unfortunately, these stress measurements have been down-graded and removed in the World Stress Map 2016 (Heidbach et al., 2018) due to the major errors in over-coring measurements and difficulties in verifying the details of the measurement process (Materna et al., 2019). A general east-west tension in Botswana is also observed in deviatoric stress models of Africa (Stamps et al., 2014). This further corresponds with the extensional fault movement of the normal faulting events within central and south-eastern Botswana (Bouwman, 2019). However, to provide a better understanding of the stresses and associated deformation in Botswana and neighbouring countries, further research on the stress state is required.

5. Conclusion

A reliable assessment of the seismicity throughout Botswana has been carried out using data recorded by the NARS-Botswana seismic network between January 1st, 2014 and March 1st, 2018. A total of 376 seismic events have been detected and located in Botswana using SeisComP3 software package. The hypocenter, origin time and magnitude of each detected event in Botswana have been reported in an earthquake catalogue.

Botswana can be generally regarded as a country of low seismic activity. Moderate to large seismic events have been mainly located in the Okavango Rift Zone (ORZ) and central Botswana. During the period under study, the largest event recorded in Botswana was the April 3rd, 2017 Moiyabana earthquake, located near the tectonic boundary between the Kaapvaal Craton and the Limpopo Belt. The 2017 Moiyabana earthquake seems to be preceded by two low magnitude (fore)shocks which occurred on October 27th, 2014 and March 10th, 2015. A sequence of about 216 aftershocks followed the main event. The NW-SE strike along which the aftershocks are located is consistent with the focal mechanism of the main event and the geologically mapped strike of the Kaapvaal Craton's northern boundary. Within the ORZ, seismicity was highest along the south-eastern edge of the Okavango delta, between the Thamalakane and Tsau faults. Most of the events in the ORZ are aligned within a NNW-SSE trending seismicity zone. This zone might indicate the development of a continental rift, which could be related to the continuation of the southwestern branch of the EARS.

The clustering of seismic events in the ORZ and central Botswana appears to have filled a previously unknown seismicity gap in Southern Africa. From the identified seismic events in Botswana and neighbouring countries, it is suggested that the seismic activity observed along the 2017 Moiyabana earthquake might be connected to the seismicity observed in the ORZ and eastern South Africa. Thus, leading to the conclusion that the southwestern branch of the EARS might be extending southwards from the ORZ through central and south-eastern Botswana to eastern South Africa, in a NW-SE direction. This is indicative of the early stage of a continental breakup by rifting, which should occur gradually by the continuing southward propagation of the EARS.

The Botswana earthquake catalogue created can now be used for hazard analysis which is important for assessing the seismic risk in the country. In addition, future studies of the stress field imposed by the East African Rift System, the geology and geophysical data in Botswana may be helpful in further illuminating the seismic activity pattern in Botswana.

References

AfricaArray. (2010). *Stations and Data: Permananet Observations*. Retrieved June 15, 2019 from AfricaArray: http://africaarray.psu.edu/default.asp

Agius, M. R. (2007). *Automatic Earthquake Detection and Localisation from a three-component single-station.* M.Sc. thesis, University of Malta.

Ahmed, A., Sharma, M. L., & Sharma, A. (2007). Wavelet Based Automatic Phase Picking Algorithm for 3-Component Broadband Seismological Data. *Journal of Seismology and Earthquake Engineering, 9*(1-2), 15-24.

Akaike, H. (1971). Autoregressive model fitting for control. *Annals of the Institute of Statistical Mathematics*, *23*, 163-180.

Akaike, H. (1974). Markovian representation of stochastic process and its application to the analyses of autoregressive moving average processes. *Annals of the Institute of Statistical Mathematics*, *26,* 363-387.

Akram, J., & Eaton, D. W. (2016). A review and appraisal of arrival-time picking methods for downhole microseismic data. *GEOPHYSICS*, *81*(2), KS67-KS87.

Alabi, A., Akinyemi, O. D., & Adewale, A. (2012). Seismicity Pattern in Southern Africa from 1986 to 2009. *Earth Science Research, 2*(2). doi:10.5539/esr.v2n2p1

Albano, M., Polcari, M., Bignami, C., Moro, M., Saroli, M., & Stramondo, S. (2017). Did Anthropogenic Activities Trigger the 3 April 2017 Mw 6.5 Botswana Earthquake? *Remote Sensing*, *9*(1028). doi:10.3390/rs9101028

Allen, R. V. (1978). Automatic earthquake recognition and timing from single traces. *Bulletin of the Seismological Society of America, 65*(5), 1521-1532.

AZoMining. (2012). *Botswana: Mining, Minerals and Fuel Resources*. Retrieved June 16, 2019 from AZOMINING: https://www.azomining.com/Article.aspx?ArticleID=83

Baer, M., & Kradolfer, U. (1987). An automatic phase picker for local and teleseismic events. *Bulletin of the Seismological Society of America*, *77*(4), 1437-1445.

Begg, G. C., Griffin, W. L., Natapov, L. M., O'Reilly, S. Y., Grand, S. P., O'Neill, C. J., Hronsky, J. M. A., Djomani, Y. P., Swain, C. J., Deen, T., & Bowden, P. (2009). The lithospheric architecture of Africa: Seismic tomography, mantle petrology, and tectonic evolution. *Geosphere* , *5*(1), 23-50. doi:10.1130/GES00179.1

Benson, M. N. (2007). *The Palaeozoic Palynostratigraphy of the Karoo Supergroup and Palynofacies insight into Palaeoenvironmental interpretations, Kalahari Karoo Basin, Botswana.* Ph.D thesis, Université de Bretagne Occidentale, Brest.

Bird , P., Ben-Avraham , Z., Schubert , G., & Andreoli , M. (2006). Patterns of stress and strain rate in southern Africa. *Journal of Geophysical Research, Solid Earth, 111*(B8402), 1-14. doi:10.1029/2005JB003882

Bormann, P., & Saul , J. (2008). The New IASPEI Standard Broadband Magnitude m_B. *Seismological Research Letters, 79*(5), 698-705. doi:10.1785/gssrl.79.5.698

Bormann, P., Wendt, S., & Klinge, K. (2014). Data Analysis and Seismogram Interpretation. In P. Bormann (Ed.), *New Manual of Seismological Observatory Practice 2 (NMSOP-2)* (pp. 1-126). Potsdam: GFZ German Research Centre for Geosciences. doi:10.2312/GFZ.NMSOP-2_ch11

Bouwman, D. R. (2019). *Relocating aftershocks of the 2017 Moiyabana, Botswana earthquake.* M.Sc. thesis, Utrecht University.

Bozdogan, H. (2000). Akaike's Information Criterion and Recent Developments in Information Complexity. *Journal of Mathematical Psychology, 44*(1), 62-91. doi:10.1006/jmps.1999.1277

Bratt, S. R., & Bache, T. C. (1988). Locating events with a sparse network of regional arrays. *Bulletin of the Seismological Society of America, 78*(2), 780-798.

Bratt, S. R., & Nagy, W. (1991). *The LocSAT Program.* San Diego: Science Applications International Corporation.

Bufford, K. M., Atekwana, E. A., Abdelsalam, M. G., Shemang, E., Atekwana, E. A., Mickus, K., Moidaki, M., Modisi, M. P., & Molwalefhe, L. (2012). Geometry and faults tectonic activity of the Okavango Rift Zone, Botswana: Evidence from magnetotelluric and electrical resistivity tomography imaging. *Journal of African Earth Sciences, 65*, 61-71. doi:10.1016/j.jafrearsci.2012.01.004

Carlson, R. W., Grove, T. L., De Wit, M. J., & Gurney, J. J. (1996). Program to study crust and mantle of Archean craton in southern Africa. *Eos, Transactions American Geophysical Union, 77*(29), 273-277. doi:10.1029/96EO00194

Cessaro, R. K. (1994). Sources of Primary and Secondary Microseisms. *Bulletin of the Seismological Society of America, 84*(1), 142-148.

Columbia University. (2007). *Earthquakes and Seismology*. Retrieved June 21, 2019 from http://www.columbia.edu/~vjd1/earthquakes.htm

Corner, B., & Durrheim, R. J. (2018). An Integrated Geophysical and Geological Interpretation of the Southern African Lithosphere. In S. Siegesmund, M. A. Basei, P. Oyhantçabal, & S. Oriolo (Eds.), *Geology of Southwest Gondwana.* Cham, Switzerland: Springer International Publishing AG, part of Springer Nature. doi:10.1007/978-3-319-68920-3_2

Craig, T. J., Jackson, J. A., Priestley, K., & McKenzie, D. (2011). Earthquake distribution patterns in Africa: their relationship to variations in lithospheric and geological structure, and their rheological implications. *Geophysical Journal International*, *185*(1), 403-434. doi:10.1111/j.1365-246X.2011.04950.x

de Wit, M. J., Roering, C., Hart, R. J., Armstrong, R. A., de Ronde, C. E. J., Green , R. W. E., Tredoux, M., Peberdy, E., & Hart, R. A. (1992). Formation of an Archean continent. *Nature, 357*, 553-562.

Du Toit, A. L. (1927). The Kalahari and some of its problems. *South African Journal of Science, 24*, 88-101.

Earle, P. S., & Shearer, P. M. (1994). Characterization of Global Seismograms Using an Automatic-Picking Algorithm. *Bulletin of the Seismological Society of America, 84*(2), 366-376.

Ernst, R. E., Pereira, E., Hamilton, M. A., Pisarevsky, S. A., Rodriques, J., Tassinari, C. C. G., Teixeira, W., & Van-Dunem, V. (2013). Mesoproterozoic intraplate magmatic 'barcode' record of the Angola portion of the Congo Craton: Newly dated magmatic events at 1505 and 1110 Ma and implications for Nuna (Columbia) supercontinent reconstructions. *Precambrian Research, 230*, 103-118. doi:10.1016/j.precamres.2013.01.010

Evernden, J. F. (1969). Precision of epicenters obtained by small numbers of world-wide stations. *Bulletin of the Seismological Society of America , 59*(3), 1365-1398.

Fadel, I. E. (2018). *Crustal and upper mantle structure of Botswana: is Botswana rifting?* Ph.D thesis, University of Twente, Faculty of Geo-Information Science and Earth Observation (ITC).

Fairhead, J. D., & Girdler, R. W. (1969). How Far does the Rift System extend through Africa? *Nature, 221*(5185), 1018–1020. doi:10.1038/2211018a0

Flinn, E. A. (1965). Confidence regions and error determinations for seismic event location. *Reviews of Geophysics, 3*(1), 157-185. doi:10.1029/RG003i001p00157

Gao , S. S., Liu , K. H., Reed , C. A., Yu, Y., Massinque , B., Mdala , H., Moidaki, M., Mutamina, D., Atekwana, E. A., Ingate, S., & Reusch, A. M. (2013). Seismic arrays to study African rift initiation. *Eos, Transactions American Geophysical Union*, *94*(24), 213-214. doi:10.1002/2013EO240002

Gardonio, B., Jolivet, R., Calais, E., & Leclère, H. (2018). The April 2017 Mw6.5 Botswana Earthquake: An Intraplate. *Geophysical Research Letters, 45*. doi:10.1029/2018GL078297

GeoSci Developers. (2017). *Geophysics for Practicing Geoscientists (GPG)*. Retrieved February 20, 2019 from Filtering of Seismic Data: https://gpg.geosci.xyz/content/seismic/seismic_reflection_filtering.html

GFZ Potsdam. (2018). *SeisComP3 documentation*. Retrieved October till March, 2018-2019 from SeisComP3: https://docs.gempa.de/seiscomp3/current/

Gibson , G., & Sandiford, M. (2013). *Seismicity & induced earthquakes.* Melbourne: Melbourne Energy Institute.

Gore, J., James, D. E., Zengeni, T. G., & Gwavava, O. (2009). Crustal structure of the Zimbabwe Craton and the Limpopo Belt of Southern Africa: New constraints from seismic data and implications for its evolution. *South African Journal of Geology, 112*(3-4), 213-228. doi:10.2113/gssajg.112.3-4.213

Gutenberg , B., & Richter, C. F. (1944). Frequency of earthquakes in California. *Bulletin of the Seismological Society of America, 34*(4), 185-188.

Gwebu, T. D. (2013). Mining in Botswana. *Encyclopaedia of the History of Science, Technology, and Medicine in Non-Western Cultures*. doi:10.1007/978-94-007-3934-5_9974-1

Haddon, I. G. (2005). *The sub-Kalahari geology and tectonic evolution of the Kalahari Basin, Southern Africa.* Ph.D thesis, Faculty of Science, University of the Witwatersrand, Johannesburg.

Hanka, W., Saul, J., Weber, B., Becker, J., Harjadi, P., Fauzi, & GITEWS Seismology Group. (2010). Real-time earthquake monitoring for tsunami warning in the Indian Ocean and beyond. *Natural hazards and earth system sciences, 10*(12), 2611-2622. doi:10.5194/nhess-10-2611-2010

Havskov, J., Bormann, P., & Schweitzer, J. (2011). Seismic source location. In P. Bormann (Ed.), *New Manual of Seismological Observatory Practice 2 (NMSOP-2).* Potsdam: GFZ German Research Centre for Geosciences. doi:10.2312/GFZ. NMSOP-2_IS_11.1

Heidbach, O., Rajabi, M., Cui, X., Fuchs, K., Müller, B., Reinecker, J., Reiter, K., Tingay, M., Wenzel, F., Xie, F., Ziegler, M. O., Zoback, M. L., & Zoback, M. (2018). The World Stress Map database release 2016: Crustal stress pattern across. *Tectonophysics, 744,* 484-498. doi:10.1016/j.tecto.2018.07.007

Heidbach, O., Tingay, M., Barth, A., Reinecker, J., Kurfeß, D., & Müller, B. (2010). Global crustal stress pattern based on the World Stress Map database release 2008. *Tectonophysics, 482*(1-4), 3-15. doi:10.1016/j.tecto.2009.07.023

Hoffe, B. H. (1996). *Deep Seismic Evidence of Late Middle Proterozoic Rifting Beneath the Kalahari, Western Botswana.* M.Sc. thesis, Department of Earth Sciences Memorial University of Newfoundland.

Husen, S., & Hardebeck, J. L. (2010). Earthquake Location Accuracy. *Community Online Resource for Statistical Seismicity Analysis*. doi:10.5078/corssa-55815573

IRIS EMC. (2012). *Data Services Products: EMC-iasp91 P & S velocity reference Earth model*. Retrieved June 22, 2019 from http://ds.iris.edu/spud/earthmodel/9991809#

ISC On-line Bulletin. (2016). *International Seismological Centre*. Retrieved September - February, 2018-2019 from http://www.isc.ac.uk/

James, D., & Fouch, M. (2002). Formation and evolution of Archaean Cratons: insights from southern Africa. *Geological Society of London, 199*, 1-26. doi:10.1144/GSL.SP.2002.199.01.01

Jelsma, H. A., & Dirks, P. H. (2002). Neoarchaean tectonic evolution of the Zimbabwe Craton. *Geological Society, London, Special Publications, 199*, 183-211. doi:10.1144/GSL.SP.2002.199.01.10

Jiang, W., Yu, H., Huang, L., & Huang, L. (2012). A Robust Algorithm for Earthquake Detector. *15th World Conference on Earthquake Engineering (15WCEE), 8*.

Jordan, T. H., & Sverdrup, K. A. (1981). Teleseismic location techniques and their application to earthquake clusters in the South-Central Pacific. *Bulletin of the Seismological Society of America, 71*(4), 1105-1130.

Kennett, B. L., & Engdahl , E. R. (1991). Travel times for global earthquake location and phase association. *Geophysical Journal International, 105*, 429-465.

Key, R. M., & Ayres, N. (2000). The 1998 edition of the National Geological Map of Botswana. *Journal of African Earth Sciences, 30*(3), 427-451. doi:10.1016/S0899-5362(00)00030-0

Kinabo, B. D., Atekwana, E. A., Hogan, J. P., Modisi, M. P., Wheaton, D. D., & Kampunzu, A. B. (2007). Early structural development of the Okavango rift zone, NW Botswana. *Journal of African Earth Sciences, 48*(2-3), 125-136. doi:10.1016/j.jafrearsci.2007.02.005

Kinabo, B. D., Hogan, J. P., Atekwana, E. A., Abdelsalam, M. G., & Modisi, M. P. (2008). Fault growth and propagation during incipient continental rifting: Insights from a combined aeromagnetic and Shuttle Radar Topography Mission digital elevation model investigation of the Okavango Rift Zone, northwest Botswana. *Tectonics, 27*(3). doi:10.1029/2007TC002154

KnowBotswana. (2010). *Mining in Botswana*. Retrieved June 16, 2019 from KnowBotswana.com: http://www.knowbotswana.com/mining-in-botswana.html

Kolawole, F., Atekwana, E. A., Malloy, S., Stamps, D. S., Grandin, R., Abdelsalam, M. G., Leseane, K., & Shemang, E. M. (2017). Aeromagnetic, gravity, and Differential Interferometric Synthetic Aperture Radar analyses reveal the causative fault of the 3 April 2017 Mw 6.5 Moiyabana, Botswana, earthquake. *Geophysical Research Letters, 44*(17). doi:10.1002/2017GL074620

Küperkoch, L., Meier, T., & Diehl, T. (2011). Automated Event and Phase Identification. In P. Bormann (Ed.), *New Manual of Seismological Observatory Practice (NMSOP-2), IASPEI*, (pp. 1-52). Potsdam: GFZ German Research Centre for Geosciences. doi:10.2312/GFZ.NMSOP-2_ch16

Küperkoch, L., Meier, T., Friederich, W., & EGELADOS working group. (2010). Automated determination of P-phase arrival times at regional and local distances using higher order statistics. *Geophysical Journal International, 181*(2), 1159-1170. doi:10.1111/j.1365-246X.2010.04570.x

Kurz, J. H., Grosse, C. U., & Reinhardt, H.-W. (2005). Strategies for reliable automatic onset time picking of acoustic emissions and of ultrasound signals in concrete. *Ultrasonics, 43*(7), 538-546. doi:10.1016/j.ultras.2004.12.005

Kwadib, M. T., & Ntibinyane, O. (1993). *Seismicity of Botswana for the period 1950 - 2014.* 35th International Geological Congress Abstract.

Leseane, K., Atekwana, E. A., Mickus, K. L., Abdelsalam, M. G., Shemang, E. M., & Atekwana, E. A. (2015). Thermal perturbations beneath the incipient Okavango Rift Zone, northwest Botswana. *Journal of Geophysical Research: Solid Earth, 120*, 1210-1228. doi:10.1002/2014JB011029

Li, K. L. (2017). Location and Relocation of Seismic Sources. *Digital Comprehensive Summaries of Uppsala Dissertations from the Faculty of Science and Technology 1532*, Uppsala: Acta Universitatis Upsaliensis. ISBN 978-91-513-0013-9.

Lucara Diamond. (2019). *Karowe Mine*. Retrieved February 4, 2019 from LUCARA DIAMOND: https://www.lucaradiamond.com/operations/karowe-mine/

Maeda, N. (1985). A Method for Reading and Checking Phase Time in Auto-Processing System of Seismic Wave Data. *Zisin (Journal of the Seismological Society of Japan), 38*(3), 365-379.

Materna, K., Wei, S., Wang, X., Heng, L., Wang, T., Chen, W., Salman, R., & Bürgmann, R. (2019). Source characteristics of the 2017 Mw6.4 Moijabana, Botswana earthquake, a rare lower-crustal event within an ancient zone of weakness. *Earth and Planetary Science Letters, 506*, 348-359. doi:10.1016/j.epsl.2018.11.007

McCourt, S., Armstrong, R. A., Jelsma, H., & Mapeo, R. B. (2013). New U-Pb SHRIMP ages from the Lubango region, SW Angola: Insights into the Palaeoproterozoic evolution of the Angolan Shield, southern Congo Craton, Africa. *Journal of the Geological Society, London, 170*, 353-363. doi:10.1144/jgs2012-059.

McCourt, S., Kampunzu, A. B., Bagai, Z., & Armstrong, R. A. (2004). The crustal architecture of Archaean terranes in Northeastern Botswana. *South African Journal of Geology, 107*, 147-158. doi:10.2113/107.1-2.147

Meneghini, F., Fagereng, Å., & Kisters, A. (2017). The Matchless Amphibolite of the Damara belt, Namibia: unique preservation of a late Neoproterozoic ophiolitic suture. *Ofioliti, 42*(2), 129-145. doi:10.4454/ofioliti.v42i2.488

Midzi, V., Saunders, I., Manzunzu, B., Kwadiba, M., Jele, V., Mantsha, R., Marimira, K. T., Mulabisana, T. F., Ntibinyane, O., Pule, T., Rathod, G. W., Sitali, M., Tabane, L., van Aswegen, G., & Zulu, B. (2018). The 03 April 2017 Botswana M6.5 earthquake: Preliminary results. *Journal of African Earth Sciences, 143*, 187-194. doi:10.1016/j.jafrearsci.2018.03.027

Modie, B. N. (2000). Geology and mineralisation in the Meso- to Neoproterozoic Ghanzi-Chobe Belt of northwest Botswana. *Journal of African Earth Sciences, 30*, 467-474. doi:10.1016/S0899-5362(00)00032-4

Modisi, M. P., Atekwana, E. A., Kampunzu , A. B., & Ngwisanyi, T. H. (2000). Rift kinematics during the incipient stages of continental extension: Evidence from the nascent Okavango rift basin, northwest Botswana. *Geology, 28*(10), 939-942. doi:10.1130/0091-7613(2000)28<939:RKDTIS>2.0.CO;2

Mooney , W. D., Ritsema, J., & Hwang, Y. K. (2012). Crustal seismicity and the earthquake catalog maximum moment magnitude (M_{cmax}) in stable continental regions (SCRs): correlation with the seismic velocity of the lithosphere. *Earth and Planetary Science Letters, 357-358*, 78-83. doi:10.1016/j.epsl.2012.08.032

Moorkamp, M., Fishwick, S., Walker, R. J., & Jones, A. G. (2019). Geophysical evidence for crustal and mantle weak zones controlling intra-plate seismicity – the 2017 Botswana earthquake sequence. *Earth and Planetary Science Letters, 506*, 175-183. doi:10.1016/j.epsl.2018.10.048

Mulabisana, T. F. (2016). *Compiling a homogeneous Earthquake Catalogue for Southern Africa.* M. Sc thesis, Faculty of Science, University of Witwatersrand, Johannesburg.

Munro, K. (2004). Automatic event detection and picking of P-wave arrivals. *CREWES Research Report, 16*.

Nascimento, D. B., Schmitt, R. S., Ribeiro, A., Trouw, R. A., Passchier, C. W., & Basei, M. A. (2017). Depositional ages and provenance of the Neoproterozoic Damara Supergroup (northwest Namibia): Implications for the Angola-Congo and Kalahari cratons connection. *Gondwana Research, 52*, 153-171. doi:10.1016/j.gr.2017.09.006

Nthaba, B., Simon, R. E., & Ogubazghi, G. M. (2018). Seismicity Study of Botswana from 1966 to 2012. *International Journal of Geosciences, 9*, 707-718. doi:10.4236/ijg.2018.912043

Olivieri , M., & Clinton, J. (2012). An Almost Fair Comparison Between Earthworm and SeisComp3. *Seismological Research Letters, 83*(4). doi:10.1785/0220110111

Oriolo, S., & Becker, T. (2018). The Kalahari Craton, Southern Africa: From Archean Crustal Evolution to Gondwana Amalgamation. In S. Siegesmund, M. A. Basei, P. Oyhantçabal, & S. Oriolo, *Geology of Southwest* (pp. 133-159). Cham: Springer International Publishing AG, part of Springer Nature. doi:10.1007/978-3-319-68920-3

Pastier, A. M., Dauteuil, O., Hudson, M. M., Moreau, F., Walpersdorf, A., & Makati, K. (2017). Is the Okavango Delta the terminus of the East African Rift System? Towards a new geodynamic model: Geodetic study and geophysical review. *Tectonophysics, 712-713*, 469-481. doi:10.1016/j.tecto.2017.05.035

Pesaresi, D. (2011). The EGU2010 SM1.3 Seismic Centers Data Acquisition session: an introduction to Antelope, EarthWorm and SeisComP, and their use around the World. *Annals of Geophysics, 54*(4). doi:10.4401/ag-4972

Piersol, A. G. (2006). Chapter 3 - Data Analysis. In I. L. Ver, & L. L. Beranek, *Noise and Vibration Control Engineering - Principles and Applications* (2nd ed., pp. 43 - 70). Hoboken, New Jersey: John Wiley & Sons Inc.

Pilz, M., & Parolai, S. (2012). Tapering of windowed time series. In P. Bormann (Ed.), *New Manual of Seismological Observatory Practice 2 (NMSOP-2)* (pp. 1 - 4). Potsdam: GFZ German Research Centre for Geosciences. doi:10.2312/GFZ.NMSOP-2_IS_14.1

Pouliquen, G., Key, R. M., & Walker, A. (2008). The internal structure and geotectonic setting of the Xade and Tsetseng complexes in the westernmost part of the Kaapvaal Craton. *South African Journal of Geology, 111*(4), 345-356. doi:10.2113/gssajg.111.4.345

Ranganai, R. T., Kampunzu, A. B., Atekwana, E. A., Paya, B. K., King, J. G., Koosimile, D. I., & Stettler, E. H. (2002). Gravity evidence for a larger Limpopo Belt in southern Africa and geodynamic implications. *Geophysical Journal International*, *149*(3), F9-F14. doi:10.1046/j.1365-246X.2002.01703.x

Rankin, W. (2015). *Cross-border correlation of the Damara Belt in Namibia and equivalent lithologies in northwestern Botswana from potential field and magnetotelluric interpretations.* M.Sc thesis, School of Geosciences, University of the Witwatersrand, Johannesburg.

Reeves, C. (1972). Earthquakes in Ngamiland. *Botswana Notes and Records, 4*, 257-261.

Reeves, C. V. (1978). *Reconnaissance Aeromagnetic Survey of Botswana 1975-1977: Final Interpretation Report.* Terra Surveys Ltd, Botswana Geological Survey Department.

Richards-Dinger, K. B., & Shearer, P. M. (2000). Earthquake locations in southern California obtained using source-specific station terms. *Journal of Geophysical Research: Solid Earth, 105*(B5), 10939-10960. doi:10.1029/2000JB900014

Richter, C. F. (1935). An Instrumental Earthquake Magnitude Scale. *Bulletin of the Seismological Society of America, 25*(1), 1-32.

Schlüter, T. (2006). Botswana. In T. Schlüter, *Geological Atlas of Africa: with Notes on Stratigraphy, Tectonics, Economic Geology*, (pp. 46-49). Germany: Springer-Verlag Berlin Heidelberg.

Scholz , C. H., Koczynski , T. A., & Hutchins, D. G. (1976). Evidence for incipient rifting in Southern Africa. *Geophysical Journal of the Royal Astronomical Society, 44*(1), 135-144. doi:10.1111/j.1365-246X.1976.tb00278.x

Schorlemmer, D., Euchner, F., Kästli, P., Saul, J., & QuakeML Working Group. (2011). QuakeML: status of the XML-based seismological data exchange format. *Annals of Geophysics*, *54*(1). doi:10.4401/ag-4874

Schweitzer, J., Fyen, J., Mykkeltveit, S., Gibbons, S. J., Pirli, M., Kühn, D., & Kværna, T. (2012). Seismic Arrays. In P. Bormann (Ed.), *New Manual of Seismological Observatory Practice 2 (NMSOP-2)*, *IASPEI*. Potsdam: GFZ German Research Centre for Geosciences. doi:10.2312/GFZ.NMSOP-2_ch9

Seismology group, Utrecht University. (2015). *NARS-Botswana*. Retrieved October 22, 2019 from Network of Autonomously Recording Seismographs (NARS): http://www.geo.uu.nl/Research/Seismology/nars.html

Shearer, P. (1997). Improving local earthquake locations using the L1 norm and waveform cross correlation: Application to the Whittier Narrows California, aftershock sequence. *Journal of Geophysical Research: Solid Earth, 102*(B4), 8269-8283. doi:10.1029/96JB03228

Shearer, P. M. (2009). *Introduction to Seismology* (2nd ed.). New York: Cambridge University Press.

Shemang, E. M., & Molwalefhe, L. N. (2011). Geomorphic Landforms and Tectonism Along the Eastern Margin of the Okavango Rift Zone, North Western Botswana as Deduced From Geophysical Data in the Area. In E. Sharkov, *New Frontiers in Tectonic Research - General Problems, Sedimentary Basins and Island Arcs* (pp. 2970-3304). Rijeka: InTechOpen. doi:10.5772/18863

Simon, R. E., Kwadiba, M. T., King, J. G., & Moidaki, M. (2012). A History of Botswana's Seismic Network. *Botswana Notes and Records, 44*, 184-192.

Sleeman, R., & van Eck, T. (1999). Robust automatic P-phase picking: an on-line implementation in the analysis of broadband seismogram recordings. *Physics of the Earth and Planetary Interiors, 113*(1-4), 265-275. doi:10.1016/S0031-9201(99)00007-2

Stamps , D. S., Flesch , L. M., Calais , E., & Ghosh, A. (2014). Current kinematics and dynamics of Africa and the East African Rift System. *Journal of Geophysical Research: Solid Earth, 119*, 5161-5186. doi:10.1002/2013JB010717

Stein, S., & Wysession, M. (2003). *An Introduction to Seismology, Earthquakes, and Earth Structure*. Blackwell Publishing.

St-Onge, A. (2011). Akaike Information Criterion Applied to Detecting First Arrival Times on Microseismic Data. *Recovery – 2011 CSPG CSEG CWLS Convention*. doi:10.1190/1.3627522

Thomas, R. J., von Veh, M. W., & McCourt, S. (1993). The tectonic evolution of southern Africa: an overview. *Journal of African Earth Sciences, 16*(1-2), 5-24. doi:10.1016/0899-5362(93)90159-N

Tinker, J. H., de Wit, M. J., & Royden, L. H. (2004). Old, strong continental lithosphere with weak Archaean margin at ~1.8 Ga, Kaapvaal Craton, South Africa. *South African Journal of Geology, 107*(1-2), 255 - 260. doi:10.2113/107.1-2.255

Trnkoczy, A. (2012). Understanding and parameter setting of STA/LTA trigger algorithm. In P. Bormann (Ed.), *New Manual of Seismological Observatory Practice 2 (NMSOP-2), IASPEI* (pp. 1-20). Potsdam: GFZ German Research Centre for Geosciences. doi:10.2312/GFZ.NMSOP-2_IS_8.1

Tsuboi, S., Abe, K., Takano, K., & Yamanaka, Y. (1995). Rapid Determination of M_w from Broadband P Waveforms. *Bulletin of the Seismological Society of America, 85*(2), 606-613.

U.S. Geological Survey. (2019). *Station GT LBTB*. Retrieved June 16, 2019 from https://earthquake.usgs.gov/monitoring/operations/stations/GT/LBTB/

University of Washington School of Oceanography. (2014). *ESS 522*. From Practical Aspects of Filtering: https://www.ocean.washington.edu/courses/ess522/lectures/10_filtering.pdf

Unsworth , M., & Bedrosian, P. A. (2004). Electrical resistivity structure at the SAFOD site from magnetotelluric exploration. *Geophysical Research Letters, 31*(12). doi:10.1029/2003GL019405

Unsworth , M., Egbert , G., & Booker, J. (1999). High-resolution electromagnetic imaging of the San Andreas Fault in central California. *Journal of Geophysical Research, Solid Earth, 104*(B1), 1131-1150. doi:10.1029/98JB01755

Vaezi, Y., & van der Baan, M. (2015). Comparison of the STA/LTA and power spectral density methods for microseismic event detection. *Geophysical Journal International, 203*(3), 1896-1908.

Van Reenen, D. D., Barton, J. M., Roering, C. A., Smith, J. F., & Van Schalkwyk, J. F. (1987). Deep crystal response to continental collision: The Limpopo belt of southern Africa. *Geology, 15*(1), 11-14. doi:10.1130/0091-7613(1987)15<11:DCRTCC>2.0.CO;2

van Schijndel, V. (2013). *Precambrian Crustal Evolution of the Rehoboth Province, Southern Africa*. Ph.D. thesis, University of Gothenburg Department of Earth sciences Gothenburg, Sweden.

van Schijndel, V., Cornell, D. H., Frei, D., Simonsen, S. L., & Whitehouse, M. J. (2014). Crustal evolution of the Rehoboth Province from Archaean to Mesoproterozoic times: Insights from the Rehoboth Basement Inlier. *Precambrian Research, 240*, 22-36. doi:10.1016/j.precamres.2013.10.014

van Schijndel, V., Cornell, D. H., Hoffmann, K. H., & Frei, D. (2011). Three episodes of crustal development in the Rehoboth Province, Namibia. *Geological Society, London, Special Publications, 357*, 27-47. doi:10.1144/SP357.3

Veith, K. F., & Clawson, G. E. (1972). Magnitude from short-period P-wave data. *Bulletin of the Seismological Society of America*, *62*(2), 435-452.

Weber, B., Becker, J., Hanka, W., Heinloo, A., Hoffmann, M., Kraft, T., Pahlke, D., Reinhardt, J., & Thoms , H. (2007). SeisComP3 - automatic and interactive real time data processing. *Geophysical Research Abstracts, 9*(09219).

Weber, B., Rößler, D., & Becker, J. (2017). *Introduction to the key features of SeisComP3 [Tarining workshop Presentation slides]*. Gempa. From http://ds.iris.edu/ds/workshops/2017/10/training-workshop-in-baku-azerbaijan/presentations/

Whitmore, P. M., Tsuboi, S., Hirshorn, B., & Sokolowski, T. J. (2002). Magnitude-dependent correction for MWP. *The International Journal of The Tsunami Society, 20*(4), 187-192.

Wright, J. A., & Hall, J. (1990). Deep seismic profiling in the Nosop Basin, Botswana: cratons, mobile belts and sedimentary basins. *Tectonophysics, 173*(1-4), 333 - 343. doi:10.1016/0040-1951(90)90228-Z

Yang , Z., & Chen, W. P. (2010). Earthquakes along the East African Rift System: A multiscale, system-wide perspective. *Journal of Geophysical Research, Solid Earth, 115*(B12309), 1-31. doi:10.1029/2009JB006779

Zhang, H., Thurber, C., & Rowe, C. (2003). Automatic P-Wave Arrival Detection and Picking with Multiscale Wavelet Analysis for Single-Component Recordings. *Bulletin of the Seismological Society of America, 93*(5), 1904-1912. doi:10.1785/0120020241

Appendix A

Table A. Botswana event catalogue for seismic events detected during the period between January 1st, 2014 and March 1st 2018. Events with a fixed depth are marked with a *.

EventID	Date	Origin time (UTC)	Latitude (°) ± error	Longitude (°) ± error	Depth (km) ± error	Summary Magnitude (M)	No. of stations
gfz2014bfvc	2014-01-18	09:52:30	-18.992 ± 76.387	24.509 ± 16.441	10.0*	4.1	4
gfz2014ddlw	2014-02-14	14:00:24	-24.565 ± 5.978	24.694 ± 5.071	10.0*	2.9	4
gfz2014dxlb	2014-02-25	12:19:44	-23.319 ± 5.243	25.873 ± 10.659	16.349 ± 5.320	2.9	7
gfz2014eppt	2014-03-07	11:08:00	-19.757 ± 27.179	25.255 ± 7.517	10.0*	3.6	6
gfz2014fpnl	2014-03-21	15:30:05	-21.339 ± 5.688	25.555 ± 8.042	10.0*	3.1	6
gfz2014gccz	2014-03-28	12:59:41	-24.528 ± 5.578	24.519 ± 20.270	30.971 ± 35.311	2.5	4
gfz2014gdhk	2014-03-29	04:21:59	-23.668 ± 8.696	25.621 ± 7.745	9.302 ± 5.536	3.2	6
gfz2014gzyb	2014-04-10	13:46:39	-23.611 ± 8.919	22.805 ± 5.675	10.0*	3.3	5
gfz2014kupy	2014-06-03	14:08:23	-24.569 ± 5.954	24.718 ± 5.111	10.0*	2.9	4
gfz2014mogb	2014-06-28	13:23:29	-24.638 ± 5.605	24.830 ± 5.818	6.315 ± 10.025	2.8	4
gfz2014nker	2014-07-10	13:40:47	-24.587 ± 5.508	24.704 ± 4.942	10.0*	3	5
gfz2014opjy	2014-07-27	15:34:12	-24.558 ± 5.049	24.732 ± 4.794	10.0*	3.2	6
gfz2014sylg	2014-09-27	12:35:28	-24.534 ± 5.820	24.718 ± 4.942	10.0*	2.9	5
gfz2014tghx	2014-10-01	19:59:19	-23.049 ± 9.574	23.842 ± 5.082	8.255 ± 28.117	2.7	4
gfz2014tque	2014-10-07	13:32:56	-24.577 ± 5.963	24.682 ± 5.060	10.0*	2.7	4
gfz2014udrz	2014-10-14	15:12:31	-24.603 ± 4.957	24.758 ± 5.098	10.0*	3.1	5
gfz2014vbum	2014-10-27	19:43:41	-22.401 ± 16.186	24.890 ± 8.311	10.0*	2.9	4
gfz2015cgnd	2015-02-02	00:31:26	-18.993 ± 42.068	23.492 ± 7.659	10.0*	4	6
gfz2015dyah	2015-02-25	20:01:07	-20.059 ± 45.766	23.325 ± 10.230	10.0*	3.6	4
gfz2015emep	2015-03-05	14:06:31	-21.294 ± 34.158	25.702 ± 25.163	10.0*	3.5	5
gfz2015evme	2015-03-10	16:09:01	-22.305 ± 15.789	25.038 ± 8.813	10.0*	2.6	4
gfz2015ifac	2015-04-27	14:01:12	-22.693 ± 4.027	21.989 ± 6.097	1.756 ± 5.325	4.5	10
gfz2015irys	2015-05-04	16:04:31	-21.145 ± 9.587	25.456 ± 9.021	103.016 ± 29.992	3.5	9
gfz2015kspu	2015-06-02	11:46:38	-23.823 ± 5.266	25.733 ± 8.854	10.0*	2.7	4
gfz2015nvhq	2015-07-16	15:40:14	-21.252 ± 7.604	25.744 ± 11.512	10.0*	3.5	6
gfz2015omvl	2015-07-26	05:58:19	-19.499 ± 9.339	23.657 ± 9.856	9.624 ± 18.770	4.4	8
gfz2015rkjm	2015-09-05	14:15:01	-21.290 ± 3.716	25.546 ± 3.391	10.0*	3.1	10

gfz2015ssel	2015-09-24	02:20:03	-22.706 ± 3.498	25.769 ± 3.647	10.0*	3.6	13
gfz2015tuoh	2015-10-09	15:07:34	-21.200 ± 3.837	25.355 ± 3.574	12.984 ± 6.631	3.4	11
gfz2015uhin	2015-10-16	14:58:54	-24.529 ± 4.250	24.832 ± 6.982	10.0*	3	7
gfz2015wdom	2015-11-12	00:31:19	-21.195 ± 4.557	26.288 ± 3.902	10.0*	2.4	6
gfz2015wpik	2015-11-18	11:05:00	-21.503 ± 4.962	25.710 ± 4.135	10.0*	2.8	7
gfz2015xfum	2015-11-27	11:21:09	-21.307 ± 3.387	25.563 ± 3.419	10.0*	3.1	10
gfz2015xjli	2015-11-29	11:16:43	-24.548 ± 4.142	24.725 ± 5.808	10.0*	2.8	7
gfz2015xltp	2015-11-30	17:42:45	-23.191 ± 3.387	24.478 ± 4.625	5.632 ± 5.947	3.4	12
gfz2015xxzz	2015-12-07	10:35:18	-21.514 ± 3.647	25.697 ± 3.979	10.0*	2.7	8
gfz2015ydor	2015-12-10	11:41:01	-21.312 ± 3.195	25.571 ± 3.416	10.0*	3.2	11
gfz2015ydti	2015-12-10	14:01:28	-21.311 ± 3.561	25.360 ± 4.039	10.0*	2.9	8
gfz2015yjdx	2015-12-13	13:03:02	-24.523 ± 4.463	25.094 ± 5.156	10.0*	3.3	8
gfz2015yqpm	2015-12-17	14:51:26	-21.363 ± 4.029	25.459 ± 4.359	5.018 ± 6.102	2.9	7
gfz2016aily	2016-01-05	15:07:16	-24.714 ± 4.251	24.561 ± 4.506	10.0*	2.9	7
gfz2016anrs	2016-01-08	11:43:03	-22.378 ± 4.622	26.967 ± 9.086	8.952 ± 12.426	3.6	7
gfz2016biyp	2016-01-20	03:03:10	-20.076 ± 3.340	23.040 ± 2.980	10.0*	4.1	13
gfz2016bjwp	2016-01-20	15:10:38	-21.518 ± 3.694	25.699 ± 3.975	10.0*	2.8	8
gfz2016blpx	2016-01-21	14:04:31	-21.355 ± 3.572	25.411 ± 4.309	10.0*	3.1	9
gfz2016cdzz	2016-01-31	15:36:06	-21.330 ± 2.582	25.341 ± 3.289	10.0*	3.5	15
gfz2016cuec	2016-02-09	11:52:13	-21.970 ± 22.172	26.543 ± 9.310	6.188 ± 20.479	2.4	4
gfz2016czvv	2016-02-12	14:30:15	-21.330 ± 2.939	25.414 ± 3.970	10.0*	3.7	12
gfz2016diwv	2016-02-17	13:14:12	-24.545 ± 4.422	24.752 ± 4.834	1.158 ± 8.725	3	6
gfz2016dtyv	2016-02-23	14:44:40	-21.350 ± 3.280	25.408 ± 5.027	10.0*	3.1	8
gfz2016dxms	2016-02-25	13:09:00	-21.502 ± 3.965	25.475 ± 5.321	10.0*	2.7	6
gfz2016evgc	2016-03-09	13:05:19	-22.715 ± 8.439	26.788 ± 6.673	10.0*	2.8	5
gfz2016fgha	2016-03-15	14:02:05	-21.409 ± 4.529	25.617 ± 4.157	10.0*	3.1	8
gfz2016fghl	2016-03-15	14:15:00	-21.324 ± 6.607	25.531 ± 9.437	10.0*	2.7	6
gfz2016fluk	2016-03-18	14:29:25	-21.457 ± 6.113	25.491 ± 9.442	3.954 ± 6.601	2.6	6
gfz2016fwwk	2016-03-24	15:59:27	-19.293 ± 5.004	23.585 ± 3.609	18.796 ± 12.516	4	11
gfz2016gemr	2016-03-28	20:10:07	-19.226 ± 4.409	23.861 ± 3.112	5.207 ± 8.747	4.8	15
gfz2016gepy	2016-03-28	21:48:47	-20.106 ± 5.839	25.898 ± 9.667	2.266 ± 9.573	2.5	4
gfz2016gqus	2016-04-04	13:51:32	-21.485 ± 6.501	25.471 ± 9.295	10.0*	2.8	5
gfz2016hfjx	2016-04-12	13:26:21	-21.585 ± 6.228	25.544 ± 9.019	3.100 ± 6.941	2.6	5
gfz2016hjbz	2016-04-14	13:58:54	-21.133 ± 11.491	25.130 ± 11.535	10.0*	3.1	5

gfz2016hwnu	2016-04-21	22:43:05	-21.525 ± 12.341	27.470 ± 34.768	8.087 ± 22.779	2.5	4
gfz2016iezy	2016-04-26	13:56:16	-21.311 ± 5.595	25.404 ± 5.601	10.0*	3.3	7
gfz2016igta	2016-04-27	12:42:18	-21.604 ± 13.267	25.474 ± 12.738	10.0*	2.7	4
gfz2016ixhe	2016-05-06	14:02:22	-21.330 ± 6.557	25.566 ± 8.093	10.0*	3.1	7
gfz2016ixmp	2016-05-06	16:47:10	-21.708 ± 6.627	25.193 ± 8.488	10.0*	2.6	5
gfz2016jglt	2016-05-11	14:34:42	-21.504 ± 6.225	25.638 ± 7.598	10.0*	2.6	5
gfz2016jivo	2016-05-12	21:48:34	-23.034 ± 4.583	25.600 ± 5.153	10.0*	3.1	7
gfz2016jlbp	2016-05-14	03:07:58	-21.713 ± 7.761	24.772 ± 7.514	10.0*	2.9	5
gfz2016jrjn	2016-05-17	13:56:42	-21.532 ± 3.343	25.632 ± 3.654	25.807 ± 7.171	3.7	12
gfz2016jtap	2016-05-18	11:42:22	-21.453 ± 6.428	25.623 ± 8.102	10.0*	2.6	5
gfz2016kclc	2016-05-23	15:13:46	-25.136 ± 4.365	24.843 ± 5.711	10.0*	3.1	6
gfz2016kcmr	2016-05-23	16:01:30	-21.627 ± 6.219	25.652 ± 7.458	10.0*	2.4	4
gfz2016kjqv	2016-05-27	14:04:44	-21.318 ± 5.078	25.405 ± 4.063	10.0*	3.2	7
gfz2016ksxf	2016-06-01	15:32:11	-21.539 ± 3.705	25.714 ± 4.018	10.0*	3.1	9
gfz2016lshm	2016-06-15	13:07:33	-21.405 ± 6.742	25.438 ± 9.716	10.0*	2.8	5
gfz2016lsje	2016-06-15	13:58:02	-24.362 ± 4.776	25.405 ± 6.911	12.210 ± 15.425	4	9
gfz2016luff	2016-06-16	14:14:40	-21.539 ± 8.748	25.696 ± 10.979	10.0*	2.7	4
gfz2016lwdu	2016-06-17	15:47:33	-19.121 ± 7.956	23.304 ± 5.159	10.0*	3.7	8
gfz2016mgzh	2016-06-23	14:01:25	-21.556 ± 4.210	25.660 ± 5.681	10.0*	2.5	6
gfz2016mtwb	2016-06-30	15:09:22	-21.210 ± 18.010	25.623 ± 13.731	10.0*	2.6	4
gfz2016mvpe	2016-07-01	13:56:54	-21.276 ± 4.771	25.156 ± 10.330	10.0*	3.1	5
gfz2016neni	2016-07-06	11:14:10	-21.513 ± 4.324	25.693 ± 5.690	10.0*	3.2	6
gfz2016nequ	2016-07-06	12:59:40	-21.677 ± 4.277	25.665 ± 5.265	5.000 ± 0.000	2.8	6
gfz2016ngoh	2016-07-07	13:59:49	-21.381 ± 4.051	25.444 ± 6.599	10.0*	2.8	6
gfz2016niic	2016-07-08	13:08:50	-21.535 ± 4.014	25.456 ± 6.594	10.0*	2.7	6
gfz2016nvcq	2016-07-15	13:08:47	-21.627 ± 4.193	25.588 ± 5.889	10.0*	2.7	6
gfz2016nxom	2016-07-16	21:24:56	-23.731 ± 6.138	25.905 ± 7.235	10.0*	3.1	6
gfz2016nxuo	2016-07-17	00:29:16	-21.439 ± 3.289	25.770 ± 3.641	5.140 ± 5.204	3.5	11
gfz2016oapc	2016-07-18	13:07:06	-21.433 ± 9.875	24.464 ± 15.175	10.0*	2.9	5
gfz2016onjj	2016-07-25	12:59:40	-21.624 ± 4.336	25.534 ± 7.000	10.0*	2.8	5
gfz2016orcc	2016-07-27	14:00:45	-21.369 ± 3.535	25.592 ± 4.005	10.0*	3.6	9
gfz2016phms	2016-08-05	13:24:24	-21.578 ± 3.648	25.555 ± 4.976	10.0*	2.8	7
gfz2016povv	2016-08-09	14:00:05	-21.234 ± 2.890	25.601 ± 4.418	10.0*	3.2	10
gfz2016pqtt	2016-08-10	15:11:00	-21.533 ± 3.485	25.717 ± 4.122	10.0*	3	9

gfz2016qdge	2016-08-17	11:05:27	-21.422 ± 6.355	25.711 ± 8.637	8.737 ± 7.545	2.5	5
gfz2016qhfs	2016-08-19	15:24:25	-21.380 ± 3.816	25.541 ± 5.044	10.0*	3	7
gfz2016qtxu	2016-08-26	14:10:14	-21.316 ± 3.277	25.380 ± 4.248	10.0*	3.2	9
gfz2016rgsb	2016-09-02	14:02:28	-21.281 ± 3.833	25.357 ± 5.143	10.0*	2.9	7
gfz2016rnua	2016-09-06	10:59:50	-21.569 ± 3.959	25.764 ± 4.615	10.0*	3.3	9
gfz2016sjyz	2016-09-18	14:29:13	-18.637 ± 5.119	24.811 ± 5.635	10.0*	3.1	4
gfz2016takb	2016-09-27	14:15:29	-21.296 ± 3.824	25.325 ± 4.292	10.0*	3.1	8
gfz2016tzyl	2016-10-11	13:56:26	-21.320 ± 3.423	25.399 ± 3.447	10.0*	3.5	11
gfz2016uskw	2016-10-21	16:38:50	-24.633 ± 4.244	24.648 ± 4.272	10.0*	3.1	8
gfz2016wess	2016-11-11	15:47:28	-21.439 ± 6.454	25.620 ± 8.181	10.0*	2.5	5
gfz2016wgfn	2016-11-12	11:23:50	-24.740 ± 4.136	24.497 ± 3.860	10.0*	3.2	9
gfz2016wtkk	2016-11-19	16:37:53	-21.774 ± 3.849	24.354 ± 3.604	4.988 ± 11.711	3.6	10
gfz2016ybvt	2016-12-08	12:58:45	-24.624 ± 4.751	24.584 ± 4.476	10.0*	3.1	7
gfz2016yhog	2016-12-11	16:00:51	-24.564 ± 5.271	24.742 ± 7.187	10.0*	2.4	4
gfz2016yqoh	2016-12-16	14:15:26	-24.703 ± 4.610	24.475 ± 4.062	10.0*	3.3	8
gfz2016yrmk	2016-12-17	02:26:41	-23.328 ± 7.837	25.808 ± 6.002	10.0*	2.3	4
gfz2016yznc	2016-12-21	11:53:10	-22.276 ± 6.832	26.909 ± 5.511	10.0*	3.4	4
gfz2016zbmz	2016-12-22	14:05:22	-21.308 ± 3.189	25.399 ± 3.464	10.0*	3.3	11
gfz2017adet	2017-01-02	17:48:39	-19.914 ± 3.238	23.798 ± 2.895	4.910 ± 7.685	4.1	17
gfz2017dhct	2017-02-16	13:57:28	-21.324 ± 3.429	25.388 ± 3.794	10.0*	3.5	9
gfz2017evia	2017-03-10	14:02:32	-21.315 ± 3.668	25.416 ± 4.607	10.0*	3.4	7
gfz2017fpiy	2017-03-21	13:14:29	-24.487 ± 5.244	25.069 ± 11.868	10.0*	3.1	4
gfz2017gnlg	2017-04-03	17:40:17	-22.636 ± 3.075	25.206 ± 3.680	20.417 ± 9.568	7.3	14
gfz2017gnlp	2017-04-03	17:50:23	-22.602 ± 4.933	25.027 ± 4.868	10.0*	5.5	8
gfz2017gnlv	2017-04-03	17:57:56	-22.662 ± 3.192	25.115 ± 3.884	10.0*	5	12
gfz2017gnmh	2017-04-03	18:11:26	-22.584 ± 3.192	25.095 ± 3.725	10.061 ± 5.607	5.1	12
gfz2017gnmp	2017-04-03	18:20:21	-22.567 ± 4.250	25.058 ± 6.650	10.0*	4.5	6
gfz2017gnne	2017-04-03	18:38:12	-22.601 ± 3.192	25.077 ± 3.754	5.834 ± 5.406	4.4	12
gfz2017gnoj	2017-04-03	19:14:57	-22.373 ± 4.581	24.686 ± 7.484	18.384 ± 14.241	3.7	6
gfz2017gnpf	2017-04-03	19:39:36	-22.628 ± 3.357	25.029 ± 3.969	1.855 ± 6.169	4	10
gfz2017gnqf	2017-04-03	20:09:50	-22.585 ± 3.392	25.071 ± 5.157	9.587 ± 5.920	4.3	10
gfz2017gnqu	2017-04-03	20:28:01	-22.562 ± 3.243	25.101 ± 3.971	12.613 ± 5.621	4.2	11
gfz2017gnrc	2017-04-03	20:37:33	-22.650 ± 4.219	25.046 ± 5.384	10.0*	3.7	7
gfz2017gnrx	2017-04-03	21:01:13	-22.577 ± 3.420	25.076 ± 3.980	10.420 ± 5.687	3.9	10

gfz2017gnso	2017-04-03	21:21:01	-22.648 ± 3.340	25.202 ± 4.014	17.549 ± 9.287	4	11
gfz2017gnuf	2017-04-03	22:11:14	-22.710 ± 4.477	25.204 ± 4.648	5.221 ± 5.907	3.5	7
gfz2017gnum	2017-04-03	22:19:40	-22.548 ± 3.232	25.083 ± 3.966	11.915 ± 5.633	3.8	11
gfz2017gnva	2017-04-03	22:36:43	-22.695 ± 5.472	25.754 ± 6.660	5.168 ± 8.701	3.3	6
gfz2017gnwj	2017-04-03	23:16:23	-22.648 ± 3.572	25.231 ± 4.058	14.677 ± 5.828	4.2	10
gfz2017gnyn	2017-04-04	00:22:26	-22.677 ± 5.464	25.237 ± 7.582	10.0*	2.8	5
gfz2017gnyo	2017-04-04	00:23:51	-22.673 ± 4.262	25.057 ± 6.651	10.0*	3.2	6
gfz2017gnzr	2017-04-04	00:57:41	-22.685 ± 4.223	25.233 ± 5.240	11.681 ± 6.231	3.4	8
gfz2017gobt	2017-04-04	02:00:00	-22.611 ± 3.675	25.085 ± 4.339	4.380 ± 6.178	3.8	9
gfz2017goea	2017-04-04	03:08:48	-22.640 ± 17.460	25.193 ± 24.549	12.342 ± 23.262	2.8	4
gfz2017goeb	2017-04-04	03:10:25	-22.676 ± 3.825	25.158 ± 4.386	4.040 ± 6.304	3.3	8
gfz2017gogi	2017-04-04	04:19:23	-22.622 ± 3.534	25.156 ± 4.036	13.801 ± 5.788	4.3	10
gfz2017goia	2017-04-04	05:09:58	-22.670 ± 6.156	25.228 ± 6.814	13.100 ± 7.568	3.4	6
gfz2017gojp	2017-04-04	05:58:11	-22.645 ± 3.924	25.101 ± 4.897	10.0*	3.5	8
gfz2017gola	2017-04-04	06:40:43	-22.702 ± 3.215	25.224 ± 3.736	8.030 ± 5.470	3.9	13
gfz2017gooe	2017-04-04	08:17:21	-22.690 ± 4.959	25.170 ± 4.914	7.288 ± 6.036	3.2	7
gfz2017gooo	2017-04-04	08:29:00	-22.580 ± 4.190	25.118 ± 4.129	9.516 ± 5.827	3.3	8
gfz2017goou	2017-04-04	08:35:10	-22.998 ± 7.622	25.359 ± 5.294	10.0*	3	5
gfz2017goqr	2017-04-04	09:32:02	-22.638 ± 3.198	25.207 ± 3.715	10.096 ± 5.508	4.1	13
gfz2017goqx	2017-04-04	09:39:48	-22.615 ± 3.411	25.098 ± 3.981	7.686 ± 5.478	4.3	11
gfz2017gozj	2017-04-04	13:56:30	-22.653 ± 3.308	25.272 ± 3.769	9.081 ± 5.587	4.1	12
gfz2017gpda	2017-04-04	15:46:34	-22.645 ± 3.494	25.238 ± 3.798	11.823 ± 5.706	4	11
gfz2017gpek	2017-04-04	16:28:46	-22.585 ± 5.174	25.071 ± 5.598	8.280 ± 6.233	3.1	6
gfz2017gphr	2017-04-04	18:07:25	-22.635 ± 3.594	25.125 ± 3.769	6.919 ± 5.520	4	10
gfz2017gpie	2017-04-04	18:23:35	-22.574 ± 12.433	25.073 ± 19.637	9.538 ± 12.608	3	5
gfz2017gpje	2017-04-04	18:53:10	-22.602 ± 3.214	25.064 ± 3.753	8.699 ± 5.551	4.8	12
gfz2017gpku	2017-04-04	19:41:59	-22.668 ± 3.328	25.214 ± 4.017	15.613 ± 9.081	4.6	11
gfz2017gpni	2017-04-04	20:59:35	-22.541 ± 4.782	25.106 ± 4.894	11.669 ± 6.488	3.5	7
gfz2017gpnz	2017-04-04	21:18:40	-22.573 ± 3.223	25.049 ± 4.504	10.486 ± 5.880	4	10
gfz2017gpox	2017-04-04	21:46:42	-22.580 ± 6.447	25.100 ± 6.614	9.056 ± 7.032	3.4	6
gfz2017gppu	2017-04-04	22:13:57	-22.645 ± 3.307	25.202 ± 4.539	14.761 ± 5.908	3.9	10
gfz2017gprj	2017-04-04	23:01:48	-22.678 ± 3.836	25.237 ± 4.827	11.420 ± 6.105	3.4	8
gfz2017gpsv	2017-04-04	23:45:36	-22.650 ± 3.382	25.180 ± 4.947	13.749 ± 5.960	3.8	9
gfz2017gpud	2017-04-05	00:25:12	-22.210 ± 5.422	24.493 ± 7.081	29.870 ± 36.786	3.3	5

gfz2017gpue	2017-04-05	00:25:41	-22.651 ± 4.202	25.158 ± 6.857	10.0*	3	5
gfz2017gpvd	2017-04-05	00:54:59	-22.583 ± 3.215	25.077 ± 4.504	9.082 ± 5.775	5.7	10
gfz2017gpve	2017-04-05	00:55:51	-22.557 ± 3.534	25.073 ± 4.584	10.466 ± 6.013	5.7	10
gfz2017gpxl	2017-04-05	02:06:29	-22.582 ± 3.739	25.090 ± 4.812	8.088 ± 5.922	3.7	8
gfz2017gpyw	2017-04-05	02:49:05	-22.689 ± 3.325	25.205 ± 4.536	14.826 ± 6.050	4.2	10
gfz2017gpzj	2017-04-05	03:04:10	-22.574 ± 4.641	25.071 ± 4.886	10.024 ± 6.346	3.3	7
gfz2017gpzp	2017-04-05	03:10:53	-22.611 ± 4.424	25.106 ± 4.793	15.962 ± 17.988	3.5	8
gfz2017gpzv	2017-04-05	03:18:12	-22.632 ± 3.689	25.097 ± 4.798	4.135 ± 6.396	3.3	8
gfz2017gqao	2017-04-05	03:40:37	-22.601 ± 3.681	25.036 ± 4.794	4.313 ± 6.475	3.6	8
gfz2017gqds	2017-04-05	05:15:24	-22.548 ± 6.169	24.953 ± 6.901	2.861 ± 7.444	3.3	5
gfz2017gqhl	2017-04-05	07:08:42	-22.561 ± 4.035	25.108 ± 4.747	6.305 ± 6.198	3.6	6
gfz2017gqol	2017-04-05	10:41:11	-22.614 ± 5.092	25.109 ± 5.124	5.088 ± 6.216	3.5	6
gfz2017gqry	2017-04-05	12:26:49	-22.568 ± 3.223	25.096 ± 4.281	10.346 ± 5.788	4.2	11
gfz2017gqxb	2017-04-05	15:02:37	-22.555 ± 3.779	25.106 ± 4.297	2.918 ± 6.567	4.2	9
gfz2017grdw	2017-04-05	18:28:57	-22.697 ± 4.078	25.328 ± 5.136	10.0*	3.1	6
gfz2017grmj	2017-04-05	22:47:02	-22.595 ± 3.307	25.073 ± 4.932	8.629 ± 5.753	4.3	9
gfz2017grqz	2017-04-06	01:05:50	-22.604 ± 3.855	25.122 ± 4.822	7.016 ± 5.914	3.4	7
gfz2017grtt	2017-04-06	02:30:21	-22.762 ± 3.104	25.044 ± 4.260	10.0*	4.4	11
gfz2017grwn	2017-04-06	03:53:54	-22.566 ± 4.574	25.073 ± 4.886	6.600 ± 6.258	3.8	7
gfz2017grzo	2017-04-06	05:26:01	-22.651 ± 3.692	25.198 ± 4.951	14.696 ± 6.157	4.2	8
gfz2017gsbe	2017-04-06	06:15:38	-22.480 ± 4.794	24.837 ± 5.354	9.458 ± 7.135	3.2	5
gfz2017gsdt	2017-04-06	07:34:02	-22.600 ± 3.092	25.131 ± 4.280	13.652 ± 5.801	5	12
gfz2017gsmd	2017-04-06	11:47:50	-22.618 ± 4.149	25.244 ± 4.353	10.572 ± 6.137	3.8	8
gfz2017gtok	2017-04-07	02:04:27	-23.147 ± 6.018	24.820 ± 6.420	12.247 ± 4.866	3.4	6
gfz2017gton	2017-04-07	02:08:19	-22.597 ± 3.216	25.066 ± 4.496	8.792 ± 5.754	4.7	10
gfz2017gtpq	2017-04-07	02:41:40	-22.646 ± 4.227	25.130 ± 6.612	4.439 ± 6.828	3.1	6
gfz2017gtrr	2017-04-07	03:43:48	-22.656 ± 4.286	25.259 ± 5.645	2.615 ± 7.435	3.3	5
gfz2017guno	2017-04-07	14:47:10	-22.540 ± 3.980	24.924 ± 4.496	5.825 ± 6.308	3.8	7
gfz2017gvad	2017-04-07	21:08:51	-22.678 ± 3.366	25.152 ± 4.935	11.038 ± 5.827	4.3	9
gfz2017gwmf	2017-04-08	16:22:22	-22.563 ± 3.445	25.086 ± 4.315	10.015 ± 5.937	3.8	10
gfz2017gwnd	2017-04-08	16:50:28	-22.644 ± 3.764	25.260 ± 4.590	8.563 ± 5.942	3.7	8
gfz2017gwom	2017-04-08	17:31:29	-22.610 ± 3.741	25.060 ± 4.475	8.336 ± 5.816	4.3	9
gfz2017gwtg	2017-04-08	19:55:33	-22.567 ± 3.090	25.087 ± 4.387	11.649 ± 5.818	5.3	11
gfz2017gxeh	2017-04-09	01:30:16	-22.666 ± 6.509	25.255 ± 6.567	10.710 ± 7.881	3.2	6

gfz2017gxpg	2017-04-09	07:03:11	-22.621 ± 3.496	25.234 ± 4.345	9.986 ± 5.845	3.8	10
gfz2017gxvd	2017-04-09	10:01:07	-22.654 ± 4.198	25.203 ± 4.795	12.939 ± 6.413	3.7	6
gfz2017gxwi	2017-04-09	10:37:00	-22.683 ± 4.838	25.290 ± 5.391	10.0*	3	5
gfz2017gyee	2017-04-09	14:34:48	-22.608 ± 4.340	25.105 ± 4.597	9.220 ± 6.155	3.5	8
gfz2017gykk	2017-04-09	17:44:02	-22.702 ± 6.428	25.314 ± 6.649	6.339 ± 8.699	3.3	5
gfz2017gzcl	2017-04-10	02:51:03	-22.598 ± 3.178	25.028 ± 4.472	3.544 ± 6.339	4.2	10
gfz2017gzcs	2017-04-10	02:59:12	-22.570 ± 3.222	25.067 ± 4.508	10.318 ± 5.841	3.9	10
gfz2017gzea	2017-04-10	03:38:56	-22.646 ± 5.074	25.214 ± 5.229	16.509 ± 10.638	3.4	6
gfz2017haji	2017-04-10	19:28:12	-22.640 ± 6.801	25.168 ± 11.050	14.160 ± 8.493	3.4	5
gfz2017hame	2017-04-10	20:54:33	-22.581 ± 3.455	25.089 ± 4.532	10.431 ± 5.942	3.8	9
gfz2017hbfm	2017-04-11	06:39:34	-22.574 ± 4.214	24.997 ± 5.607	4.552 ± 7.072	3.2	5
gfz2017hbkv	2017-04-11	09:21:55	-22.579 ± 4.574	25.016 ± 4.476	10.650 ± 6.381	3.4	7
gfz2017hckg	2017-04-11	22:11:39	-22.634 ± 4.125	25.207 ± 4.382	15.359 ± 9.858	3.7	9
gfz2017hcvc	2017-04-12	03:40:21	-22.644 ± 3.397	25.089 ± 4.277	5.687 ± 5.611	3.6	10
gfz2017heqr	2017-04-13	03:43:18	-22.634 ± 4.744	25.169 ± 4.921	10.670 ± 6.486	3.2	6
gfz2017hfel	2017-04-13	10:40:48	-22.660 ± 6.532	25.262 ± 6.569	10.268 ± 7.928	3.3	6
gfz2017hfuh	2017-04-13	18:41:21	-22.647 ± 3.537	25.205 ± 4.339	14.083 ± 5.996	3.8	10
gfz2017hhfm	2017-04-14	13:28:49	-22.611 ± 4.340	25.047 ± 4.467	1.868 ± 6.710	3.5	7
gfz2017hhke	2017-04-14	15:50:42	-22.662 ± 6.795	25.234 ± 11.168	13.010 ± 8.435	3.5	5
gfz2017hihg	2017-04-15	03:29:51	-22.694 ± 4.673	25.271 ± 5.335	5.972 ± 6.695	3.3	6
gfz2017hjxl	2017-04-16	00:48:42	-22.611 ± 4.706	25.125 ± 5.405	9.157 ± 6.635	2.9	5
gfz2017hkhc	2017-04-16	05:41:11	-22.666 ± 4.218	25.227 ± 4.930	14.519 ± 6.340	3.3	7
gfz2017hmma	2017-04-17	10:27:10	-22.846 ± 5.263	25.988 ± 4.650	10.0*	3.3	6
gfz2017hnbs	2017-04-17	18:23:11	-22.575 ± 3.870	25.077 ± 4.308	9.422 ± 6.093	3.7	9
gfz2017hnnp	2017-04-18	00:23:05	-22.568 ± 4.658	25.082 ± 4.888	9.920 ± 6.360	3.5	7
gfz2017hocb	2017-04-18	07:42:09	-22.592 ± 3.692	25.161 ± 4.298	11.335 ± 5.867	3.6	9
gfz2017hpmh	2017-04-19	01:59:44	-22.569 ± 4.528	24.993 ± 4.882	3.711 ± 6.945	3.3	6
gfz2017hqbb	2017-04-19	09:27:13	-22.605 ± 4.774	25.137 ± 4.914	11.502 ± 6.492	3.6	6
gfz2017hqfl	2017-04-19	11:40:37	-22.753 ± 5.743	25.495 ± 4.783	10.0*	3.1	5
gfz2017hqpe	2017-04-19	16:35:28	-22.560 ± 6.285	25.003 ± 6.886	6.294 ± 6.818	3	5
gfz2017hrwu	2017-04-20	09:34:16	-22.740 ± 3.987	25.376 ± 7.720	10.0*	3.5	8
gfz2017htay	2017-04-21	00:48:56	-22.596 ± 3.426	25.199 ± 4.538	9.384 ± 5.732	3.5	9
gfz2017hujw	2017-04-21	18:27:39	-22.613 ± 3.581	25.165 ± 4.930	6.632 ± 5.827	3.5	8
gfz2017humn	2017-04-21	19:47:45	-22.313 ± 4.779	24.743 ± 8.468	53.779 ± 23.319	2.8	5

gfz2017hunh	2017-04-21	20:10:32	-22.782 ± 3.981	25.214 ± 4.837	10.0*	3.1	7
gfz2017hvhq	2017-04-22	06:28:10	-22.636 ± 4.035	25.221 ± 4.563	13.521 ± 6.201	3.7	8
gfz2017hxws	2017-04-23	16:21:35	-22.616 ± 4.345	25.244 ± 5.012	8.663 ± 6.347	3.6	7
gfz2017hzdu	2017-04-24	09:04:23	-22.686 ± 3.675	25.230 ± 4.494	13.344 ± 6.031	4.2	9
gfz2017hzvg	2017-04-24	17:53:41	-22.661 ± 3.425	25.218 ± 4.964	15.672 ± 9.359	3.9	9
gfz2017idlc	2017-04-26	17:17:49	-22.577 ± 8.317	25.115 ± 5.891	28.390 ± 15.226	2.7	4
gfz2017iegv	2017-04-27	04:16:17	-22.562 ± 4.675	25.009 ± 4.892	9.057 ± 6.422	3.3	6
gfz2017iejk	2017-04-27	05:34:35	-22.571 ± 4.173	25.100 ± 5.655	8.059 ± 6.050	3.9	7
gfz2017ielh	2017-04-27	06:32:31	-18.469 ± 5.702	23.490 ± 4.259	19.402 ± 4.728	4.3	10
gfz2017ieyi	2017-04-27	13:07:19	-22.623 ± 6.179	25.107 ± 5.480	12.493 ± 6.849	2.8	5
gfz2017ikpj	2017-04-30	15:24:20	-18.377 ± 6.607	23.458 ± 4.275	10.0*	3.6	7
gfz2017illi	2017-05-01	02:30:38	-22.696 ± 3.511	25.172 ± 4.823	14.292 ± 6.052	3.8	9
gfz2017ilxr	2017-05-01	08:44:01	-22.655 ± 3.884	25.168 ± 4.312	9.939 ± 5.987	3.8	9
gfz2017ioyj	2017-05-03	00:30:19	-22.648 ± 4.381	25.205 ± 7.123	14.576 ± 7.133	2.6	5
gfz2017ipdg	2017-05-03	02:58:30	-22.705 ± 4.380	25.086 ± 4.890	3.734 ± 6.580	3.3	7
gfz2017itvj	2017-05-05	16:40:11	-22.665 ± 4.418	25.232 ± 4.604	14.128 ± 6.426	3.7	7
gfz2017iuqw	2017-05-06	03:31:08	-22.604 ± 6.117	25.027 ± 6.856	5.962 ± 6.706	3.1	5
gfz2017iuzi	2017-05-06	07:48:17	-22.624 ± 4.875	25.197 ± 5.435	10.0*	3.1	5
gfz2017ivmv	2017-05-06	14:37:54	-22.179 ± 6.296	25.273 ± 5.468	10.0*	3.6	6
gfz2017ivtn	2017-05-06	18:00:05	-22.571 ± 3.211	25.096 ± 4.279	8.949 ± 5.759	4.3	11
gfz2017ixej	2017-05-07	12:37:17	-22.570 ± 4.126	25.034 ± 4.759	3.420 ± 6.836	3.4	6
gfz2017ixiv	2017-05-07	14:52:38	-22.610 ± 3.680	25.145 ± 4.324	12.198 ± 5.971	3.6	9
gfz2017iyel	2017-05-08	01:47:36	-22.665 ± 3.778	25.180 ± 5.126	9.303 ± 6.013	3.2	7
gfz2017iyit	2017-05-08	03:58:45	-22.625 ± 8.460	25.293 ± 6.688	17.355 ± 15.730	3.2	6
gfz2017izxc	2017-05-09	00:21:49	-22.614 ± 3.231	25.087 ± 4.404	8.679 ± 5.784	3.7	10
gfz2017jcbc	2017-05-10	04:39:20	-22.572 ± 5.965	25.000 ± 6.804	10.0*	3.3	5
gfz2017jfir	2017-05-11	23:53:18	-22.631 ± 3.673	25.104 ± 4.816	12.594 ± 6.044	3.3	9
gfz2017jguq	2017-05-12	19:04:05	-22.143 ± 8.085	24.350 ± 5.405	10.0*	3.4	5
gfz2017jhqc	2017-05-13	05:54:30	-22.647 ± 4.481	25.111 ± 4.906	8.084 ± 6.120	3.5	7
gfz2017jmmy	2017-05-15	21:59:20	-22.676 ± 4.472	25.032 ± 4.361	10.0*	3.1	7
gfz2017jscd	2017-05-18	23:20:51	-22.606 ± 2.920	25.097 ± 3.794	6.586 ± 5.452	4.6	15
gfz2017jswe	2017-05-19	09:28:51	-22.548 ± 6.807	24.945 ± 11.402	10.0*	2.9	4
gfz2017jxfj	2017-05-21	18:39:28	-22.662 ± 3.190	25.207 ± 3.806	14.480 ± 5.563	3.3	11
gfz2017jxpi	2017-05-21	23:41:41	-22.650 ± 4.298	25.168 ± 5.461	4.680 ± 6.683	2.5	6

gfz2017kbxd	2017-05-24	08:10:38	-22.682 ± 3.421	25.208 ± 3.365	14.276 ± 5.377	3.8	12
gfz2017kfao	2017-05-26	01:19:18	-22.619 ± 3.673	25.189 ± 4.152	8.764 ± 5.527	2.7	8
gfz2017kfzu	2017-05-26	14:03:57	-21.318 ± 3.030	25.400 ± 3.770	10.0*	3.3	11
gfz2017kgrj	2017-05-26	22:57:07	-22.583 ± 3.891	25.133 ± 3.674	10.029 ± 5.591	3.1	9
gfz2017kgwa	2017-05-27	01:17:45	-23.603 ± 5.920	25.402 ± 5.144	10.685 ± 6.537	2.2	4
gfz2017khlr	2017-05-27	09:13:03	-22.663 ± 3.554	25.243 ± 5.755	10.053 ± 6.145	2.8	6
gfz2017kibx	2017-05-27	17:24:52	-22.714 ± 4.307	24.974 ± 3.509	3.413 ± 8.624	3.4	11
gfz2017kmjn	2017-05-30	01:47:48	-22.639 ± 3.812	25.191 ± 4.804	12.808 ± 5.660	2.7	8
gfz2017kngc	2017-05-30	13:12:54	-21.497 ± 3.672	25.467 ± 5.332	10.0*	2.8	7
gfz2017koln	2017-05-31	05:04:48	-22.571 ± 3.921	25.125 ± 7.561	13.393 ± 6.343	2.8	6
gfz2017kxam	2017-06-04	21:43:24	-22.305 ± 6.519	24.644 ± 11.497	18.741 ± 14.313	2.8	7
gfz2017kxbp	2017-06-04	22:17:56	-22.595 ± 3.624	25.058 ± 4.503	5.017 ± 5.440	2.8	8
gfz2017kxby	2017-06-04	22:28:24	-22.586 ± 3.996	25.111 ± 5.227	10.810 ± 6.423	2.8	6
gfz2017kxmc	2017-06-05	03:35:27	-22.589 ± 3.877	25.116 ± 7.413	11.295 ± 6.310	2.8	6
gfz2017kymd	2017-06-05	16:44:43	-22.669 ± 4.130	25.122 ± 4.855	6.076 ± 6.373	3	7
gfz2017kyrq	2017-06-05	19:31:50	-22.725 ± 3.425	25.013 ± 3.302	10.0*	3.2	11
gfz2017kzgs	2017-06-06	03:09:11	-22.648 ± 4.636	25.178 ± 7.619	13.530 ± 7.401	2.5	5
gfz2017lacv	2017-06-06	14:19:50	-19.117 ± 5.815	23.536 ± 3.746	6.113 ± 7.867	4	9
gfz2017ldow	2017-06-08	11:49:13	-22.620 ± 4.102	25.219 ± 4.481	18.361 ± 9.988	3.3	7
gfz2017lebx	2017-06-08	18:24:26	-22.689 ± 3.222	25.192 ± 3.503	9.271 ± 5.390	3.7	12
gfz2017lfon	2017-06-09	13:55:30	-21.291 ± 3.367	25.401 ± 5.537	10.0*	3	7
gfz2017ljbn	2017-06-11	11:52:36	-22.606 ± 3.692	25.101 ± 6.213	6.954 ± 5.801	3	7
gfz2017lkam	2017-06-12	00:30:19	-22.684 ± 4.429	24.971 ± 6.434	10.0*	2.8	8
gfz2017lvfz	2017-06-18	03:46:20	-23.903 ± 5.879	26.662 ± 7.905	10.0*	3.2	7
gfz2017mazf	2017-06-21	07:10:32	-22.668 ± 2.679	25.206 ± 3.145	18.414 ± 8.914	5	18
gfz2017mdhg	2017-06-22	13:30:06	-24.497 ± 4.771	24.699 ± 5.744	10.0*	3.1	5
gfz2017mdvl	2017-06-22	20:39:50	-22.576 ± 3.636	25.010 ± 4.668	1.076 ± 6.536	2.9	7
gfz2017mfnn	2017-06-23	18:56:40	-22.578 ± 3.368	25.076 ± 4.115	8.717 ± 5.562	3.3	9
gfz2017mgsk	2017-06-24	10:32:21	-22.625 ± 3.234	25.112 ± 3.309	7.288 ± 5.336	4	14
gfz2017moyc	2017-06-28	22:31:25	-22.672 ± 2.976	25.295 ± 3.505	8.157 ± 5.101	3.5	12
gfz2017mpbu	2017-06-29	00:22:04	-22.580 ± 2.808	25.130 ± 3.247	13.476 ± 5.348	3.9	16
gfz2017mwwf	2017-07-03	06:38:15	-22.693 ± 3.814	25.297 ± 4.095	9.597 ± 5.422	3	8
gfz2017mzbo	2017-07-04	11:37:06	-22.564 ± 2.497	25.131 ± 3.161	11.920 ± 5.253	5.4	19
gfz2017ndzo	2017-07-07	04:16:57	-19.992 ± 3.419	23.115 ± 3.092	6.552 ± 15.220	3.7	14

gfz2017nfsz	2017-07-08	03:14:26	-22.664 ± 3.578	25.180 ± 4.217	9.523 ± 5.347	3	9
gfz2017nijs	2017-07-09	13:57:33	-21.299 ± 3.074	25.371 ± 3.694	10.0*	3.2	11
gfz2017nmrv	2017-07-11	22:36:29	-22.551 ± 5.327	25.106 ± 9.448	6.549 ± 8.244	2.5	5
gfz2017nmwq	2017-07-12	01:02:11	-22.593 ± 3.321	25.111 ± 4.388	6.544 ± 5.398	2.8	9
gfz2017npve	2017-07-13	15:41:54	-24.397 ± 12.745	24.694 ± 5.420	10.0*	3.2	5
gfz2017nryy	2017-07-14	19:52:46	-22.658 ± 2.803	25.222 ± 3.228	18.025 ± 8.789	4.4	16
gfz2017ocfo	2017-07-20	10:34:38	-23.562 ± 16.070	26.351 ± 6.357	10.0*	2.6	4
gfz2017oder	2017-07-20	23:15:51	-22.650 ± 2.994	25.148 ± 3.180	8.846 ± 5.198	4	14
gfz2017oedn	2017-07-21	11:49:15	-22.649 ± 3.638	25.238 ± 3.766	10.941 ± 5.697	3.3	10
gfz2017olss	2017-07-25	15:27:28	-24.422 ± 4.432	24.866 ± 6.281	10.0*	3.1	6
gfz2017ophj	2017-07-27	14:15:34	-21.302 ± 3.270	25.598 ± 4.023	11.703 ± 5.849	3.1	9
gfz2017opwn	2017-07-27	21:54:52	-22.651 ± 3.387	25.206 ± 4.323	16.928 ± 9.551	3.2	10
gfz2017opzd	2017-07-27	23:14:37	-22.539 ± 4.028	25.115 ± 4.576	11.221 ± 5.918	2.9	7
gfz2017ourr	2017-07-30	13:08:33	-21.503 ± 3.220	25.472 ± 5.163	10.0*	2.9	8
gfz2017pcuf	2017-08-03	23:30:43	-22.609 ± 2.706	25.070 ± 3.201	6.101 ± 5.152	4.6	17
gfz2017pjyq	2017-08-07	21:42:16	-22.647 ± 3.153	25.078 ± 3.543	10.0*	3.1	11
gfz2017pnrb	2017-08-09	22:25:05	-22.576 ± 3.230	25.100 ± 3.255	12.417 ± 5.489	3.7	13
gfz2017povt	2017-08-10	13:56:31	-21.316 ± 3.029	25.419 ± 3.769	10.0*	3.2	11
gfz2017ppus	2017-08-11	02:32:28	-22.602 ± 3.569	25.127 ± 3.836	6.950 ± 5.371	3.1	9
gfz2017prqk	2017-08-12	02:37:46	-23.626 ± 3.790	25.678 ± 3.618	6.668 ± 4.201	5.6	18
gfz2017prqr	2017-08-12	02:46:32	-23.641 ± 5.192	25.642 ± 4.259	4.274 ± 5.776	3.5	8
gfz2017pxym	2017-08-15	13:32:28	-21.510 ± 3.222	25.499 ± 5.108	10.0*	2.9	8
gfz2017qgig	2017-08-20	03:33:38	-22.584 ± 4.592	25.080 ± 8.846	9.887 ± 6.372	2.6	6
gfz2017qinj	2017-08-21	08:24:30	-22.578 ± 3.408	25.127 ± 4.043	9.532 ± 5.700	3.6	11
gfz2017qlzp	2017-08-23	05:59:55	-23.606 ± 13.226	25.636 ± 4.946	3.133 ± 5.780	2.8	5
gfz2017qqek	2017-08-25	12:58:19	-21.524 ± 3.223	25.510 ± 5.091	10.0*	2.9	8
gfz2017qufs	2017-08-27	18:11:13	-23.587 ± 5.837	25.686 ± 6.174	14.580 ± 5.307	2.9	5
gfz2017qxgd	2017-08-29	09:48:35	-22.669 ± 3.248	25.176 ± 3.996	22.717 ± 10.530	4	12
gfz2017qzor	2017-08-30	16:23:34	-22.685 ± 6.442	24.562 ± 6.205	6.881 ± 12.084	2.7	4
gfz2017rbpt	2017-08-31	19:12:08	-23.626 ± 5.272	25.712 ± 4.317	6.802 ± 4.968	3.4	9
gfz2017rcze	2017-09-01	13:05:28	-21.475 ± 3.559	25.489 ± 3.976	10.0*	3.2	9
gfz2017rqvi	2017-09-09	03:03:53	-22.663 ± 3.397	25.005 ± 3.057	10.0*	3.4	12
gfz2017rsvk	2017-09-10	05:21:44	-22.670 ± 3.646	25.007 ± 3.512	10.0*	3.2	10
gfz2017ryyb	2017-09-13	13:31:09	-24.505 ± 4.538	24.732 ± 11.423	10.0*	3.7	4

gfz2017sauz	2017-09-14	14:14:59	-21.252 ± 4.409	25.354 ± 5.112	10.0*	3.4	6
gfz2017sdmy	2017-09-16	01:35:07	-22.611 ± 4.239	25.107 ± 4.150	9.879 ± 5.687	2.9	8
gfz2017seul	2017-09-16	18:31:10	-22.567 ± 3.225	25.095 ± 3.422	10.230 ± 5.444	3.6	12
gfz2017sgds	2017-09-17	12:20:39	-22.659 ± 3.277	25.168 ± 5.227	6.621 ± 5.534	3.1	8
gfz2017spod	2017-09-22	15:49:19	-22.588 ± 3.031	25.102 ± 3.242	9.446 ± 5.331	4.1	14
gfz2017tdyp	2017-09-30	13:00:30	-21.507 ± 3.668	25.467 ± 5.340	10.0*	2.7	7
gfz2017tjou	2017-10-03	14:52:19	-22.556 ± 3.752	25.128 ± 4.554	11.446 ± 6.203	3.3	8
gfz2017tlwo	2017-10-04	21:03:58	-22.582 ± 4.648	25.105 ± 5.264	10.025 ± 5.958	3.2	7
gfz2017uazf	2017-10-13	03:27:42	-22.621 ± 4.059	24.957 ± 4.582	10.0*	2.9	7
gfz2017ujyu	2017-10-18	01:27:38	-22.661 ± 3.544	25.003 ± 3.481	10.0*	3.1	11
gfz2017uuvm	2017-10-24	00:17:09	-22.574 ± 4.479	25.198 ± 6.953	7.888 ± 6.594	2.6	6
gfz2017uxnv	2017-10-25	11:50:05	-22.805 ± 8.461	26.518 ± 5.645	10.0*	3.3	5
gfz2017uyyx	2017-10-26	06:34:02	-22.639 ± 3.237	25.150 ± 3.530	13.348 ± 5.480	4.1	12
gfz2017vfig	2017-10-29	18:06:07	-23.640 ± 4.658	25.664 ± 3.903	4.128 ± 5.325	3.6	11
gfz2017vkjc	2017-11-01	12:12:41	-22.622 ± 2.887	25.120 ± 3.263	9.841 ± 5.276	5.3	15
gfz2017vmiw	2017-11-02	14:21:19	-22.580 ± 3.849	25.072 ± 3.991	6.681 ± 5.492	3.5	9
gfz2017vmth	2017-11-02	19:37:56	-22.634 ± 3.127	25.123 ± 3.295	11.007 ± 5.385	4.1	13
gfz2017voed	2017-11-03	14:14:26	-21.281 ± 3.703	25.398 ± 5.328	0.558 ± 7.403	2.6	6
gfz2017vrpe	2017-11-05	11:13:54	-22.581 ± 3.881	25.205 ± 3.950	12.513 ± 5.708	3.1	8
gfz2017vvjk	2017-11-07	12:51:29	-24.545 ± 4.261	24.618 ± 5.171	10.0*	3.1	7
gfz2017vvpg	2017-11-07	15:48:35	-23.337 ± 4.837	24.867 ± 3.744	10.774 ± 4.251	3.3	7
gfz2017vyru	2017-11-09	08:29:55	-22.555 ± 3.003	25.131 ± 3.223	12.173 ± 5.377	3.8	14
gfz2017wbam	2017-11-10	15:09:37	-24.526 ± 4.317	24.707 ± 5.175	12.057 ± 7.603	2.8	7
gfz2017wbvg	2017-11-11	01:39:12	-22.673 ± 4.342	25.149 ± 5.225	8.304 ± 5.519	2.9	8
gfz2017woie	2017-11-17	21:49:51	-22.612 ± 3.284	25.078 ± 3.940	7.656 ± 5.259	3.3	11
gfz2017wzcs	2017-11-23	19:33:35	-22.564 ± 2.849	25.107 ± 3.338	10.867 ± 5.312	4	15
gfz2017xamv	2017-11-24	13:48:34	-22.671 ± 3.319	25.259 ± 4.069	7.710 ± 5.297	3	9
gfz2017xqbl	2017-12-03	02:13:58	-22.589 ± 3.188	25.216 ± 3.337	8.074 ± 5.095	3.3	13
gfz2017xyex	2017-12-07	13:04:11	-21.514 ± 3.915	25.488 ± 4.669	10.0*	2.8	6
gfz2017xygp	2017-12-07	13:55:17	-21.263 ± 4.046	25.575 ± 3.785	10.0*	3.2	8
gfz2017ybde	2017-12-09	03:35:27	-22.592 ± 3.404	25.227 ± 3.599	10.720 ± 5.209	3.5	12
gfz2017ylbs	2017-12-14	14:13:27	-21.302 ± 4.474	25.357 ± 3.967	10.0*	3.4	9
gfz2018acfl	2018-01-02	05:01:40	-22.608 ± 3.749	25.117 ± 3.624	13.451 ± 8.326	3.7	12
gfz2018aijr	2018-01-05	13:58:58	-21.250 ± 3.805	25.374 ± 3.183	10.0*	3.5	12

gfz2018amps	2018-01-07	21:33:55	-22.673 ± 4.553	25.230 ± 3.437	13.613 ± 7.753	3.3	12
gfz2018atis	2018-01-11	13:58:44	-21.263 ± 3.925	25.407 ± 4.175	10.0*	3.3	9
gfz2018aveb	2018-01-12	13:54:40	-21.257 ± 3.963	25.547 ± 3.600	10.0*	3.2	9
gfz2018bkcl	2018-01-20	18:07:35	-22.873 ± 11.569	24.961 ± 4.341	7.619 ± 13.329	2.8	6
gfz2018bskx	2018-01-25	07:29:49	-22.654 ± 4.841	25.158 ± 4.928	8.021 ± 9.862	3	7
gfz2018ccun	2018-01-30	23:43:00	-22.710 ± 4.812	25.264 ± 4.461	18.323 ± 14.691	3.1	8
gfz2018cdns	2018-01-31	09:24:27	-23.624 ± 7.308	26.221 ± 5.705	13.333 ± 6.718	3.6	7
gfz2018cfgw	2018-02-01	08:12:54	-22.667 ± 5.968	25.231 ± 6.369	12.728 ± 9.538	2.9	6
gfz2018ckvu	2018-02-04	09:26:07	-22.596 ± 3.578	25.151 ± 3.331	10.462 ± 8.320	3.7	13

Appendix B

Table B. Entire event catalogue for seismic events detected during the period between January 1st, 2014 and March 1st 2018, excluding events detected in Botswana. Events with a fixed depth are marked with a *.

EventID	Date	Origin time (UTC)	Latitude (°) ± error	Longitude (°) ± error	Depth (km) ± error	Summary Magnitude (M)	No. of stations	Region
gfz2014gcas	2014-03-28	11:50:53	-27.986 ± 60.926	23.170 ± 13.076	10.0*	3.9	6	South Africa
gfz2014gduq	2014-03-29	11:02:06	-26.382 ± 24.012	27.295 ± 24.093	10.0*	4.7	9	South Africa
gfz2014glle	2014-04-02	15:21:32	-25.683 ± 38.463	27.495 ± 34.702	10.0*	4	5	South Africa
gfz2014gobj	2014-04-04	01:37:57	-21.484 ± 248.636	-69.735 ± 159.159	10.0*	6.2	9	Northern Chile
gfz2014hiid	2014-04-15	03:57:20	-52.118 ± 18.977	11.306 ± 32.819	39.426 ± 13.962	6.3	8	Southwest of Africa
gfz2014iczv	2014-04-26	11:36:00	-26.376 ± 30.639	27.202 ± 25.769	82.775 ± 53.536	4.4	7	South Africa
gfz2014jaei	2014-05-09	04:00:18	-24.409 ± 6.675	26.431 ± 10.925	8.122 ± 14.062	4.8	10	South Africa
gfz2014jivt	2014-05-13	21:54:07	-26.412 ± 28.562	27.392 ± 26.705	10.0*	4.5	8	South Africa
gfz2014lqog	2014-06-15	14:16:26	-26.998 ± 35.703	26.744 ± 25.030	10.0*	5.4	9	South Africa
gfz2014plhb	2014-08-08	15:06:06	-26.902 ± 34.883	26.648 ± 23.733	10.0*	5	8	South Africa
gfz2014qjqs	2014-08-21	23:14:50	-26.364 ± 26.627	27.320 ± 25.834	10.0*	5	8	South Africa
gfz2014rbgu	2014-08-31	14:40:08	-26.290 ± 32.801	27.055 ± 30.753	10.0*	4.7	8	South Africa
gfz2014wbdg	2014-11-10	16:34:41	-26.149 ± 38.607	37.451 ± 34.508	10.0*	4.3	4	South Indian Ocean
gfz2014wnyk	2014-11-17	16:52:51	-45.844 ± 41.923	33.639 ± 46.926	10.0*	6.3	8	Prince Edward Islands Region
gfz2015aqkx	2015-01-09	23:41:38	-26.434 ± 35.727	27.367 ± 38.567	10.0*	5.2	6	South Africa
gfz2015aqvl	2015-01-10	05:00:28	-28.130 ± 65.577	26.837 ± 41.484	10.0*	4.2	4	South Africa
gfz2015cnvr	2015-02-06	00:47:56	-27.381 ± 50.320	27.125 ± 41.378	10.0*	4.7	5	South Africa
gfz2015ddar	2015-02-14	08:21:42	-25.937 ± 22.581	24.299 ± 11.047	10.0*	2.8	4	South Africa
gfz2015dwmd	2015-02-24	23:43:18	-10.400 ± 127.667	23.671 ± 26.041	10.0*	5.5	5	Democratic Republic of Congo
gfz2015dxuu	2015-02-25	17:13:49	-26.866 ± 40.796	27.823 ± 47.914	10.0*	4.9	6	South Africa
gfz2015efgr	2015-03-01	19:11:56	-27.573 ± 47.247	26.379 ± 30.879	10.0*	4.9	6	South Africa
gfz2015fnol	2015-03-20	13:44:35	-29.222 ± 65.818	27.540 ± 44.631	10.0*	4.6	7	Lesotho
gfz2015fvos	2015-03-24	22:46:45	-19.746 ± 221.776	-71.779 ± 154.570	10.0*	5.2	9	Off Coast of Northern Chile
gfz2015gbcl	2015-03-27	23:34:47	36.344 ± 18.509	26.462 ± 92.385	31.889 ± 9.511	5.3	11	Dodecanese Islands, Greece
gfz2015gckn	2015-03-28	16:36:36	-23.044 ± 141.529	-70.332 ± 128.392	10.0*	5.9	12	Near Coast of Northern Chile
gfz2015gefi	2015-03-29	16:26:59	-14.104 ± 32.286	41.960 ± 41.824	10.0*	4.5	6	Mozambique Channel

gfz2015gfpf	2015-03-30	10:35:25	-40.120 ± 60.949	75.732 ± 15.592	182.817 ± 11.701	5.5	12	Mid Indian Ridge
gfz2015giot	2015-04-01	01:45:48	-17.360 ± 35.167	-10.375 ± 18.217	26.175 ± 10.805	4.7	8	Southern Mid Atlantic Ridge
gfz2015giqv	2015-04-01	02:48:28	-26.309 ± 36.420	28.326 ± 59.538	10.0*	3.8	5	South Africa
gfz2015gyig	2015-04-09	16:39:05	-25.914 ± 24.213	26.958 ± 32.937	97.741 ± 41.873	4.5	8	South Africa
gfz2015hkyn	2015-04-16	14:30:11	-26.318 ± 21.991	27.223 ± 21.452	68.063 ± 58.860	4.6	10	South Africa
gfz2015hmyu	2015-04-17	16:54:10	-58.926 ± 117.256	-14.586 ± 114.239	10.0*	5.3	9	East of South Sandwich Islands
gfz2015hpth	2015-04-19	05:32:13	-17.454 ± 67.854	66.978 ± 110.235	10.0*	5.1	11	Mauritius/Reunion Region
gfz2015idjl	2015-04-26	16:26:10	28.119 ± 210.721	84.386 ± 137.193	10.0*	5.6	9	Nepal
gfz2015ikfh	2015-04-30	10:19:30	-59.033 ± 123.442	-21.948 ± 118.825	10.0*	5.8	9	East of South Sandwich Islands
gfz2015jewl	2015-05-11	17:41:59	-7.670 ± 36.293	68.129 ± 21.001	3.554 ± 11.302	4.9	8	Chagos Archipelago Region
gfz2015jpzm	2015-05-17	19:43:36	-60.856 ± 112.507	-19.762 ± 102.176	10.0*	5.1	10	East of South Sandwich Islands
gfz2015jqpy	2015-05-18	04:03:32	-41.519 ± 64.561	76.088 ± 17.882	212.645 ± 13.743	4.9	9	Mid Indian Ridge
gfz2015kbqq	2015-05-24	04:53:53	-17.798 ± 41.149	-11.768 ± 30.597	97.947 ± 25.700	5.9	10	Southern Mid Atlantic Ridge
gfz2015kcws	2015-05-24	21:06:35	-60.430 ± 121.081	-26.329 ± 110.717	10.0*	6	10	South Sandwich Islands Region
gfz2015kkqv	2015-05-29	03:13:32	-26.712 ± 29.060	26.453 ± 23.144	10.0*	4.4	10	South Africa
gfz2015kwyj	2015-06-04	20:39:56	-17.914 ± 23.332	24.609 ± 15.744	105.510 ± 31.297	4.4	9	Zambia
gfz2015ldmv	2015-06-08	10:47:05	-0.980 ± 31.921	69.973 ± 21.341	31.042 ± 10.914	5.2	9	Carlsberg Ridge
gfz2015ljyl	2015-06-11	23:27:37	-26.286 ± 26.263	27.261 ± 27.813	10.0*	5.1	10	South Africa
gfz2015ljzi	2015-06-11	23:55:15	-21.485 ± 13.107	33.473 ± 53.346	107.326 ± 31.248	5.1	10	Mozambique
gfz2015lroe	2015-06-16	03:22:06	-28.496 ± 43.900	30.900 ± 49.749	132.547 ± 36.074	4.5	9	South Africa
gfz2015ltty	2015-06-17	08:33:44	-18.656 ± 40.462	31.789 ± 64.662	163.480 ± 36.129	4.9	8	Zimbabwe
gfz2015lucn	2015-06-17	12:52:03	-34.740 ± 59.832	-12.386 ± 117.482	10.0*	6.3	11	Tristan da Cunha Region
gfz2015nnzo	2015-07-12	15:38:59	-26.367 ± 33.359	27.421 ± 42.006	10.0*	4.5	6	South Africa
gfz2015qfxt	2015-08-19	22:15:30	-8.831 ± 53.060	29.367 ± 25.649	10.0*	5.4	8	Lake Tanganyika Region
gfz2015qqnr	2015-08-25	17:40:22	-16.198 ± 16.553	36.372 ± 17.361	60.845 ± 15.461	5.2	11	Mozambique
gfz2015rizw	2015-09-04	20:08:52	-8.299 ± 155.192	102.775 ± 181.377	10.0*	5.4	8	Southwest of Sumatra, Indonesia
gfz2015rkld	2015-09-05	15:05:55	-37.583 ± 75.704	76.638 ± 127.526	10.0*	4.9	9	Mid Indian Ridge
gfz2015rqot	2015-09-08	23:43:46	-9.030 ± 40.644	38.968 ± 33.541	10.0*	5	11	Tanzania
gfz2015rquj	2015-09-09	02:35:26	-60.643 ± 32.933	-26.881 ± 20.123	29.280 ± 9.378	5.3	10	South Sandwich Islands Region
gfz2015rsfh	2015-09-09	21:03:07	35.527 ± 111.636	72.704 ± 112.594	10.0*	5.4	13	Pakistan
gfz2015sfdy	2015-09-16	23:18:48	-32.023 ± 43.634	-70.250 ± 20.971	40.265 ± 8.734	6.4	16	Chile-Argentina Border Region
gfz2015sjos	2015-09-19	09:07:13	-32.338 ± 50.607	-71.029 ± 25.936	30.020 ± 8.804	5.9	11	Near Coast of Central Chile
gfz2015snyn	2015-09-21	18:36:50	-32.707 ± 154.561	-72.536 ± 121.700	10.0*	5.6	11	Off Coast of Central Chile

gfz2015soqv	2015-09-22	04:03:29	11.468 ± 16.103	50.653 ± 18.432	14.381 ± 6.848	5.2	15	Northeastern Somalia
gfz2015soxl	2015-09-22	07:12:56	-32.932 ± 112.002	-71.083 ± 99.697	10.0*	6.2	17	Near Coast of Central Chile
gfz2015subp	2015-09-25	03:13:30	-26.421 ± 20.796	27.440 ± 15.892	80.025 ± 48.644	4.3	15	South Africa
gfz2015tees	2015-09-30	16:06:48	-56.563 ± 29.878	-26.494 ± 15.798	30.636 ± 8.469	5.8	14	South Sandwich Islands Region
gfz2015tgil	2015-10-01	20:14:57	-30.001 ± 17.808	24.879 ± 10.537	8.405 ± 20.159	5.2	12	South Africa
gfz2015tiyf	2015-10-03	06:26:52	-31.996 ± 113.083	-71.990 ± 101.117	10.0*	6.1	17	Near Coast of Central Chile
gfz2015tnjd	2015-10-05	16:33:21	-31.651 ± 132.794	-72.555 ± 113.538	10.0*	6.1	13	Off Coast of Central Chile
gfz2015ttol	2015-10-09	02:03:42	-59.571 ± 101.201	-25.326 ± 143.521	10.0*	5.1	8	South Sandwich Islands Region
gfz2015ttvl	2015-10-09	05:35:50	-27.036 ± 30.747	27.936 ± 23.093	111.751 ± 40.168	4.8	11	South Africa
gfz2015tvxo	2015-10-10	08:56:14	-60.891 ± 27.869	-18.835 ± 20.936	27.622 ± 9.927	5.2	9	East of South Sandwich Islands
gfz2015tzln	2015-10-12	07:23:42	10.735 ± 27.552	56.406 ± 32.364	27.017 ± 12.406	5.3	6	Carlsberg Ridge
gfz2015tzrb	2015-10-12	10:11:11	-17.506 ± 19.862	27.272 ± 16.251	67.639 ± 46.264	4.9	16	Zimbabwe
gfz2015udgb	2015-10-14	09:11:06	-18.214 ± 17.176	33.254 ± 38.644	132.965 ± 19.508	5.3	15	Mozambique
gfz2015ujet	2015-10-17	15:20:45	-17.600 ± 15.251	25.684 ± 8.148	15.308 ± 7.753	4.4	16	Zambia
gfz2015ukbr	2015-10-18	02:55:03	-21.374 ± 8.237	31.886 ± 31.509	133.115 ± 20.840	4.6	14	Zimbabwe
gfz2015uorz	2015-10-20	15:42:36	30.386 ± 105.652	49.009 ± 101.116	10.0*	5.3	10	Western Iran
gfz2015upbq	2015-10-20	20:33:06	-56.678 ± 184.610	-67.645 ± 117.021	10.0*	5.5	11	Drake Passage
gfz2015urez	2015-10-22	00:32:39	-28.283 ± 68.820	72.482 ± 94.286	10.0*	5	13	South Indian Ocean
gfz2015urgl	2015-10-22	01:17:16	-61.076 ± 117.041	-43.398 ± 97.157	10.0*	5.3	12	Scotia Sea
gfz2015uthm	2015-10-23	04:04:21	-45.358 ± 12.532	36.864 ± 17.254	16.217 ± 7.307	5.8	13	Prince Edward Islands Region
gfz2015vbfr	2015-10-27	12:15:35	-16.919 ± 65.129	65.326 ± 116.593	10.0*	5	9	Mid Indian Ridge
gfz2015vbhv	2015-10-27	13:15:14	25.075 ± 31.780	67.552 ± 28.568	40.968 ± 13.342	5.5	8	Pakistan
gfz2015vvzn	2015-11-07	21:00:37	-39.873 ± 30.242	-13.541 ± 14.342	21.022 ± 7.965	4.9	13	Tristan da Cunha Region
gfz2015vyyj	2015-11-09	11:49:10	-23.503 ± 7.908	27.953 ± 25.177	10.0*	3.2	4	South Africa
gfz2015waaz	2015-11-10	02:17:04	-11.406 ± 139.967	64.208 ± 109.583	10.0*	4.8	7	South Indian Ocean
gfz2015wiig	2015-11-14	15:02:08	-18.355 ± 10.047	26.434 ± 11.643	10.0*	3.1	5	Zimbabwe
gfz2015wmoc	2015-11-16	22:32:17	-49.474 ± 73.549	27.638 ± 45.836	10.0*	5	10	South of Africa
gfz2015wnfe	2015-11-17	07:10:08	38.576 ± 17.916	20.590 ± 82.688	3.942 ± 8.873	6	12	Greece
gfz2015wnzr	2015-11-17	17:29:39	38.327 ± 112.747	74.522 ± 104.642	10.0*	6	14	Tajikistan-Xinjiang Border Region
gfz2015xbao	2015-11-24	20:44:48	0.592 ± 81.038	-19.683 ± 90.154	10.0*	4.9	11	Central Mid Atlantic Ridge
gfz2015xcxd	2015-11-25	21:17:18	30.753 ± 85.204	51.946 ± 80.376	10.0*	5.4	16	Northern and Central Iran
gfz2015xczg	2015-11-25	22:23:39	-27.187 ± 29.394	26.827 ± 16.287	119.951 ± 25.219	4.6	10	South Africa
gfz2015xdod	2015-11-26	05:44:22	-11.470 ± 180.717	-70.279 ± 204.956	10.0*	6.7	9	Peru-Brazil Border Region

gfz2015xecf	2015-11-26	12:59:23	-44.530 ± 19.661	37.452 ± 23.465	19.349 ± 13.927	4.8	12	Prince Edward Islands Region
gfz2015xhtq	2015-11-28	13:11:43	14.013 ± 17.919	60.373 ± 17.289	30.276 ± 7.736	5.8	17	Owen Fracture Zone Region
gfz2015xlyt	2015-11-30	20:19:04	-9.296 ± 67.604	68.010 ± 88.314	10.0*	4.9	13	Chagos Archipelago Region
gfz2015xrnk	2015-12-03	21:27:14	-25.918 ± 10.785	27.055 ± 9.943	16.849 ± 25.010	4.3	8	South Africa
gfz2015xtgw	2015-12-04	20:22:24	-53.955 ± 13.901	-1.074 ± 15.339	19.181 ± 6.585	5	19	Bouvet Island Region
gfz2015xtkx	2015-12-04	22:25:07	-47.589 ± 70.216	82.525 ± 80.235	10.0*	6.7	18	Mid Indian Ridge
gfz2015xxup	2015-12-07	07:50:01	35.411 ± 146.170	76.394 ± 112.383	10.0*	6.6	10	Eastern Kashmir
gfz2015yaan	2015-12-08	12:56:06	-31.825 ± 162.147	-71.760 ± 146.566	10.0*	5.8	9	Near Coast of Central Chile
gfz2015ycnj	2015-12-09	21:53:09	-36.746 ± 22.544	48.146 ± 18.733	44.125 ± 17.287	4.6	13	Southwest Indian Ridge
gfz2015ydpm	2015-12-10	12:05:16	-59.452 ± 23.280	-23.556 ± 14.230	30.814 ± 7.510	5.6	18	South Sandwich Islands Region
gfz2015yeua	2015-12-11	03:20:47	-5.748 ± 123.674	102.678 ± 110.797	10.0*	5.6	13	Southern Sumatra, Indonesia
gfz2015ygeu	2015-12-11	22:05:39	-46.789 ± 111.743	84.942 ± 120.434	10.0*	4.8	9	Southeast Indian Ridge
gfz2015ysex	2015-12-18	11:47:14	-3.967 ± 70.165	-13.846 ± 100.820	10.0*	4.9	11	North of Ascension Island
gfz2015ytcm	2015-12-18	23:41:40	-59.913 ± 85.793	-9.124 ± 96.981	10.0*	4.7	10	East of South Sandwich Islands
gfz2015yudr	2015-12-19	13:26:18	-4.735 ± 26.367	27.759 ± 21.106	10.0*	4.9	17	Democratic Republic of Congo
gfz2015ywzw	2015-12-21	02:53:42	-59.245 ± 109.645	27.027 ± 76.545	10.0*	4.9	9	South of Africa
gfz2015zbsp	2015-12-23	16:55:10	-54.342 ± 93.591	-0.687 ± 95.942	10.0*	5.5	9	Bouvet Island Region
gfz2015zeoi	2015-12-25	06:11:05	-54.533 ± 32.380	-22.055 ± 17.986	4.798 ± 9.497	5	11	South Sandwich Islands Region
gfz2015zfoe	2015-12-25	19:14:23	36.164 ± 22.753	72.845 ± 20.816	30.466 ± 6.940	6.6	19	Afghanistan-Tajikistan Border Region
gfz2015zlaz	2015-12-28	19:24:05	0.275 ± 106.448	-21.201 ± 126.196	10.0*	5	8	Central Mid Atlantic Ridge
gfz2015znap	2015-12-29	21:28:29	-56.226 ± 91.646	-24.433 ± 117.951	10.0*	4.8	9	South Sandwich Islands Region
gfz2015zqfr	2015-12-31	15:26:04	-23.513 ± 7.121	27.963 ± 15.898	10.0*	3.3	8	South Africa
gfz2016akki	2016-01-06	16:34:48	-26.109 ± 29.457	27.304 ± 22.891	102.932 ± 43.405	4.3	8	South Africa
gfz2016alwb	2016-01-07	11:39:14	-23.329 ± 7.374	27.329 ± 11.531	10.0*	2.9	5	South Africa
gfz2016aowd	2016-01-09	03:05:33	-16.400 ± 21.873	28.127 ± 17.775	145.432 ± 16.493	5.3	19	Zambia
gfz2016auoj	2016-01-12	05:58:18	-17.621 ± 15.606	26.949 ± 12.687	10.0*	5	15	Zambia
gfz2016auvw	2016-01-12	09:45:36	-31.186 ± 38.246	54.788 ± 84.584	10.0*	5.6	18	South Indian Ocean
gfz2016bcvz	2016-01-16	18:54:35	-1.615 ± 110.564	98.205 ± 96.395	10.0*	5.4	15	Southern Sumatra, Indonesia
gfz2016besr	2016-01-17	19:26:37	-35.264 ± 56.959	65.982 ± 87.229	10.0*	5.3	14	South Indian Ocean
gfz2016blny	2016-01-21	13:02:10	-31.577 ± 46.892	56.879 ± 35.480	10.0*	5.1	8	Southwest Indian Ridge
gfz2016bnmz	2016-01-22	14:49:21	-26.509 ± 78.814	63.490 ± 141.433	10.0*	4.7	8	Southwest Indian Ridge
gfz2016bnyw	2016-01-22	20:51:47	27.591 ± 17.073	57.083 ± 21.004	40.661 ± 8.937	5.4	18	Southern Iran
gfz2016bses	2016-01-25	04:21:57	35.970 ± 114.107	-5.154 ± 91.080	10.0*	6	13	Strait of Gibraltar

gfz2016bshy	2016-01-25	05:53:55	36.859 ± 114.187	-4.690 ± 112.255	10.0*	5.2	12	Strait of Gibraltar
gfz2016bwre	2016-01-27	15:10:53	4.339 ± 158.995	-30.378 ± 120.499	10.0*	5.2	8	Central Mid Atlantic Ridge
gfz2016bymj	2016-01-28	15:02:05	-26.514 ± 30.812	27.655 ± 25.926	10.0*	4.5	7	South Africa
gfz2016cdjr	2016-01-31	07:22:12	-24.036 ± 9.950	27.876 ± 16.174	10.0*	3.2	4	South Africa
gfz2016cjdn	2016-02-03	11:04:22	-20.394 ± 12.369	16.299 ± 46.520	10.0*	5.3	10	Namibia
gfz2016clch	2016-02-04	12:43:54	-0.980 ± 30.569	29.281 ± 32.410	10.0*	4.8	12	Democratic Republic of Congo
gfz2016cufi	2016-02-09	12:28:37	-57.792 ± 74.451	-25.922 ± 73.487	10.0*	5.7	17	South Sandwich Islands Region
gfz2016cvdp	2016-02-10	00:33:01	-30.792 ± 53.938	-72.485 ± 25.976	29.157 ± 8.355	6.3	11	Off Coast of Central Chile
gfz2016cyfh	2016-02-11	17:00:48	-26.143 ± 44.679	-12.199 ± 17.028	29.538 ± 10.492	5.2	11	Southern Mid Atlantic Ridge
gfz2016dcky	2016-02-14	00:24:52	-51.952 ± 103.998	62.411 ± 97.411	10.0*	4.9	8	South Indian Ocean
gfz2016djuj	2016-02-18	01:07:17	-56.517 ± 26.163	-26.743 ± 13.780	138.126 ± 9.193	5.8	18	South Sandwich Islands Region
gfz2016dyda	2016-02-25	21:23:27	-21.231 ± 8.517	32.710 ± 37.425	134.317 ± 21.532	4.9	13	Mozambique
gfz2016dyfn	2016-02-25	22:39:52	-46.627 ± 62.301	32.567 ± 49.215	10.0*	4.8	8	Prince Edward Islands Region
gfz2016dzac	2016-02-26	08:52:51	-32.414 ± 128.802	-66.858 ± 121.524	10.0*	5.6	10	San Luis Province, Argentina
gfz2016eilc	2016-03-02	12:49:53	-6.334 ± 35.045	93.789 ± 17.944	29.842 ± 7.181	7.3	16	South Indian Ocean
gfz2016eism	2016-03-02	16:34:41	-30.700 ± 40.685	55.580 ± 86.417	10.0*	5.6	17	South Indian Ocean
gfz2016ejho	2016-03-03	00:10:53	-5.593 ± 95.018	94.296 ± 91.028	10.0*	5.4	16	Southwest of Sumatra, Indonesia
gfz2016endf	2016-03-05	02:31:57	-26.231 ± 21.854	27.324 ± 16.816	10.0*	4.6	13	South Africa
gfz2016esxx	2016-03-08	06:39:34	-26.088 ± 20.839	27.452 ± 20.906	10.0*	4.4	9	South Africa
gfz2016evlq	2016-03-09	15:50:27	-55.058 ± 93.865	-38.849 ± 102.352	10.0*	5.6	13	South Georgia Island Region
gfz2016eweh	2016-03-10	01:18:14	-31.929 ± 66.446	20.728 ± 22.858	129.420 ± 26.323	5.1	11	South Africa
gfz2016ewil	2016-03-10	03:24:14	-59.521 ± 131.615	-64.647 ± 103.535	10.0*	5	12	Drake Passage
gfz2016fawp	2016-03-12	15:04:15	35.066 ± 21.241	-2.626 ± 36.611	27.824 ± 9.126	5.2	10	Strait of Gibraltar
gfz2016ffec	2016-03-14	23:25:38	-52.731 ± 89.011	19.061 ± 44.663	10.0*	5.7	16	Southwest of Africa
gfz2016ffon	2016-03-15	04:40:53	33.725 ± 83.986	-2.625 ± 82.450	10.0*	5.6	16	Morocco
gfz2016fhtj	2016-03-16	09:24:37	-59.206 ± 95.058	-19.912 ± 121.984	10.0*	5	8	East of South Sandwich Islands
gfz2016flng	2016-03-18	10:52:25	-55.736 ± 29.421	-22.418 ± 18.861	153.476 ± 12.675	5	10	South Sandwich Islands Region
gfz2016fsvk	2016-03-22	10:56:14	-5.046 ± 33.115	37.527 ± 33.235	10.0*	4.8	12	Tanzania
gfz2016fzon	2016-03-26	03:24:30	-3.205 ± 24.530	67.870 ± 15.621	31.103 ± 8.633	5.7	14	Carlsberg Ridge
gfz2016ggjp	2016-03-29	20:53:34	6.579 ± 27.775	62.451 ± 23.789	268.738 ± 16.300	4.4	7	Carlsberg Ridge
gfz2016hbnb	2016-04-10	10:28:28	36.381 ± 116.415	73.356 ± 114.191	10.0*	6.8	10	Northwestern Kashmir
gfz2016hfno	2016-04-12	15:17:12	-11.745 ± 17.994	39.650 ± 16.488	66.705 ± 14.988	5.2	12	Mozambique
gfz2016hgca	2016-04-12	22:34:44	-47.578 ± 45.590	28.325 ± 42.813	10.0*	5	11	South of Africa

gfz2016hhgy	2016-04-13	14:12:20	-8.861 ± 23.090	44.443 ± 18.693	59.160 ± 18.009	6.1	11	Northwest of Madagascar
gfz2016hqzu	2016-04-18	21:57:14	-33.761 ± 53.395	73.822 ± 15.363	20.071 ± 7.926	5.1	14	South Indian Ocean
gfz2016hrmj	2016-04-19	04:18:23	-55.890 ± 78.605	-25.909 ± 103.830	10.0*	5	11	South Sandwich Islands Region
gfz2016hrop	2016-04-19	05:25:56	-55.000 ± 87.640	-23.535 ± 102.889	10.0*	5.8	10	South Sandwich Islands Region
gfz2016hwfb	2016-04-21	18:07:46	-23.692 ± 104.800	-67.328 ± 97.064	153.000 ± 0.000	5.3	16	Chile-Argentina Border Region
gfz2016ieam	2016-04-26	01:05:04	-45.715 ± 12.768	33.615 ± 21.064	9.566 ± 7.819	4.8	10	Prince Edward Islands Region
gfz2016ifxy	2016-04-27	02:04:13	-51.563 ± 96.911	26.218 ± 43.286	10.0*	5.2	14	South of Africa
gfz2016ijhz	2016-04-28	22:32:04	-26.600 ± 35.413	28.190 ± 33.456	10.0*	4.7	7	South Africa
gfz2016ipog	2016-05-02	08:31:01	-4.069 ± 33.397	23.703 ± 21.384	10.0*	4.9	12	Democratic Republic of Congo
gfz2016irqv	2016-05-03	12:05:56	-23.829 ± 10.050	27.906 ± 21.181	10.0*	3.2	5	South Africa
gfz2016iuxu	2016-05-05	07:01:51	12.502 ± 95.071	52.877 ± 96.971	10.0*	5.5	9	Socotra Region
gfz2016jjnu	2016-05-13	07:01:10	29.440 ± 27.499	68.453 ± 28.592	29.367 ± 9.147	5.3	10	Pakistan
gfz2016jopx	2016-05-16	01:45:50	30.178 ± 19.221	35.136 ± 51.393	28.985 ± 9.701	4.8	9	Dead Sea Region
gfz2016jtbh	2016-05-18	12:10:14	-25.066 ± 37.351	27.139 ± 25.836	10.0*	3.4	4	South Africa
gfz2016kdzt	2016-05-24	11:46:52	-23.373 ± 9.130	27.495 ± 17.022	10.0*	3.1	5	South Africa
gfz2016kldv	2016-05-28	09:47:02	-56.607 ± 26.540	-25.984 ± 14.084	91.622 ± 9.467	7.2	17	South Sandwich Islands Region
gfz2016koqn	2016-05-30	07:36:18	-48.242 ± 18.255	-5.010 ± 15.982	25.692 ± 8.478	5.4	13	Southern Mid Atlantic Ridge
gfz2016liws	2016-06-10	09:27:12	-8.607 ± 26.744	-11.718 ± 16.352	19.565 ± 8.645	5.4	11	Ascension Island Region
gfz2016lysa	2016-06-19	01:15:45	-31.638 ± 43.894	60.457 ± 17.160	6.156 ± 8.966	5	9	Southwest Indian Ridge
gfz2016majm	2016-06-19	23:13:17	-3.420 ± 28.133	-14.424 ± 17.619	33.965 ± 10.808	5.3	10	North of Ascension Island
gfz2016mdrs	2016-06-21	18:47:43	-44.531 ± 89.344	-14.667 ± 127.143	10.0*	4.8	7	Southern Mid Atlantic Ridge
gfz2016mesi	2016-06-22	08:12:48	-12.729 ± 53.888	32.694 ± 51.290	111.393 ± 36.379	4.9	9	Zambia
gfz2016mezf	2016-06-22	11:42:28	-26.970 ± 23.197	26.773 ± 12.567	97.154 ± 30.308	4.9	14	South Africa
gfz2016mgdr	2016-06-23	03:05:48	-61.123 ± 50.653	-41.083 ± 16.739	38.994 ± 9.484	5.3	13	Scotia Sea
gfz2016mnib	2016-06-27	01:15:44	-25.223 ± 26.300	29.426 ± 52.911	10.0*	3.8	5	South Africa
gfz2016mprf	2016-06-28	08:09:24	-2.970 ± 116.122	81.180 ± 116.690	10.0*	5.3	8	South Indian Ocean
gfz2016mrsn	2016-06-29	11:06:31	-17.122 ± 62.251	-16.159 ± 110.451	10.0*	5.1	10	Southern Mid Atlantic Ridge
gfz2016mtqm	2016-06-30	12:20:53	-29.156 ± 47.272	56.845 ± 131.490	10.0*	4.9	9	South Indian Ocean
gfz2016nkhm	2016-07-09	15:05:48	-25.627 ± 15.470	27.122 ± 14.398	10.0*	4.2	8	South Africa
gfz2016nmzr	2016-07-11	02:33:44	-43.290 ± 91.640	62.904 ± 113.760	10.0*	4.7	8	South Indian Ocean
gfz2016nnrz	2016-07-11	11:49:34	-23.724 ± 9.311	27.640 ± 17.970	10.0*	3.4	5	South Africa
gfz2016npdk	2016-07-12	06:43:08	-31.295 ± 26.639	50.158 ± 24.657	228.011 ± 24.114	4.9	13	South Indian Ocean
gfz2016nqbp	2016-07-12	18:56:54	-30.674 ± 54.855	54.119 ± 131.714	10.0*	4.7	8	South Indian Ocean

gfz2016nqpy	2016-07-13	02:12:20	-9.584 ± 49.918	30.332 ± 26.779	10.0*	4.4	10	Lake Tanganyika Region
gfz2016nqrp	2016-07-13	03:01:28	-6.861 ± 27.525	35.443 ± 21.272	10.0*	5	16	Tanzania
gfz2016nvoe	2016-07-15	18:58:39	-24.640 ± 42.148	80.943 ± 14.950	24.050 ± 7.284	5.3	15	South Indian Ocean
gfz2016ocdc	2016-07-19	09:20:42	-28.165 ± 34.146	26.924 ± 15.998	10.0*	4.7	11	South Africa
gfz2016oexc	2016-07-20	21:42:30	-28.042 ± 30.481	8.281 ± 53.401	10.0*	4	7	South Atlantic Ocean
gfz2016ofkt	2016-07-21	04:37:19	-48.132 ± 13.036	30.696 ± 26.087	30.356 ± 8.944	5	13	South of Africa
gfz2016oplw	2016-07-26	16:32:30	-54.292 ± 89.041	-19.818 ± 109.553	10.0*	5.3	9	Southwestern Atlantic Ocean
gfz2016oyfn	2016-07-31	11:33:13	-56.619 ± 29.561	-27.060 ± 15.627	31.347 ± 8.232	6.2	15	South Sandwich Islands Region
gfz2016oztl	2016-08-01	07:42:58	-24.445 ± 46.775	81.393 ± 15.460	4.370 ± 8.210	6	14	South Indian Ocean
gfz2016pbop	2016-08-02	07:32:30	-59.509 ± 82.398	-23.761 ± 96.068	10.0*	5.5	12	South Sandwich Islands Region
gfz2016phlb	2016-08-05	12:34:27	-24.146 ± 56.669	81.170 ± 18.099	28.348 ± 9.184	5.9	10	South Indian Ocean
gfz2016pikb	2016-08-06	01:12:37	-28.091 ± 32.643	50.954 ± 23.762	72.675 ± 21.985	4.5	9	South Indian Ocean
gfz2016qdmx	2016-08-17	14:29:54	-7.134 ± 16.346	32.538 ± 18.082	30.587 ± 14.412	5.1	10	Tanzania
gfz2016qfqr	2016-08-18	18:40:58	-30.558 ± 53.057	28.494 ± 29.716	163.997 ± 29.814	5.1	11	South Africa
gfz2016qgqd	2016-08-19	07:33:00	-56.073 ± 30.551	-27.570 ± 14.728	230.238 ± 10.566	6.9	15	South Sandwich Islands Region
gfz2016qhav	2016-08-19	12:56:40	-49.990 ± 108.383	-26.854 ± 104.948	10.0*	5	8	South Georgia Rise
gfz2016qhay	2016-08-19	13:00:11	-55.608 ± 37.884	-30.955 ± 16.426	32.337 ± 8.853	5.2	13	South Sandwich Islands Region
gfz2016qhjy	2016-08-19	17:33:40	-55.744 ± 41.360	-33.067 ± 15.613	40.427 ± 10.162	5.7	14	South Georgia Island Region
gfz2016qhqa	2016-08-19	20:37:19	-55.919 ± 35.704	-31.718 ± 14.607	30.339 ± 7.819	5.6	16	South Georgia Island Region
gfz2016qito	2016-08-20	11:27:19	-54.917 ± 46.106	-31.948 ± 18.268	31.880 ± 9.590	5.5	11	South Georgia Island Region
gfz2016qjzq	2016-08-21	03:45:24	-55.827 ± 38.495	-31.961 ± 15.803	33.363 ± 8.686	6.3	14	South Georgia Island Region
gfz2016qmeq	2016-08-22	08:32:36	-56.494 ± 125.902	-32.725 ± 119.849	10.0*	5.4	9	South Georgia Island Region
gfz2016qnox	2016-08-23	02:52:01	-55.743 ± 94.838	-31.256 ± 120.829	10.0*	5.3	9	South Georgia Island Region
gfz2016qpzr	2016-08-24	10:34:50	19.580 ± 41.245	94.851 ± 24.189	31.049 ± 8.614	6.8	12	Myanmar
gfz2016qqgd	2016-08-24	13:50:06	-8.647 ± 90.733	88.553 ± 92.538	10.0*	5.2	15	South Indian Ocean
gfz2016qsfj	2016-08-25	15:44:17	-27.098 ± 26.447	27.941 ± 20.229	130.376 ± 26.459	4.5	12	South Africa
gfz2016qycp	2016-08-28	21:08:38	-24.360 ± 17.921	26.895 ± 14.189	10.0*	3.1	5	South Africa
gfz2016qzzd	2016-08-29	21:40:41	-56.311 ± 93.076	-3.732 ± 86.755	10.0*	4.7	11	Southern Mid Atlantic Ridge
gfz2016radp	2016-08-29	23:55:43	-17.206 ± 35.279	24.867 ± 9.623	9.822 ± 8.374	3.7	6	Zambia
gfz2016rauf	2016-08-30	08:09:10	-36.892 ± 137.122	-72.797 ± 113.108	10.0*	5.6	12	Near Coast of Central Chile
gfz2016rbiy	2016-08-30	15:46:08	-55.825 ± 34.843	-29.417 ± 16.224	31.668 ± 8.827	5.5	13	South Sandwich Islands Region
gfz2016rdtr	2016-08-31	23:26:54	-26.889 ± 26.645	26.484 ± 14.003	10.0*	4.3	12	South Africa
gfz2016rgdt	2016-09-02	06:49:09	-54.696 ± 37.484	-28.891 ± 17.755	70.001 ± 11.573	5.4	11	South Sandwich Islands Region
gfz2016rgng	2016-09-02	11:38:48	-23.630 ± 17.607	29.042 ± 39.938	10.0*	3.7	5	South Africa

gfz2016rich	2016-09-03	08:19:03	-29.016 ± 46.068	58.063 ± 118.221	10.0*	5.3	11	South Indian Ocean
gfz2016rlpk	2016-09-05	06:22:46	-29.920 ± 46.583	27.852 ± 22.695	10.0*	4.8	11	Lesotho
gfz2016rpco	2016-09-07	04:24:07	-10.426 ± 13.845	36.142 ± 14.400	7.754 ± 13.433	5.1	11	Tanzania
gfz2016rslc	2016-09-09	00:03:31	-31.768 ± 171.917	-64.927 ± 162.209	10.0*	5.2	8	Cordoba Province, Argentina
gfz2016ruvr	2016-09-10	07:47:05	-23.586 ± 8.884	27.956 ± 19.010	10.0*	3.5	7	South Africa
gfz2016rvey	2016-09-10	12:27:30	-1.556 ± 29.384	31.968 ± 26.469	10.0*	5.8	17	Lake Victoria Region
gfz2016scag	2016-09-14	06:02:53	-29.249 ± 55.933	58.019 ± 129.142	10.0*	5	9	South Indian Ocean
gfz2016sgdf	2016-09-16	12:04:35	-56.533 ± 87.534	-30.511 ± 96.981	10.0*	5.5	12	South Sandwich Islands Region
gfz2016sgqg	2016-09-16	18:38:36	-29.985 ± 63.592	57.004 ± 121.026	10.0*	5.7	10	South Indian Ocean
gfz2016sgxo	2016-09-16	22:22:35	-22.897 ± 18.004	37.605 ± 89.678	10.0*	4.6	10	Mozambique Channel
gfz2016sikl	2016-09-17	18:00:45	-55.595 ± 42.814	-30.100 ± 19.760	65.091 ± 12.789	5.1	9	South Sandwich Islands Region
gfz2016sjse	2016-09-18	11:03:23	-27.927 ± 40.415	52.932 ± 111.630	10.0*	5.3	12	South Indian Ocean
gfz2016smqj	2016-09-20	01:32:11	-30.773 ± 44.466	54.703 ± 98.881	10.0*	5.2	13	South Indian Ocean
gfz2016soja	2016-09-21	00:06:52	-54.614 ± 28.518	-23.489 ± 16.815	297.641 ± 12.598	4.7	12	South Sandwich Islands Region
gfz2016sojb	2016-09-21	00:06:00	-20.788 ± 25.877	39.551 ± 17.664	11.733 ± 17.379	4	9	Mozambique Channel
gfz2016solc	2016-09-21	01:08:54	-12.932 ± 18.701	42.788 ± 16.263	31.906 ± 14.145	5.4	13	Northwest of Madagascar
gfz2016sopb	2016-09-21	03:10:20	-21.492 ± 10.408	30.762 ± 52.394	107.215 ± 23.789	5	12	Zimbabwe
gfz2016srsb	2016-09-22	20:06:01	-21.310 ± 12.870	34.396 ± 57.867	115.973 ± 19.883	5.9	15	Mozambique
gfz2016stfw	2016-09-23	16:12:17	-3.119 ± 16.147	28.848 ± 18.046	152.177 ± 16.818	4.5	15	Lake Tanganyika Region
gfz2016sukv	2016-09-24	07:50:18	-55.567 ± 46.581	-32.892 ± 20.153	74.273 ± 12.720	5.1	9	South Georgia Island Region
gfz2016swtk	2016-09-25	14:27:14	-21.202 ± 18.630	34.401 ± 68.794	104.558 ± 25.401	5.3	9	Mozambique
gfz2016tjkw	2016-10-02	12:53:10	-27.956 ± 44.732	51.207 ± 28.858	17.879 ± 19.179	5.1	8	South Indian Ocean
gfz2016tumh	2016-10-08	14:06:50	-12.128 ± 36.830	36.365 ± 55.140	10.0*	4.7	7	Mozambique
gfz2016umaf	2016-10-18	04:26:07	-63.702 ± 106.123	-46.960 ± 103.082	10.0*	5.5	12	Southwestern Atlantic Ocean
gfz2016umed	2016-10-18	06:26:55	-26.880 ± 37.178	23.588 ± 9.145	149.260 ± 21.759	3.8	7	South Africa
gfz2016usbi	2016-10-21	11:49:41	-23.682 ± 8.460	28.199 ± 20.147	10.0*	3.4	6	South Africa
gfz2016vbtq	2016-10-26	19:18:04	43.129 ± 20.406	12.085 ± 60.668	1.826 ± 9.135	6.1	11	Central Italy
gfz2016vcfa	2016-10-27	01:03:18	-2.743 ± 26.357	-15.713 ± 18.022	30.231 ± 10.318	5.2	10	North of Ascension Island
gfz2016vfvb	2016-10-29	00:33:50	-46.985 ± 21.263	32.551 ± 28.488	19.840 ± 14.433	5.1	12	Prince Edward Islands Region
gfz2016vict	2016-10-30	06:40:12	43.736 ± 85.146	12.722 ± 111.598	10.0*	6.4	16	Central Italy
gfz2016vjwu	2016-10-31	05:59:22	-26.964 ± 29.674	26.780 ± 18.588	10.0*	5	10	South Africa
gfz2016vkqr	2016-10-31	16:02:42	19.860 ± 95.591	63.156 ± 101.648	10.0*	5.4	11	Arabian Sea
gfz2016vndj	2016-11-02	00:43:06	-26.656 ± 28.810	27.690 ± 21.831	10.0*	4.7	9	South Africa
gfz2016vqzp	2016-11-04	03:21:30	-22.177 ± 13.465	36.733 ± 18.316	87.443 ± 15.181	5.4	13	Mozambique Channel

gfz2016vxwk	2016-11-07	21:31:20	-7.667 ± 170.815	105.535 ± 139.997	10.0*	5.5	9	Java, Indonesia
gfz2016wlug	2016-11-15	12:31:28	-52.453 ± 16.693	5.392 ± 21.653	19.230 ± 8.786	5	11	Bouvet Island Region
gfz2016wnok	2016-11-16	11:50:20	-23.341 ± 9.531	27.280 ± 14.484	10.0*	3	5	South Africa
gfz2016wqxh	2016-11-18	07:42:14	36.234 ± 15.975	5.921 ± 36.246	30.480 ± 7.696	5.6	16	Northern Algeria
gfz2016wskm	2016-11-19	03:30:40	-16.636 ± 24.822	38.218 ± 37.234	10.0*	5	12	Mozambique
gfz2016wubc	2016-11-20	00:58:18	-61.890 ± 127.884	-54.289 ± 153.051	10.0*	5.4	9	South Shetland Islands
gfz2016wufp	2016-11-20	03:20:19	-42.197 ± 23.194	38.225 ± 23.972	31.733 ± 19.459	4.3	8	Prince Edward Islands Region
gfz2016wurb	2016-11-20	09:08:02	-44.462 ± 57.805	38.767 ± 38.572	10.0*	4.9	8	Prince Edward Islands Region
gfz2016xcwd	2016-11-24	20:46:31	-44.046 ± 23.803	38.904 ± 24.041	4.208 ± 18.297	4.5	9	Prince Edward Islands Region
gfz2016xhzq	2016-11-27	16:14:46	-17.852 ± 25.160	39.200 ± 60.384	133.972 ± 33.464	4.7	13	Mozambique
gfz2016xjfc	2016-11-28	08:07:40	-40.959 ± 134.348	85.347 ± 129.170	10.0*	5.1	8	Southeast Indian Ridge
gfz2016xpqv	2016-12-01	20:52:19	-33.722 ± 44.573	51.230 ± 72.501	10.0*	5	12	South Indian Ocean
gfz2016xsaj	2016-12-03	03:57:48	-25.983 ± 23.472	38.453 ± 64.485	10.0*	4.9	7	Mozambique Channel
gfz2016ynto	2016-12-15	01:30:04	-29.139 ± 49.330	56.081 ± 97.533	10.0*	5.3	14	South Indian Ocean
gfz2016ysss	2016-12-17	18:46:12	-29.791 ± 43.066	52.612 ± 69.091	10.0*	5	13	South Indian Ocean
gfz2016ytas	2016-12-17	22:47:48	-25.104 ± 8.090	27.533 ± 7.946	19.374 ± 14.702	3.6	7	South Africa
gfz2016ytkb	2016-12-18	03:31:36	-29.146 ± 37.195	56.407 ± 13.604	15.430 ± 7.540	5.2	14	South Indian Ocean
gfz2016yued	2016-12-18	13:29:33	-9.211 ± 149.411	-64.501 ± 109.234	10.0*	6.1	12	Western Brazil
gfz2016yuef	2016-12-18	13:31:45	-9.567 ± 145.995	-65.730 ± 110.414	10.0*	5.8	14	Western Brazil
gfz2016yxgb	2016-12-20	06:03:23	37.849 ± 101.857	26.984 ± 96.753	10.0*	5.4	13	Dodecanese Islands, Greece
gfz2016zhab	2016-12-25	14:22:24	-44.433 ± 113.498	-73.879 ± 128.900	10.0*	7.7	11	Southern Chile
gfz2016zmmr	2016-12-28	14:25:34	36.134 ± 115.044	70.810 ± 101.115	10.0*	5.3	12	Hindu Kush Region, Afghanistan
gfz2016zodk	2016-12-29	12:01:35	-23.194 ± 6.539	27.613 ± 13.289	10.0*	3.4	7	South Africa
gfz2017ahot	2017-01-05	03:23:56	-22.433 ± 59.180	-12.106 ± 133.790	10.0*	4.8	8	Southern Mid Atlantic Ridge
gfz2017akay	2017-01-06	11:49:59	-23.722 ± 32.163	27.692 ± 32.764	10.0*	3	5	South Africa
gfz2017aksl	2017-01-06	20:39:42	-18.472 ± 61.707	-14.554 ± 116.394	10.0*	4.9	10	Southern Mid Atlantic Ridge
gfz2017atyv	2017-01-11	22:07:40	-20.464 ± 31.119	42.687 ± 17.942	22.922 ± 17.875	5.5	7	Madagascar
gfz2017atyw	2017-01-11	21:58:15	-22.842 ± 149.869	-68.579 ± 163.914	10.0*	6.1	9	Northern Chile
gfz2017avpd	2017-01-12	19:19:48	4.446 ± 113.567	95.392 ± 106.136	10.0*	5.3	14	Northern Sumatra, Indonesia
gfz2017bcbb	2017-01-16	08:21:08	-48.096 ± 17.246	31.675 ± 48.630	40.191 ± 13.881	5	7	South of Africa
gfz2017beph	2017-01-17	17:47:46	-13.514 ± 44.269	14.611 ± 50.429	114.396 ± 21.462	5.5	14	Angola
gfz2017boti	2017-01-23	07:13:46	-48.654 ± 64.552	29.866 ± 64.044	10.0*	5	7	South of Africa
gfz2017bwnm	2017-01-27	13:20:18	-25.946 ± 16.194	24.018 ± 7.672	1.530 ± 13.690	2.9	5	South Africa

gfz2017bwtt	2017-01-27	16:29:47	4.982 ± 126.472	37.860 ± 79.146	10.0*	5.2	8	Ethiopia
gfz2017cale	2017-01-29	16:42:53	-29.161 ± 38.924	57.704 ± 85.772	10.0*	5.9	19	South Indian Ocean
gfz2017cdsh	2017-01-31	11:43:10	-39.143 ± 49.637	46.607 ± 68.646	10.0*	4.5	8	Southwest Indian Ridge
gfz2017cobw	2017-02-06	03:51:41	39.636 ± 121.097	26.294 ± 115.573	10.0*	5.4	11	Turkey
gfz2017coqd	2017-02-06	10:57:56	40.433 ± 126.241	27.047 ± 115.825	10.0*	5.3	10	Turkey
gfz2017cpuj	2017-02-07	02:24:04	39.636 ± 103.143	26.354 ± 113.128	10.0*	5.1	11	Turkey
gfz2017cvia	2017-02-10	02:59:04	-18.896 ± 55.457	-11.805 ± 109.192	10.0*	5.2	11	Southern Mid Atlantic Ridge
gfz2017cwjf	2017-02-10	16:43:48	-18.135 ± 20.422	34.735 ± 54.036	133.961 ± 23.533	5.7	12	Mozambique
gfz2017czbc	2017-02-12	04:01:19	-57.156 ± 86.752	-28.028 ± 91.169	10.0*	5.5	12	South Sandwich Islands Region
gfz2017dgmi	2017-02-16	05:39:10	-19.943 ± 59.378	-9.724 ± 35.123	10.0*	5	8	South Atlantic Ocean
gfz2017dqas	2017-02-21	11:08:45	-29.009 ± 52.580	57.314 ± 105.455	10.0*	5	12	South Indian Ocean
gfz2017drsk	2017-02-22	09:14:32	-26.876 ± 27.788	26.741 ± 15.965	10.0*	4.6	11	South Africa
gfz2017dusf	2017-02-24	00:32:14	-8.760 ± 35.170	30.141 ± 20.703	10.0*	5.9	13	Lake Tanganyika Region
gfz2017dutu	2017-02-24	01:19:28	-9.538 ± 48.973	29.864 ± 28.573	10.0*	4.8	9	Lake Tanganyika Region
gfz2017ebbm	2017-02-27	12:02:04	-7.670 ± 45.607	30.448 ± 28.132	10.0*	5	9	Lake Tanganyika Region
gfz2017epwu	2017-03-07	14:41:37	-25.860 ± 16.624	27.333 ± 15.920	10.0*	4.6	9	South Africa
gfz2017fbty	2017-03-14	02:51:30	5.365 ± 112.501	90.249 ± 110.721	10.0*	6.1	11	Off West Coast of Northern Sumatra
gfz2017flms	2017-03-19	10:35:43	-10.183 ± 25.948	37.586 ± 27.754	10.0*	5.2	11	Tanzania
gfz2017fwei	2017-03-25	06:51:47	-26.941 ± 35.388	27.785 ± 22.292	10.0*	4.3	8	South Africa
gfz2017gefx	2017-03-29	16:44:15	-8.779 ± 50.672	30.121 ± 29.905	10.0*	4.6	8	Lake Tanganyika Region
gfz2017genp	2017-03-29	20:37:21	-11.669 ± 31.187	39.335 ± 25.922	10.0*	5.2	11	Mozambique
gfz2017gglt	2017-03-30	21:58:03	-54.797 ± 94.594	-31.744 ± 132.797	10.0*	4.9	8	South Georgia Island Region
gfz2017ghvt	2017-03-31	16:09:42	-54.182 ± 95.764	3.384 ± 73.559	10.0*	5.1	10	Bouvet Island Region
gfz2017giua	2017-04-01	04:25:06	-26.168 ± 10.978	27.238 ± 9.270	18.863 ± 23.238	4.4	10	South Africa
gfz2017gmin	2017-04-03	03:08:55	-26.817 ± 28.732	26.779 ± 16.340	68.192 ± 50.873	5.6	12	South Africa
gfz2017gmqu	2017-04-03	07:19:43	-37.512 ± 87.156	79.134 ± 129.492	10.0*	5.1	8	Mid Indian Ridge
gfz2017gxjp	2017-04-09	04:11:15	-53.276 ± 112.531	25.583 ± 64.047	10.0*	5.2	10	South of Africa
gfz2017hepf	2017-04-13	02:58:31	-12.289 ± 70.359	-14.937 ± 116.450	10.0*	4.9	9	Southern Mid Atlantic Ridge
gfz2017heqw	2017-04-13	03:42:47	-31.273 ± 122.700	-71.747 ± 128.504	10.0*	5.4	11	Near Coast of Central Chile
gfz2017hgps	2017-04-14	05:29:41	-12.842 ± 58.576	-14.556 ± 94.130	10.0*	5.2	13	Southern Mid Atlantic Ridge
gfz2017hiqu	2017-04-15	08:19:32	-22.761 ± 54.776	-67.021 ± 26.504	33.195 ± 9.614	6.4	10	Chile-Bolivia Border Region
gfz2017hkpc	2017-04-16	09:44:10	-7.928 ± 95.125	82.471 ± 120.691	10.0*	5.6	9	South Indian Ocean
gfz2017hnzr	2017-04-18	06:29:45	-57.145 ± 32.933	-24.847 ± 19.420	170.909 ± 13.583	5	9	South Sandwich Islands Region
gfz2017hwkc	2017-04-22	20:50:42	-26.761 ± 20.509	26.465 ± 12.703	12.191 ± 42.757	5	11	South Africa

gfz2017iiky	2017-04-29	10:53:41	-7.390 ± 53.168	29.356 ± 27.087	60.020 ± 25.850	5.3	11	Lake Tanganyika Region
gfz2017iukl	2017-05-06	00:16:05	-61.544 ± 127.462	-38.733 ± 133.934	10.0*	5.5	8	Scotia Sea
gfz2017jdmf	2017-05-10	23:23:29	-57.123 ± 105.499	-26.986 ± 103.377	10.0*	6	9	South Sandwich Islands Region
gfz2017jesl	2017-05-11	15:41:24	-55.503 ± 35.365	-24.584 ± 19.669	38.942 ± 12.084	5.3	9	South Sandwich Islands Region
gfz2017jkmz	2017-05-14	19:44:15	-21.538 ± 137.061	-68.310 ± 126.349	10.0*	6.1	11	Chile-Bolivia Border Region
gfz2017jmlm	2017-05-15	21:12:13	-56.794 ± 96.143	-26.907 ± 117.315	10.0*	5.2	9	South Sandwich Islands Region
gfz2017jpje	2017-05-17	11:30:33	36.061 ± 113.034	27.350 ± 121.275	10.0*	5.4	9	Dodecanese Islands, Greece
gfz2017jqlu	2017-05-18	01:57:44	-26.997 ± 33.896	26.747 ± 20.584	10.0*	4.4	8	South Africa
gfz2017jwkr	2017-05-21	08:12:14	-28.313 ± 68.041	73.580 ± 94.991	10.0*	5.1	13	Mid Indian Ridge
gfz2017kfwn	2017-05-26	12:24:28	-23.254 ± 8.632	27.167 ± 10.488	10.0*	2.6	5	South Africa
gfz2017khyx	2017-05-27	15:53:28	38.285 ± 17.931	27.201 ± 78.864	4.992 ± 8.886	5.4	12	Turkey
gfz2017kjkw	2017-05-28	11:04:49	40.638 ± 144.233	27.074 ± 105.937	10.0*	5	9	Turkey
gfz2017kncs	2017-05-30	11:29:37	-59.539 ± 71.603	-26.996 ± 73.584	10.0*	6	18	South Sandwich Islands Region
gfz2017lheh	2017-06-10	10:57:56	-47.038 ± 70.570	-9.517 ± 88.090	10.0*	5.2	12	Southern Mid Atlantic Ridge
gfz2017lkff	2017-06-12	02:43:24	-33.239 ± 106.547	-72.317 ± 95.046	10.0*	5.8	18	Off Coast of Central Chile
gfz2017lkyf	2017-06-12	12:28:40	38.707 ± 89.397	25.183 ± 93.236	10.0*	6.3	16	Aegean Sea
gfz2017llus	2017-06-12	23:52:55	-27.337 ± 23.965	26.935 ± 14.231	10.0*	4.7	14	South Africa
gfz2017lnig	2017-06-13	19:38:26	31.346 ± 111.455	89.797 ± 93.685	10.0*	5.2	16	Xizang
gfz2017luvs	2017-06-17	22:33:01	-50.930 ± 44.440	162.124 ± 50.748	10.0*	7	9	Auckland Islands, N.Z. Region
gfz2017lvzh	2017-06-18	13:31:09	-21.270 ± 8.971	33.308 ± 37.817	123.859 ± 20.004	5.1	15	Mozambique
gfz2017lwkw	2017-06-18	19:22:25	-30.107 ± 45.715	56.547 ± 110.786	10.0*	4.7	12	South Indian Ocean
gfz2017lxdo	2017-06-19	04:38:01	-7.415 ± 142.739	119.780 ± 180.954	10.0*	5.6	15	Flores Sea
gfz2017mcin	2017-06-22	01:00:21	-25.481 ± 13.107	26.811 ± 13.731	10.0*	3.4	6	South Africa
gfz2017mgct	2017-06-24	02:37:17	-19.347 ± 12.958	34.373 ± 39.777	143.085 ± 17.945	6	18	Mozambique
gfz2017mhdw	2017-06-24	16:09:15	-16.992 ± 174.907	-71.230 ± 153.036	10.0*	5.8	9	Southern Peru
gfz2017miye	2017-06-25	15:43:30	-41.816 ± 41.542	42.699 ± 44.686	10.0*	4.7	9	Prince Edward Islands Region
gfz2017mjno	2017-06-25	23:30:13	36.160 ± 125.911	72.321 ± 97.225	10.0*	5.8	12	Afghanistan-Tajikistan Border Region
gfz2017mjok	2017-06-25	23:56:10	-26.941 ± 29.638	26.757 ± 17.116	10.0*	4.1	10	South Africa
gfz2017mtyo	2017-07-01	16:24:45	-0.772 ± 55.117	23.051 ± 35.255	10.0*	4.6	7	Democratic Republic of Congo
gfz2017muth	2017-07-02	02:53:51	-26.926 ± 31.271	26.769 ± 19.893	10.0*	4.9	9	South Africa
gfz2017mvlh	2017-07-02	11:59:50	-23.350 ± 8.431	27.275 ± 11.364	10.0*	2.7	5	South Africa
gfz2017mxfq	2017-07-03	11:18:24	40.611 ± 96.602	20.515 ± 99.683	10.0*	5	15	Greece-Albania Border Region
gfz2017mzku	2017-07-04	16:06:03	-37.293 ± 177.379	-73.198 ± 116.911	10.0*	5.7	11	Near Coast of Central Chile

gfz2017naxo	2017-07-05	11:52:17	-23.378 ± 8.382	27.282 ± 11.362	10.0*	2.7	5	South Africa
gfz2017nhgb	2017-07-08	22:48:33	-7.597 ± 123.628	106.044 ± 132.418	10.0*	5.3	11	Java, Indonesia
gfz2017nhtw	2017-07-09	05:56:50	-56.741 ± 82.452	-28.373 ± 96.121	10.0*	5.7	13	South Sandwich Islands Region
gfz2017njbk	2017-07-09	22:54:09	-26.921 ± 22.685	26.773 ± 14.190	62.115 ± 47.947	5.1	15	South Africa
gfz2017nmrz	2017-07-11	22:39:20	-60.149 ± 103.661	-38.664 ± 150.717	10.0*	4.7	8	Scotia Sea
gfz2017nqop	2017-07-14	01:25:01	-2.499 ± 245.302	103.742 ± 224.427	10.0*	4.9	6	Southern Sumatra, Indonesia
gfz2017nrjs	2017-07-14	12:00:33	-34.976 ± 151.647	-72.297 ± 108.181	10.0*	5.1	12	Near Coast of Central Chile
gfz2017ntvs	2017-07-15	20:30:46	31.006 ± 125.632	23.557 ± 150.253	10.0*	5.2	7	Near Coast of Libya
gfz2017nwwa	2017-07-17	12:05:04	-23.674 ± 8.398	27.313 ± 11.912	10.0*	3.1	4	South Africa
gfz2017nxya	2017-07-18	02:05:20	-18.489 ± 147.541	-73.261 ± 177.972	10.0*	5.8	10	Off Coast of Northern Chile
gfz2017nzqx	2017-07-19	00:54:07	12.223 ± 110.331	58.011 ± 130.436	10.0*	4.9	8	Owen Fracture Zone Region
gfz2017oanm	2017-07-19	12:16:57	-18.385 ± 50.942	62.604 ± 99.699	10.0*	5.5	12	Mauritius/Reunion Region
gfz2017oeoc	2017-07-21	17:09:45	38.206 ± 20.685	27.477 ± 84.633	31.892 ± 10.553	5.2	9	Turkey
gfz2017oexz	2017-07-21	22:09:36	-55.656 ± 29.454	-26.490 ± 15.769	39.794 ± 9.594	5.1	14	South Sandwich Islands Region
gfz2017ofsx	2017-07-22	08:43:56	35.510 ± 112.281	72.307 ± 104.635	10.0*	5.3	12	Pakistan
gfz2017ogkc	2017-07-22	17:25:25	37.864 ± 107.191	26.221 ± 97.641	10.0*	5	13	Dodecanese Islands, Greece
gfz2017ohnb	2017-07-23	07:56:29	-1.809 ± 189.024	115.096 ± 197.200	10.0*	5.6	10	Borneo
gfz2017okgm	2017-07-24	20:08:54	-39.624 ± 29.449	45.119 ± 27.705	49.706 ± 24.289	4.2	7	Southwest Indian Ridge
gfz2017okwr	2017-07-25	04:18:57	-26.415 ± 19.403	27.461 ± 16.203	10.0*	4.9	17	South Africa
gfz2017opox	2017-07-27	17:53:15	13.668 ± 134.459	-51.232 ± 163.388	10.0*	6.1	7	North Atlantic Ocean
gfz2017oprq	2017-07-27	19:25:10	-4.569 ± 153.639	100.725 ± 135.254	10.0*	5	10	Southwest of Sumatra, Indonesia
gfz2017oufp	2017-07-30	07:02:23	0.238 ± 32.637	30.109 ± 37.932	10.0*	5.2	15	Uganda
gfz2017ouwo	2017-07-30	15:37:50	28.698 ± 129.447	53.524 ± 116.410	10.0*	5.1	7	Southern Iran
gfz2017oxdz	2017-07-31	21:29:09	34.855 ± 172.989	22.703 ± 105.742	10.0*	5.1	6	Central Mediterranean Sea
gfz2017oxri	2017-08-01	04:23:11	-54.889 ± 20.325	-4.553 ± 20.329	18.608 ± 8.973	5.1	10	Southern Mid Atlantic Ridge
gfz2017ozah	2017-08-01	22:02:39	-56.706 ± 96.768	-28.556 ± 106.197	10.0*	5.2	9	South Sandwich Islands Region
gfz2017pnwz	2017-08-10	01:25:28	-8.520 ± 60.846	30.435 ± 31.843	59.920 ± 27.455	4.6	10	Lake Tanganyika Region
gfz2017pons	2017-08-10	09:52:00	-25.416 ± 56.132	-12.356 ± 115.652	10.0*	5.1	11	Southern Mid Atlantic Ridge
gfz2017psfm	2017-08-12	10:14:32	-56.218 ± 110.763	-29.814 ± 137.856	10.0*	5	7	South Sandwich Islands Region
gfz2017ptnc	2017-08-13	03:08:11	-4.264 ± 152.408	101.315 ± 128.740	10.0*	6.4	10	Southern Sumatra, Indonesia
gfz2017pvhp	2017-08-14	02:43:52	36.791 ± 129.528	27.243 ± 137.848	10.0*	5.1	9	Dodecanese Islands, Greece
gfz2017qcqe	2017-08-18	02:59:24	-1.326 ± 80.012	-13.573 ± 86.833	10.0*	5.9	12	North of Ascension Island
gfz2017qids	2017-08-21	03:31:53	-56.746 ± 86.098	-27.648 ± 109.359	10.0*	4.9	10	South Sandwich Islands Region

gfz2017qmow	2017-08-23	13:42:45	36.715 ± 81.989	48.801 ± 82.427	10.0*	5.4	17	Northwestern Iran
gfz2017qvav	2017-08-28	04:51:14	-21.308 ± 10.434	32.726 ± 41.851	127.267 ± 20.648	5.4	14	Mozambique
gfz2017qwwr	2017-08-29	05:00:42	-39.793 ± 134.194	96.729 ± 109.396	10.0*	5	10	Southeast Indian Ridge
gfz2017ribv	2017-09-04	08:07:12	-60.648 ± 120.612	-29.242 ± 143.964	10.0*	5.9	8	South Sandwich Islands Region
gfz2017rjdl	2017-09-04	21:55:15	-20.567 ± 129.756	-69.769 ± 109.357	10.0*	5.8	14	Northern Chile
gfz2017rnfy	2017-09-07	03:51:05	8.642 ± 16.809	45.271 ± 21.540	151.238 ± 12.979	4.7	11	Ethiopia
gfz2017rqcp	2017-09-08	17:35:28	14.733 ± 100.187	56.617 ± 95.755	10.0*	5.1	10	Owen Fracture Zone Region
gfz2017ruac	2017-09-10	20:53:12	-9.634 ± 31.588	66.668 ± 17.540	46.401 ± 12.626	4.8	10	Mid Indian Ridge
gfz2017scpb	2017-09-15	13:31:00	-30.116 ± 53.684	26.167 ± 15.484	10.0*	5.3	10	South Africa
gfz2017shlr	2017-09-18	05:29:13	-20.428 ± 43.917	-4.578 ± 106.690	10.0*	5.3	12	South Atlantic Ocean
gfz2017sicl	2017-09-18	13:47:03	-33.511 ± 128.350	-71.115 ± 100.373	10.0*	5.8	15	Near Coast of Central Chile
gfz2017syyr	2017-09-27	19:21:50	-58.366 ± 83.214	-24.857 ± 99.565	10.0*	5.1	11	South Sandwich Islands Region
gfz2017tcfa	2017-09-29	13:49:57	38.522 ± 115.017	69.701 ± 114.793	10.0*	5.7	12	Tajikistan
gfz2017tmsy	2017-10-05	08:11:31	-22.582 ± 238.231	-67.141 ± 133.948	10.0*	5.5	8	Chile-Bolivia Border Region
gfz2017tpyq	2017-10-07	02:40:27	-26.783 ± 72.845	51.787 ± 75.163	10.0*	4.4	6	South Indian Ocean
gfz2017ttrw	2017-10-09	03:46:59	-13.511 ± 69.101	64.702 ± 88.755	10.0*	5.1	13	Mid Indian Ridge
gfz2017twrg	2017-10-10	18:52:51	-58.154 ± 108.391	4.426 ± 100.719	10.0*	6.1	9	Bouvet Island Region
gfz2017tyup	2017-10-11	22:49:39	39.986 ± 105.278	22.069 ± 103.678	10.0*	5	13	Greece
gfz2017ulye	2017-10-19	03:25:40	-50.920 ± 18.533	23.426 ± 47.184	19.941 ± 10.847	5.1	9	South of Africa
gfz2017urpy	2017-10-22	06:05:28	-7.587 ± 23.911	30.529 ± 18.397	10.0*	5.1	15	Lake Tanganyika Region
gfz2017utqi	2017-10-23	08:32:28	-53.044 ± 18.228	16.798 ± 37.433	19.627 ± 10.312	5.7	8	Southwest of Africa
gfz2017vgse	2017-10-30	12:14:52	-7.066 ± 19.476	35.849 ± 20.443	65.967 ± 18.401	4.9	9	Tanzania
gfz2017vjhv	2017-10-31	22:25:57	-60.478 ± 95.911	-24.763 ± 112.301	10.0*	5.3	9	South Sandwich Islands Region
gfz2017wbti	2017-11-11	00:36:08	-11.933 ± 25.590	-15.300 ± 14.547	20.731 ± 7.661	5.5	14	Ascension Island Region
gfz2017xbjv	2017-11-25	01:26:33	-26.616 ± 25.685	27.548 ± 20.387	10.0*	4.2	12	South Africa
gfz2017xhed	2017-11-28	05:22:06	-28.704 ± 43.570	27.043 ± 18.774	10.0*	4.5	8	South Africa
gfz2017yfpe	2017-12-11	14:09:55	34.894 ± 111.509	47.401 ± 145.517	10.0*	5.6	9	Western Iran
gfz2017ygzv	2017-12-12	08:43:19	29.651 ± 90.962	58.649 ± 93.090	10.0*	5.9	14	Southern Iran
gfz2017yhzr	2017-12-12	21:41:43	28.718 ± 113.059	57.086 ± 134.504	10.0*	5.9	9	Southern Iran
gfz2017yjnx	2017-12-13	18:03:53	-53.745 ± 93.216	3.726 ± 77.982	10.0*	5.7	12	Bouvet Island Region
gfz2017ylzs	2017-12-15	02:20:40	-26.873 ± 28.955	26.703 ± 16.148	10.0*	4.1	10	South Africa
gfz2017zemd	2017-12-25	05:04:44	-24.679 ± 9.032	27.167 ± 10.105	10.0*	3.4	8	South Africa
gfz2018amay	2018-01-07	14:07:05	-33.675 ± 17.014	11.662 ± 16.307	32.180 ± 14.934	4.6	11	South Atlantic Ocean
gfz2018asux	2018-01-11	06:59:24	34.309 ± 93.348	47.395 ± 106.728	10.0*	5.6	13	Western Iran

gfz2018asuy	2018-01-11	07:00:58	32.985 ± 134.724	45.956 ± 153.001	10.0*	5.8	8	Iraq
gfz2018asvj	2018-01-11	07:14:05	34.564 ± 90.698	48.527 ± 99.063	10.0*	5.7	14	Western Iran
gfz2018aswx	2018-01-11	08:00:39	33.148 ± 113.431	47.622 ± 114.211	10.0*	5.6	11	Western Iran
gfz2018atru	2018-01-11	18:26:31	15.014 ± 45.879	97.335 ± 24.023	45.257 ± 10.249	6.2	12	Near South Coast of Myanmar
gfz2018aymg	2018-01-14	09:18:58	-18.136 ± 121.367	-71.828 ± 128.243	10.0*	7.3	15	Off Coast of Northern Chile
gfz2018biod	2018-01-19	21:45:20	-29.130 ± 45.874	20.218 ± 22.440	10.0*	4.6	9	South Africa
gfz2018blci	2018-01-21	07:12:19	-26.567 ± 23.118	27.530 ± 16.676	83.378 ± 47.318	5	11	South Africa
gfz2018bosl	2018-01-23	06:34:49	-6.804 ± 182.200	106.216 ± 118.748	10.0*	5.9	9	Java, Indonesia
gfz2018bryp	2018-01-25	01:16:05	7.121 ± 146.070	91.005 ± 108.600	10.0*	5.9	11	Nicobar Islands, India Region
gfz2018byoj	2018-01-28	16:03:24	-51.092 ± 109.795	11.800 ± 67.367	10.0*	6.1	11	Southwest of Africa
gfz2018bzax	2018-01-28	22:23:48	-51.648 ± 112.167	11.061 ± 74.215	10.0*	5.1	10	Southwest of Africa
gfz2018cdje	2018-01-31	07:06:36	35.816 ± 129.364	72.421 ± 108.297	10.0*	6.6	12	Pakistan
gfz2018cnfm	2018-02-05	16:37:36	-7.733 ± 43.439	27.032 ± 19.869	10.0*	5.1	9	Democratic Republic of Congo
gfz2018ctlr	2018-02-09	02:32:43	-17.609 ± 30.415	25.179 ± 11.062	10.280 ± 6.637	4.1	9	Zambia
gfz2018dgza	2018-02-16	12:04:18	-23.990 ± 27.873	30.615 ± 54.452	10.0*	5.3	8	South Africa
gfz2018djya	2018-02-18	02:54:56	-58.396 ± 92.428	-23.481 ± 119.583	10.0*	5.7	9	South Sandwich Islands Region
gfz2018dlzg	2018-02-19	05:51:16	-17.598 ± 27.510	25.089 ± 7.724	11.494 ± 5.226	4.7	9	Zambia